CZECH TECHNICAL UNIVERSITY
IN PRAGUE

Faculty of Nuclear Sciences and Physical
Engineering

Department of Physics

Master's thesis

Connection between Energy Spectrum, Mass Composition and Distribution of Sources of Extragalactic Cosmic Rays

Bc. Alena Bakalová

Supervisor: Ing. Jakub Vícha, Ph.D.

Prague, 2018

ČESKÉ VYSOKÉ UČENÍ TECHNICKÉ
V PRAZE
Fakulta jaderná a fyzikálně inženýrská
Katedra fyziky

Diplomová práce

Souvislost mezi energetickým spektrem, složením a rozložením zdrojů extragalaktického kosmického záření

Bc. Alena Bakalová

Školitel: Ing. Jakub Vícha, Ph.D.

Praha, 2018

Prohlášení:

Prohlašuji, že jsem svou diplomovou práci vypracovala samostatně a použila jsem pouze podklady (literaturu, projekty, SW atd.) uvedené v přiloženém seznamu.

Nemám závažný důvod proti použití tohoto školního díla ve smyslu § 60 Zákona č. 121/2000 Sb., o právu autorském, o právech souvisejících s právem autorským a o změně některých zákonů (autorský zákon).

V Praze dne

Alena Bakalová

Title:

Connection between Energy Spectrum, Mass Composition and Distribution of Sources of Extragalactic Cosmic Rays

Author: Bc. Alena Bakalová

Specialization: Experimental nuclear and particle physics

Supervisor: Ing. Jakub Vícha, Ph.D.

Consultant: RNDr. Petr Trávníček, Ph.D.

Abstract:

This master's thesis is dedicated to the simulated propagation of extragalactic cosmic-rays in the Universe using the simulation program CRPropa 3. In the first part of the research, we focused on the very end of cosmic-ray energy spectrum measured by the Pierre Auger Observatory. Single-source scenarios with potential to explain the shape of this observed energy spectrum were investigated taking into account different parameters of the sources and the resulting mass composition of cosmic rays on Earth. In the second part of the research, we studied arrival directions of extragalactic cosmic rays on Earth that enter the Galaxy from an isotropic flux. Two most-updated models of Galactic magnetic field were considered in the simulations of propagation of these particles. We found indications of quadrupole and dipole patterns in the arrival directions of cosmic rays arisen as a consequences of Galactic magnetic fields.

Key words: Ultra-High Energy Cosmic Rays, Propagation of Cosmic Rays, CRPropa, Energy Spectrum of Cosmic Rays, Large-scale Anisotropy.

Název:

Souvislost mezi energetickým spektrem, složením a rozložením zdrojů extragalaktického kosmického záření

Autor: Bc. Alena Bakalová

Obor: Experimentální jaderná a částicová fyzika

Školitel: Ing. Jakub Vícha, Ph.D.

Konzultant: RNDr. Petr Trávníček, Ph.D.

Abstrakt:

Tato diplomová práce popisuje výsledky simulací šíření extragalaktického kosmického záření vesmírem provedených v programu CRPropa 3. Prvním zkoumaným tématem bylo možné vysvětlení konce energetického spektra naměřeného Observatoří Pierra Augera jediným zdrojem kosmického záření. Zkoumaly se různé vlastnosti těchto zdrojů a rovněž chemické složení částic dopadajících na Zemi. Druhá část výzkumu se zabývala rozdělením příchozích směrů extragalaktického kosmického záření přicházejícího na Zemi z původně isotropního toku těchto částic do Galaxie. K simulaci propagace kosmického záření Galaxií byly použity dva modely galaktického magnetického pole. V některých případech vznikaly dipólové a kvadrupólové struktury ve směrech příletů původně isotropních částic jako důsledek vlivu galaktického magnetického pole.

Klíčová slova: Kosmické záření ultra vysokých energií, šíření kosmického záření, CRPropa, energetické spektrum kosmického záření, velkoškálová anisotropie.

Acknowledgements

I would like to sincerely thank my supervisor, Ing. Jakub Vícha, Ph.D. for his patience, professional mentoring and valuable consultations and comments regarding this master's thesis. I am also very thankful to RNDr. Petr Trávníček, Ph.D. for his comments and for his support of the presented research. Finally, I would like to thank my parents for their support, especially my father for his willingness to consults matters far from his research field.

Contents

Chapter 1

Introduction

It has been more than a hundred years since the discovery of cosmic rays [1] and more than fifty years since the discovery of cosmic rays of ultra-high energies ("UHECR", above 10^{18} eV). Despite such a long time, the origin and means of acceleration of the most energetic cosmic-ray particles still remain unanswered questions.

Cosmic rays at the highest energies are usually considered to be of an extragalactic origin. This hypothesis was recently supported by measurements of arrival directions of cosmic rays above 8 EeV by the Pierre Auger Observatory [2]. The original energy spectra and composition of cosmic-ray particles from their sources can be modified during their propagation in the Universe. Furthermore, since cosmic rays are charged particles, their trajectories are influenced by extragalactic and galactic magnetic fields. For that reason, it is important to study simultaneously the effects of propagation of cosmic rays from their sources to the Earth together with measurements of ultra-high energy cosmic rays on Earth by large-area observatories.

In this diploma thesis, two phenomena are investigated. The first part of the research is dedicated to the shape of the cosmic-ray energy spectrum measured at the highest energies by the Pierre Auger Observatory. Propagation of particles originating from single sources of extragalactic cosmic rays were simulated and the properties of these sources were investigated with the aim to find source characteristics that could lead to an energy spectrum on Earth consistent with the measured data. Results summarizing the optimal combinations of mass composition on injected particles, maximal rigidity of the source, its distance and spectral index of the energy spectrum are presented in this thesis, together with mass composition of cosmic rays that would be observed on Earth.

The second investigated phenomenon was the effect of Galactic magnetic field on the distribution of arrival directions of extragalactic cosmic rays. Two models of Galactic magnetic field were considered in simulations of particle

propagation. The results concerning the formation of large-scale anisotropies on Earth from originally isotropic flux of extragalactic cosmic rays due to the influence of Galactic magnetic field are presented in this thesis.

The master's thesis is divided into eight chapters. In the first chapter, a brief historical review together with basic properties of cosmic rays is described, followed by possible sources of UHECR and acceleration mechanisms. The second chapter focuses on propagation of UHECR in the Universe. Energy losses due to interactions with ambient photon fields are described, followed by a description of models of galactic magnetic fields used in our research. The detector layout of the Pierre Auger Observatory, methods of reconstruction of cosmic-ray showers and selected recent results of the Pierre Auger Observatory are introduced in Chapter 4. In Chapter 5, a characterization of simulation frameworks dedicated to the propagation of cosmic rays in the Universe is given. Chapters 6 and 7 focus on the obtained results concerning energy spectrum and effects of Galactic magnetic field on arrival directions of cosmic rays, respectively. Finally, the last chapter summarizes the presented results.

Chapter 2

Cosmic Rays of Ultra-High Energies

Cosmic rays were discovered by an Austrian physicist Victor Franz Hess [1] who undertook a series of balloon ascents between years 1911 and 1913 measuring the level of air ionization at different altitudes in the atmosphere. During numerous flights he reached the maximum height of $5,350$ m and he concluded from his measurements that the ionization of air increases with altitude above 1 km a.s.l., which implies that the radiation does not come from the Earth as it was previously considered but rather from the space [3]. One of his balloon ascent took place during an almost total solar eclipse. Hess observed that there was not a significant decrease in the measured radiation, hence he concluded that the Sun should not be the main source of this radiation coming to Earth. He received the Nobel Prize in Physics in 1936 for his discovery of cosmic radiation [3]. Another important role in the field of cosmic-ray physics played French physicist Pierre Victor Auger who together with Rossi, Boethe, Schmeiser and Kolhörster discovered the extensive air showers of secondary particles from cosmic rays in the late 1930s and in 1938 Auger announced an existence of a primary cosmic-ray particle with energy 10^{15} eV or higher, a million times higher energy than was attributed to cosmic rays at that time [4]. Even more energetic cosmic-ray particle with at that time unbelievable energy exceeding 10^{20} eV was detected by John Linsley and collaborators in 1962 at the Volcano Ranch Array in New Mexico [5].

Cosmic rays are charged particles coming from outer space, mainly originating outside the Solar System. These particles, called primary particles of cosmic rays, are predominantly protons (86%), alpha particles (11%) and nuclei of heavier elements up to iron [6]. A shower of secondary particles is created when a primary cosmic ray enters the atmosphere and interacts with an atmospheric nucleus. A wide range of particles can be created during the formation

of cosmic-ray shower of secondary particles including pions, kaons, muons, electrons, photons or neutrinos and nuclear fragments.

Even though it is more than 50 years since cosmic-ray particles of ultra-high energies were first discovered, still many important questions remain unanswered. In this chapter, properties of cosmic rays and especially UHECR will be described, concerning their energy spectrum, mass composition and possible sources and mechanisms of their acceleration.

2.1 Energy Spectrum

The energy spectrum of cosmic rays is very wide and extends over more than ten orders of magnitude with the number of incoming particles rapidly decreasing with increasing energy E. A particle with energy $\approx 10^{11}$ eV can be observed on 1 m^2 every second while a particle with energy $\approx 10^{19}$ eV strikes an area of 1 km^2 only once per year. The energy spectrum of primary cosmic rays follows approximately E^{-3} as can be seen in Figure 2.1 where the cosmic-ray flux is scaled by $E^{2.5}$ to better visualise the spectral features. There are few energies where the spectrum noticeably changes its behaviour. A steepening of the spectrum, the so called "knee", occurs around the energy $E \approx 10^{15.6}$ eV. Another significant change in the energy spectrum is its hardening around the energy $E \approx 10^{18.6}$ eV referred to as the "ankle". The last important feature is the cut-off at the highest energies above $E \approx 10^{19.6}$ eV [7]. Additional, less visible, feature is another knee around the energy $E \approx 10^{17.5}$ eV [8, 9] where another weak steepening occurs.

These changes of the spectral index of energy spectrum are reflecting mechanisms standing behind the acceleration and production mechanisms of cosmic-ray particles for given energy, such as the maximal rigidity[1] of the sources or the magnetic confinement inside our Galaxy.

If we suppose that there is a maximal energy $E_{\max}(Z = 1)$, where Z is the proton number, to which protons can be accelerated by a source, different particles should be accelerated to maximal energies depending on their charge $q = Ze$. This mechanism, first described by Peters in [10] and thus called the Peters cycle, causes that protons are cutoff first and are followed by heavier nuclei. The maximal energy can be described as

$$E_{\max}(Z) = ZeR_{\text{Source}} = ZeE_{\max}(Z = 1), \tag{2.1}$$

where R_{Source} is the rigidity of the source. The first knee is usually explained

[1] Rigidity is a quantity defined as $R = \frac{E}{q}$, where E is the particle energy and q is the charge of the particle.

as the energy at which the galactic protons drop out because of the absence of sources in Milky Way capable to accelerate protons to higher energies or they start to escape from the Galaxy and are no longer confined within it. The second knee is observed at energies where heavier nuclei (i.e. up to iron) drop out due to the same reasons [7]. The cut-off at the end of the energy spectrum was predicted by Greisen [11], Zatsepin and Kuzmin [12] who calculated a theoretical upper limit of the energy of cosmic-ray protons originating from distant sources. This maximal energy of cosmic rays of extragalactic origin emerges as a result of photo-pion production on the cosmic microwave background ("CMB") which is described in Section 3.1.1. The energy where the spectrum rapidly falls is usually referred to as the GZK cut-off corresponding to the energy approximately $E = 10^{19.7}$ eV for protons, which is in a nice agreement with the measurements of the Pierre Auger Observatory and HiRes experiment (see Figure 2.1). However, this cut-off might also be caused by the limits of acceleration possibilities of the sources.

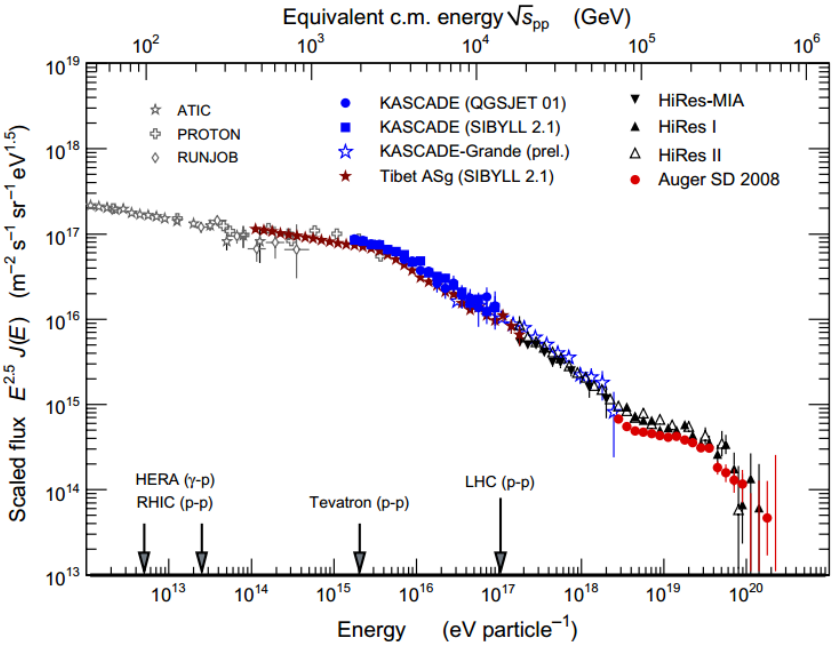

Figure 2.1: The energy spectrum of cosmic rays obtained from various experiments [13]. Note that the flux is scaled by energy $E^{2.5}$.

2.2 Mass Composition of Observed Cosmic Rays

The mass composition of primary cosmic rays evolves with their energy. As it was already mentioned in the previous section, some of the important features of the energy spectrum are related to the rigidity of sources or to the Galactic magnetic confinement resulting in the effect that different nuclei are dominant at different energies. A detailed knowledge of the energy spectrum together with the chemical composition of UHECR is crucial to understand the physics of their origin and their propagation in the universe.

Since we are able to detect only the secondary particles of cosmic-ray showers and not the primary ones at the ultra-high energies, we need to find shower properties that are sensitive to the chemical composition of the primary particle. The depth[2] of shower maximum (X_{max}), corresponding to the depth in the atmosphere where the shower contains the most electromagnetic particles, is one of the most sensitive quantities to the mass composition of primary particles which we can measure with present-day experiments, namely it can be reconstructed from the signal in fluorescence detectors. Unfortunately, these detectors can not be operated all the time, but only when there is a minimal background light implying their low duty cycle ($\sim 10\%$) and consequently low number of detected showers with the information on X_{max}. Predictions of X_{max} values and other shower parameters are derived using simulations of cosmic-ray showers. There are multiple models of hadronic interactions used for the purpose of cosmic-ray shower simulation such as those tuned to the LHC data (run 1): EPOS-LHC [14], QGSJetII-04 [15] or Sibyll 2.3c [16]. The predicted values of X_{max} are subsequently used to determine the mass composition of primary particles that induced real detected air showers.

Measurements of mean X_{max} from multiple experiments are shown in Figure 2.2. Measured data are compared with predictions of models of hadronic interactions for proton and iron nuclei. Clearly, the composition of cosmic rays develops with energy and different primaries are dominant for different energy ranges. Note that the information on X_{max} for energies above $\sim 4 \cdot 10^{19}$ eV is currently missing.

The estimations of mean $\ln A$ of primary particles based on X_{max} predictions of different hadronic interaction models are depicted in Figure 2.3. Same trends

[2]The atmospheric depth X at the altitude h is defined as

$$X = \int_{\infty}^{h} \frac{\rho(l)}{\cos\theta} \mathrm{d}l,$$

where $\rho(l)$ is the density of air at altitude l and θ is the zenith angle of primary particle.

as in Figure 2.2 can be seen in these plots. Measurements indicate an increase of the mean $\ln A$ of primary cosmic rays between 10^{15} eV and 10^{17} eV. At energy around 10^{17} eV the measurements suggest dominance of heavy components in cosmic-ray composition. The mass composition gets lighter with further decrease of energy and it reaches the lightest composition of primaries around the energy 10^{18} eV. This minimum of $\ln A$ is followed by another hardening of the mass composition.

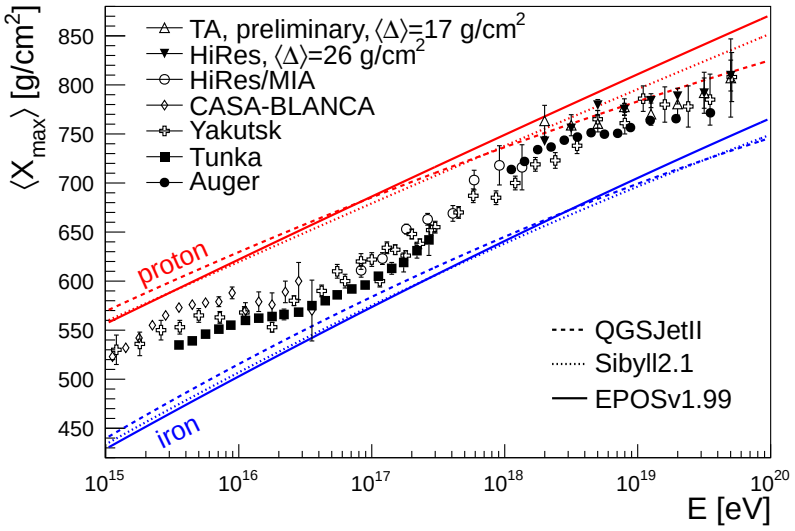

Figure 2.2: Measurements of the mean $X_{\max}$ depending on energy from multiple experiments compared to predictions of air-shower simulations [17].

A small statistics at the highest energies is a severe problem for the interpretation of the measured data. The use of surface detectors operating almost 100% of the time for the mass composition measurement is an ideal way to increase the event statistics. For instance, it has been shown that the maximum production depth of muons (denoted as $X^{\mu}_{\max}$) measured by surface detectors can be also used for mass composition analysis at higher zenith angles up to energies beyond $6 \cdot 10^{19}$ eV [18]. Another technique of shower analysis using only surface detectors came up with a quantity $\sec\theta_{\max}$ which is also sensitive to the mass composition of cosmic rays [19]. $\sec\theta_{\max}$ defines an angle where the so called asymmetry parameter, defined from the rise times $t_{1/2}$ of water Cherenkov detectors, reaches its maximum. Ongoing upgrade of the Pierre Auger Observatory [20] is, among other things, intended to improve the mass composition analysis based on surface detectors for all zenith angles.

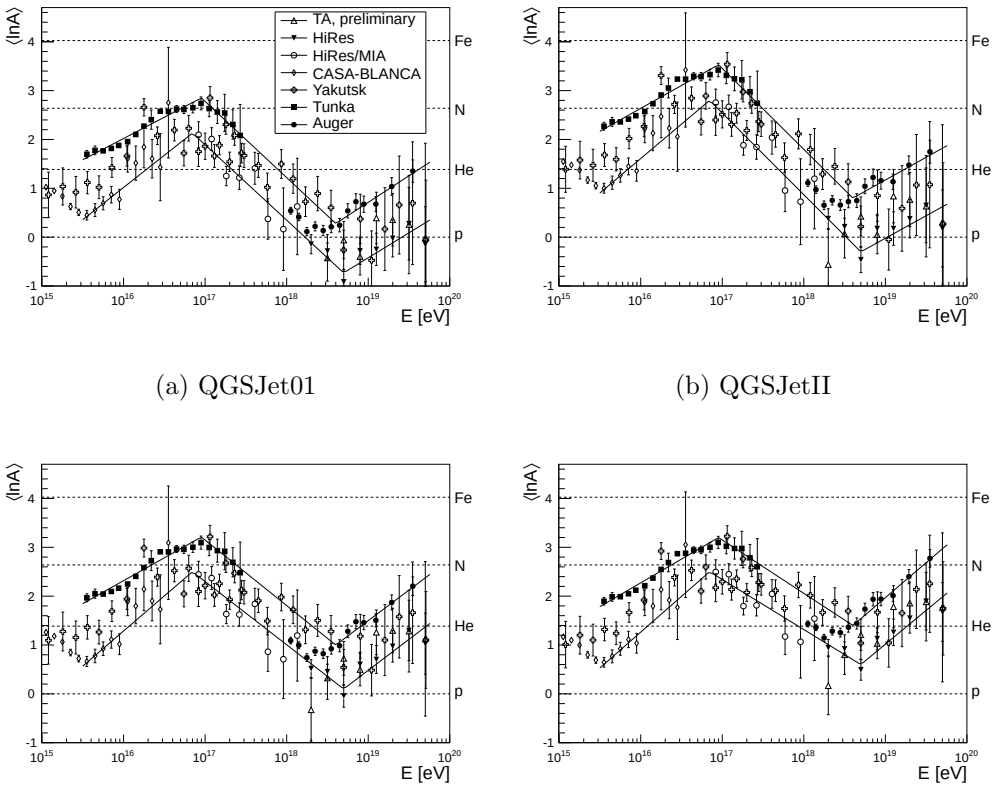

(a) QGSJet01

(b) QGSJetII

(c) Sibyll2.1

(d) Epos1.99

Figure 2.3: Evolution of the mean logarithmic mass of cosmic rays with energy interpreted with different hadronic interaction models. $X_{\max}$ measurements by multiple experiments were used to transform $< X_{\max} >$ to $< ln\mathrm{A} >$ [17].

2.3 Possible Sources of Ultra-High Energy Cosmic Rays

There are two distinct sections in which we can divide the hypotheses about the origin of UHECR. The first one is the "top-down" production process which claims that the cosmic-ray particles of the highest energies might come from the decays of extremely heavy particles including, for example, scenarios of exotic super-heavy particles of dark matter [21]. Second branch of the hypotheses about UHECR origin are referred to as the "bottom-up" scenarios, where cosmic-ray particles are accelerated in the vicinity of astrophysical objects by electromagnetic processes. The "top-down" processes are disfavoured by the measurements of neutrino and photon fluxes at the highest energies [21]. Let us

remind again that recent measurements and studies of observed UHECR by the Pierre Auger Observatory imply that the most energetic cosmic-ray particles (above 8 EeV) have an extragalactic origin [2].

Multiple mechanisms that could be able to accelerate particles to these extreme energies were proposed. The basic concept proposed by Fermi already in 1949 [22] and the later modification of his original theory given by Axford, Leer and Skadron [23] will be described in the following paragraphs.

Fermi's second order acceleration

In 1949, Enrico Fermi proposed a mechanism of acceleration of cosmic rays to ultra-high energies. The concept how particles gain their energy is a stochastic acceleration of the particle in collisions with a magnetised cloud moving with a velocity v and magnetic field B. The average energy gained in one collision is

$$\frac{\Delta E}{E} = \frac{4}{3}\beta^2, \tag{2.2}$$

where β is the velocity relative to the speed of light of the scatter centre. Since this velocity of the magnetised cloud is $\beta << 1$, the particle can be accelerated to ultra-high energies after a large number of collisions. Consequently this process of acceleration to the highest energies is of too low efficiency.

Fermi's first order acceleration

Axford, Leer and Skadron modified Fermi's original theory in order that the acceleration of particles would be more efficient and they proposed a model known as Fermi's first order acceleration mechanism. In this case, the acceleration of a particle takes place at the shock front of a supernova (but is valid also for other objects). In a simplified one-dimensional picture, we can imagine a particle with velocity v_1 in the positive x direction and a shock front moving with a velocity $-u$ in the opposite direction. The particle is back-scattered behind the front through the shock wave with increased velocity v_2. The particle can be reflected back along the upstream of the shock front and the acceleration process repeats itself. The mechanism is depicted in Figure 2.4. The energy gain per shock crossing is proportional to β, therefore, this process of acceleration of particles is much more efficient than the Fermi's second order acceleration. The resulting energy spectrum of particles accelerated in this way turns out to be a power law with the spectral index $\gamma \geq 2$.

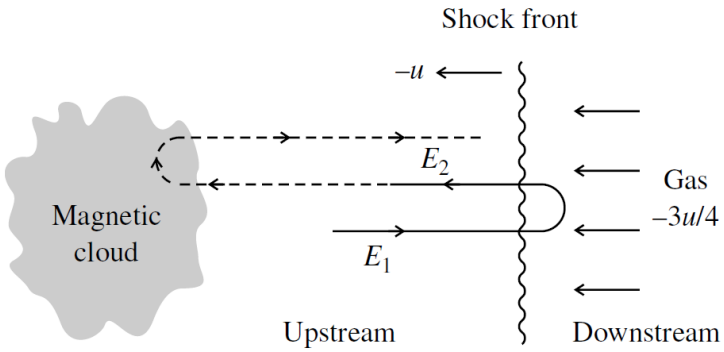

Figure 2.4: Scheme of the Fermi's first order acceleration mechanism [6].

Other mechanisms of acceleration

The theories of sources of UHECR often include the most violent objects in the Universe which are thought to have the appropriate environment for the acceleration of particles up to the highest energies. One of the possibilities are the active galactic nuclei (AGNs), which are galactic centres with very high luminosities, with jets pointing towards our Galaxy. Another objects that could produce these high energetic particles are gamma-ray bursts, radio galaxies or neutron stars. The true origin of UHECR yet still remains unclear.

A theory proposed in [24, 25] presents a possibility of particle acceleration up to the highest energies in young fast-rotating neutron stars with a strong magnetic field. Neutron stars have a metal-rich surface. Irons on the surface can be stripped off the surface as it is bombarded by particles or can be boiled off by stellar heat. These particles gain energy via the relativistic wind where the rotation energy of the neutron star is transformed to the kinetic energy of particles. As they travel through the supernovae remnants the iron nuclei can also undergo a photodisintegration (see Section 3.1.2.) and the resulting mass composition from the source is then mixed.

Most of the theoretical mechanisms of UHECR acceleration predict a power law like energy spectrum of emitted particles which is a result of statistical acceleration cycles. The latter theory of acceleration predicts a power law energy spectrum with spectral index $\gamma \sim 1$. Acceleration in relativistic shocks by Fermi mechanism should give rise to a power-law spectrum with $\gamma = 2.2 - 2.4$ [26] and plasma wakefield acceleration described in [27] suggests the maximal energy of accelerated particles exceeding 10^{21} eV and expects a power law energy spectrum with spectral index $1 < \gamma < 2$.

Chapter 3

Propagation of Ultra-High Energy Cosmic Rays

Large-area observatories are built to understand the basic properties of ultra-high energy cosmic rays in order to finally answer the persisting questions about their origin. However, during the propagation of UHECR from the source to Earth the original energy spectrum and chemical composition produced by the source can be modified. This is a consequence of the interactions with low-energy photons of CMB and extragalactic background light ("EBL"). That means that we need to understand the propagation effects very well to truly understand the physics behind the origin of UHECR. Moreover, directions of charged particles are also influenced by the magnetic field of our Galaxy and also by extragalactic magnetic fields, therefore, the arrival directions of detected particles do not need to point directly to their original sources, which makes the search for their origin even more complicated. In the following sections, the energy losses caused by interactions with ambient photon fields will be explained and a brief description of galactic and extragalactic magnetic fields will be presented.

3.1 Energy Losses During Propagation

The difference between the chemical composition of UHECR on Earth and at their sources depends on many factors. The most important variables are the distance of the source, the energy of primary particles, strength, direction and location of magnetic fields and the mean photon and energy density in the part of the Universe the particle is passing through.

The most important intergalactic medium that is responsible for energy losses of cosmic rays is the cosmic microwave background radiation. This radiation is a remnant from an early stage of the Universe, called the recombination,

when the Universe became transparent to photons, meaning that their mean free path became longer than the horizon distance. CMB follows the black-body radiation spectrum and has the temperature of ~ 2.7 K corresponding to the mean energy of approximately 10^{-3} eV with very low fluctuations of the temperature (of the order $\sim 10^{-5}$). Cosmic rays can also interact with optical light, infra-red background radiation ("IBR") or radio waves. In the following, the most important energy losses of UHECR due to interactions with CMB and EBL will be described.

3.1.1 Photo-pion Production

The photo-pion production is one of the most significant energy losses at the highest energies. In this process, a nucleon interacts with a background photon and, consequently, a pion is created that gains part of the energy of the nucleon. The production of a pion in a collision of nucleon N and background photon γ can be described as

$$N + \gamma \rightarrow N + \pi. \tag{3.1}$$

The threshold energy for this process is given by the equation

$$E^{N,\pi}_{thres} = \frac{m_\pi(m_N + \frac{1}{2}m_\pi)}{2\epsilon} \approx 6.8 \cdot 10^{19} \left(\frac{\epsilon}{10^{-3}\,\mathrm{eV}}\right)^{-1} \mathrm{eV}, \tag{3.2}$$

where m_π and m_N are the masses of the pion and the nucleon, respectively, and ϵ represents the energy of the background photon [28]. This process leads to the aforementioned GZK cut-off of protons. Proton is excited to the Δ^+ resonance by the photon and decays by the strong interaction into a nucleon and a pion in two channels

$$p + \gamma \rightarrow \Delta^+ \rightarrow \begin{cases} n + \pi^+ & \text{with branching ratio } 1/3 \\ p + \pi^0 & \text{with branching ratio } 2/3 \end{cases}. \tag{3.3}$$

Photo-pion production of a nucleus can be approximated by the superposition model, where the nucleus is treated as the superposition of A free nucleons. The threshold energy for photo-pion production for heavier nuclei is then proportional to the atomic number as $E^{A,\pi}_{thres} = E^{N,\pi}_{thres} \cdot A$.

3.1.2 Photodisintegration of Nuclei

The process of photodisintegration of nucleus happens when a photon is absorbed into a nucleus which leads to an excited state of the nucleus and to the consequent splitting of the nucleus into two or more parts. Different processes

are dominant at different photon energies. At low photon energies, the most relevant process is the giant dipole resonance ("GDR"). The GDR is a collective excitation of the nucleus after an absorption of a photon of energy about 10 MeV to 50 MeV[1]. The GDR usually emits one nucleon, but with lower probability also multiple nucleons or alpha particle can be released as well [29]. At energy about 30 MeV, the probability of quasi-deuteron process becomes comparable to the GDR, and at even higher energies, the total cross section is dominated by this process.

The effective energy loss rate of the photodisintegration of nucleus can be described as

$$\left.\frac{1}{E}\frac{\mathrm{d}E}{\mathrm{d}t}\right|_{eff} = \frac{1}{A}\frac{\mathrm{d}A}{\mathrm{d}t} = \sum_i \frac{i}{A} R_{A,i}(E), \tag{3.4}$$

where $R_{A,i}$ is the rate for emission of i nucleons from a nucleus with mass number A [28]. This process changes not only the particle energy, but also its atomic number and creates new lighter particles.

3.1.3 Pair Production

Another important process of energy loss of UHECR is the production of electron-positron pair. The pair is created in the presence of a nucleus X and the process can be described as

$$^A_Z X + \gamma \rightarrow ^A_Z X + e^+ + e^-, \tag{3.5}$$

where A is the nucleon number and Z is the proton number. The threshold energy for pair production is

$$E^{\pm}_{thres} = \frac{m_e(m_X + m_e)}{\epsilon} \approx 4.8 \cdot 10^{17} A \left(\frac{\epsilon}{10^{-3}\,\mathrm{eV}}\right)^{-1} \mathrm{eV}, \tag{3.6}$$

where m_e and m_x are the masses of electron/positron and of the nucleus X, respectively, and ϵ represents the energy of the background photon [28]. In simulations of propagation of cosmic rays, this process is usually described as a continuous energy loss because of its low threshold energy.

3.1.4 Cosmological Redshift

Red-shift of photons from distant sources, where photons undergo an increase of wavelength due to the expansion of the Universe, is a well known phenomena.

[1]These energies are meant in the laboratory frame of the nucleus.

Cosmic-ray particles are also affected by the expansion of the Universe resulting in the energy loss. Red-shift energy losses are dominant at low energies, i.e. below the energy threshold of pair production, where other processes such as photo-pion production do not yet occur. Energy losses by cosmological red-shift can be described as

$$-\frac{1}{E}\left(\frac{\mathrm{d}E}{\mathrm{d}t}\right)_{\text{adiabatic}} = H_0, \tag{3.7}$$

where H_0 is the Hubble constant [28].

We can define the energy loss length χ_{loss} which refers to the travelled trajectory over which the cosmic-ray particle losses on average 1/e of its original energy. Energy loss lengths χ_{loss} for all the aforementioned processes on CMB and EBL are shown in Figure 3.1 for ^{14}N and in Figure 3.2 for ^{56}Fe. Although χ_{loss} for photodisintegration is shown, we need to keep in mind that this process changes the chemical composition of the cosmic-ray particle, so the final χ_{loss} includes also the energy losses due to the photodisintegration of subsequent lighter nuclei, while other processes include only one type of nucleus.

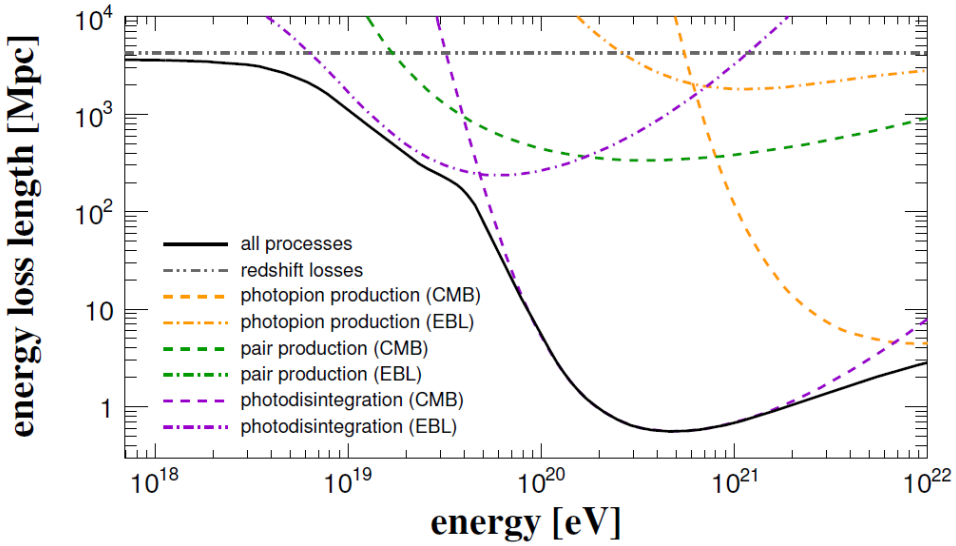

Figure 3.1: Evolution of energy loss length with energy of ^{14}N [30].

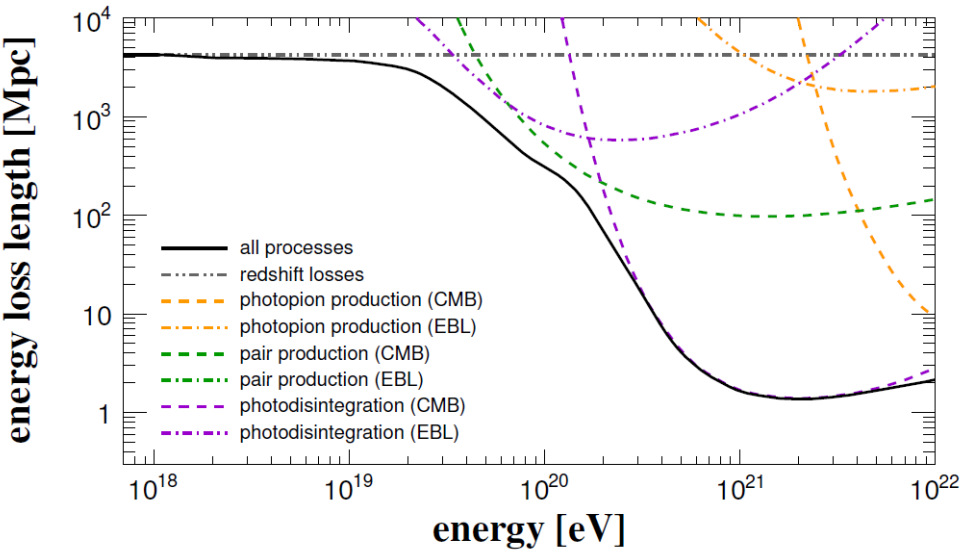

Figure 3.2: Evolution of energy loss length with energy of ^{56}Fe [30].

3.2 Magnetic Fields in the Universe

Since cosmic rays are charged particles they are deflected by the Lorentz force in the presence of magnetic fields. This effect makes the search for their origin even more complicated since the observed arrival direction does not point to the original source. The Larmor radius ${r_L}^2$ for a particle of charge Z and energy E in a magnetic field B can be expressed as

$$\left(\frac{r_L}{\text{pc}}\right) = 1.1 \left(\frac{E}{\text{PeV}}\right) \left(\frac{\mu\text{G}}{B}\right) \frac{1}{Z}. \tag{3.8}$$

Cosmic rays are deflected by both Galactic magnetic field (GMF) and extra-galactic magnetic fields (EGMF). For particles with lower energies ($< 10^{17}$ eV) the Galactic magnetic field is so strong that they become confined within the Galaxy. For higher energies, the Larmor radius becomes larger and particles are no longer confined within the Galaxy [31]. While the strength of GMF can be estimated from multiple measurements, the origin and strength of EGMF is not well understood.

[2]Magnetic field in (3.8) is expressed in units of gaussians, defined as 1 G=10^{-4} T. Distance is expressed in terms of parsecs: 1 pc$\sim$3.26 ly.

3.2.1 Galactic Magnetic Field

Magnetic fields are present in the interstellar and intracluster medium and they extend beyond the Galactic disk. They do not only deflect cosmic rays during their propagation, but they also contribute significantly to the total pressure in the Galaxy, which balances the disk against the gravitation force. Magnetic fields are also affecting the interstellar medium, heating it and influencing its motion, as well as they are essential for the early star formation [32].

The strength of GMF depends strongly on the type of the galaxy. In spiral galaxies, like the Milky Way, the average strength of the total magnetic field is about $10\,\mu$G. Our nearest neighbour, the Andromeda galaxy, has a bit weaker total magnetic field of approximately $5\,\mu$G, while the total magnetic field of spiral galaxies with high star-formation rates is about $(20-30)\,\mu$G. The strongest magnetic fields, having the size $(50-100)\,\mu$G, are observed in starburst galaxies [33].

There are multiple ways how to measure GMF, but the most commonly used are Faraday Rotation Measures, polarized synchrotron radiation, Zeeman splitting and optical polarization of starlight. In the following, Faraday Rotation Measures and polarized synchrotron radiation will be described in more detail since they are the ones used in the two models of GMF used in our research.

When a linearly polarised wave travels through a magnetic field, the plane of the polarization is rotated. This effect, called the Faraday rotation, is a measurable quantity even for astronomical distances. Faraday rotation is caused by the difference in phase velocities of the right-circularly and left-circularly polarized waves whose superposition is the observed total light. The change in the polarization angle ϕ is linearly proportional to the square of the wavelength λ as

$$\phi = \phi_0 + (\mathrm{RM})\lambda^2, \tag{3.9}$$

where ϕ_0 is the initial polarization angle from the source and RM is the rotation measure that is proportional to the magnetic field strength $B_{||}$ and to the number density of electrons n_e defined as

$$RM = \frac{e^3}{2\pi m_{\mathrm{e}}^2 c^4} \int_0^{l_{\mathrm{s}}} n_{\mathrm{e}}(l) B_{||}(l) \mathrm{d}l, \tag{3.10}$$

where l goes from the observer ($l = 0$) to the source ($l = l_{\mathrm{s}}$) and m_{e} is the mass of an electron [32]. The measurement is usually performed on either galactic pulsars or extragalactic radio sources and it needs to be evaluated for more than one wavelength to get an accurate value of RM.

Another tool to study the magnetic field strength in the Universe is the polarized synchrotron radiation. Synchrotron radiation is emitted by relativistic

electrons in a magnetic field. The emitted photons are concentrated in a cone pointing in the direction of the motion of the particle and they are also polarised in the direction of the plane perpendicular to the magnetic field. The spectrum of synchrotron radiation therefore holds the information about the magnetic field strength of astronomical sources. The total flux of synchrotron radiation from a source is connected to the strength of magnetic field and polarization of the light can then be used to estimate the field's structure.

Even with information from many measurements, the description of the true nature of our GMF is a very complex problem. It seems that the GMF in Milky Way supposedly composes of a large-scale regular field component and a small-scale irregular component, both having a strength in orders of μG [33]. There exist multiple models of our GMF and they differ not only in the strengths of individual components of the field, but also in the very components included. Some of the models suppose that the Galactic halo has a negligible magnetic effects compared to the rest of the Galaxy and some models include halo as one of the important parts generating the total magnetic field observed. In this thesis, two models of GMF are used, first one is the Jansson Farrar 2012 model (JF12) [34], which is currently the most commonly used one, and for comparison of certain effects a Pshirkov 2011 model of GMF [35] was also used.

Jansson Farrar GMF model

This model of GMF is based on the Faraday rotation measures and the observations of polarised synchrotron light. It composes of a large-scale regular component, a striated random component defined over large features of the regular field and turbulent small-scale random fields arising from objects like supernovae.

The large-scale regular field includes three separate components. It is modeled in a sphere so that for radius $r > 20$ kpc and $r < 1$ kpc[3] the magnetic field vanishes. The disc component of the field was adopted from [36]. It is defined on a $x - y$ plane from 3 kpc to 20 kpc. In the range from 3 kpc to 5 kpc only an azimuthal field is defined, while from 5 kpc to 20 kpc there are 8 logarithmic spiral regions of the magnetic field corresponding to the galaxy type of Milky Way. The disc component is defined symmetrically to the height $\pm h_{\text{disc}}$ on the z axis where the field changes to a toroidal halo component. A scheme of the JF12 GMF model at different z positions is visualised in Figure 3.3. The halo component contains only an azimuthal magnetic field and has a separate field amplitudes in the north and south hemispheres. Last part of the large-scale regular field is the out-of-plane halo component that contains other than azimuthal

[3]The magnetic properties of a close vicinity of the Galactic centre are not well understood and therefore are not included in the model.

components of the halo field. The striated field composes of random fields whose strength and orientation varies on a small scale, but they are arranged to an axis over large-scale features of the regular large-scale component. It is defined with random orientation and strength on small scales, but its relative magnitude is the same across the entire Galaxy. The turbulent component of the total GMF composes of randomly oriented fields with the coherence length of the order 100 pc or less [34].

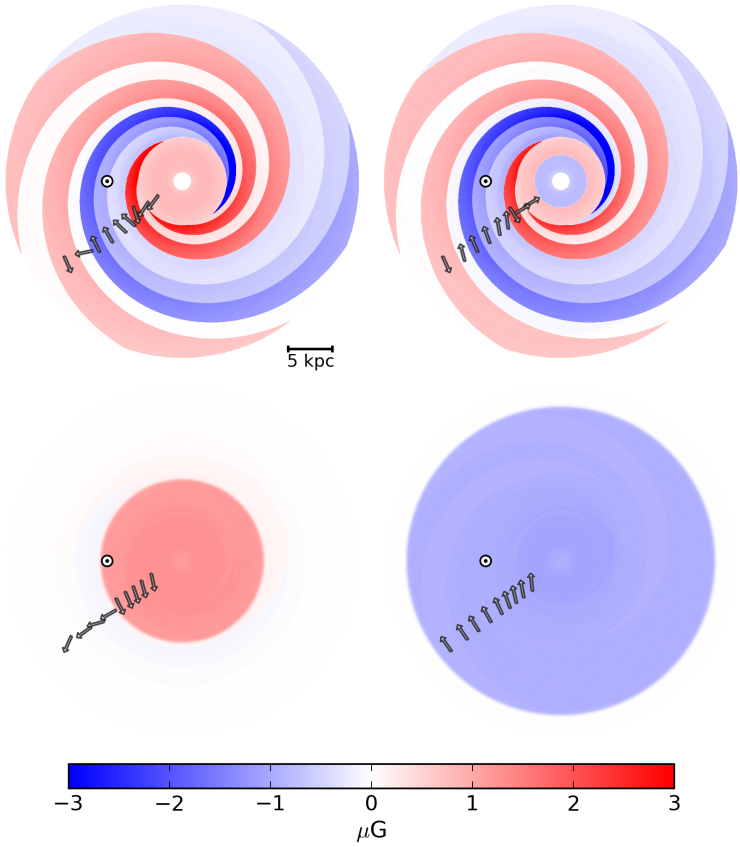

Figure 3.3: Structure of the JF12 model of the GMF. Top left and right pictures show the slices of the field at $z = 10$ pc and $z = -10$ pc, respectively. Bottom left and right pictures demonstrate the field at $z = 1$ kpc and $z = -1$ kpc, respectively. Coloured scale represents the strength of the total regular field. Negative value corresponds to the clockwise orientation of the azimuthal component of the magnetic field [34].

Pshirkov GMF model

Proposed model of GMF by Pshirkov is based on the Faraday rotation measures. GMF is modeled consisting of two components - a disk field and a halo field, where both parts are parametrized independently. While the disk field is symmetric with respect to the Galactic plane, the halo field is thought to be antisymmetric. The basic thought of the two components are very similar to the aforementioned JF12 model, but the fit was performed only based on the Faraday rotation measures. The disk field again corresponds to the spiral type of the Galaxy defined symmetrically to the height $\pm h_{\text{disc}}$ on the z axis where the field changes to the halo component based on the model [37]. The structure of the GMF is shown in Figure 3.4.

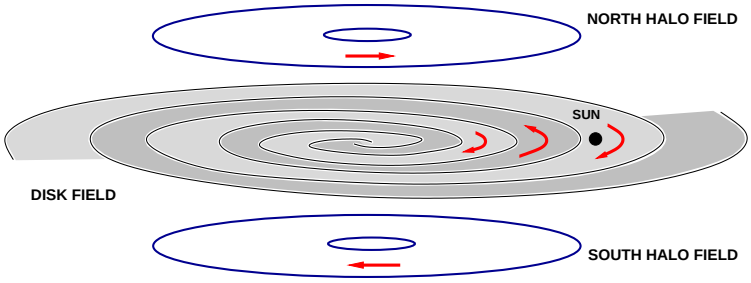

Figure 3.4: Structure of the Pshirkov model of the Galactic magnetic field [35].

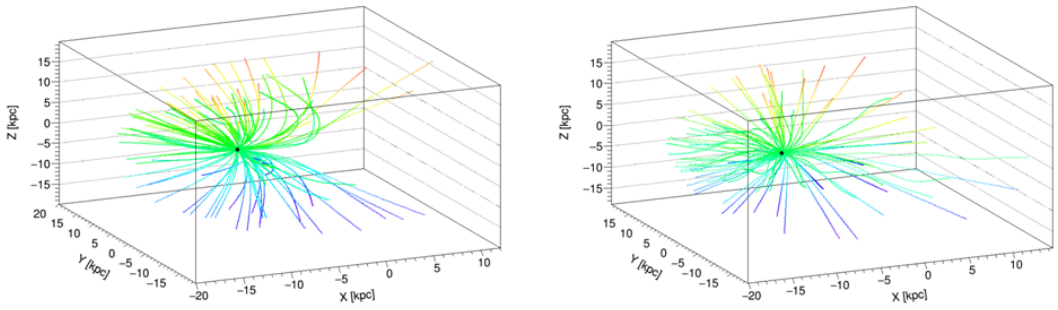

Figure 3.5: Visualisation of trajectories of 100 antiprotons with energy 10^{19} eV originating on Earth for two GMF models performed in the CRPropa simulation framework. JF12 model of GMF (left) and Pshirkov GMF model (right).

Trajectories of 100 antiprotons coming from the Earth in coordinates $(-8.5, 0, 0)$ kpc with energy $E = 10^{19}$ eV simulated in CRPropa code [38] in JF12 (left) and Pshirkov model of GMF (right) are visualised in Figure 3.5. We

can notice a different behaviour of those fields, especially the distinct shadowing of the Galactic centre in the JF12 GMF.

3.2.2 Extragalactic Magnetic Fields

Magnetic fields are also present outside our Galaxy in other galaxies or in the intracluster mediums. Measurement of EGMF is based on the same principles as exploring the fields in our own Galaxy, however, this task is much more difficult to accomplish since the space we are exploring is much larger and much more distant and only in few galaxy clusters the measurement of polarized synchrotron light or Faraday rotation measures had been performed. The strength of magnetic field within galaxy clusters is thought to be between $0.1\,\mu$G and $1\,\mu$G [39].

Theories of the origin of EGMF were made supporting the idea that the EGMF was created from smaller seeds in the early Universe during phase transitions, or from the first starburst galaxies and AGNs. On the other hand, there exist theories which assume that the material from AGNs magnetized only the intracluster medium at low red-shifts, accordingly, the EGMF is present in the proximity of galaxy clusters [40]. Mentioned theories explaining the origin of EGMF are mutually exclusive, therefore, more accurate measurements of EGMF in between the galaxy clusters needs to be made in order to verify of falsify the validity of these theories.

So far, there is no evidence that there exist magnetic fields that are not connected with known structures in the Universe. Such phenomenon is called cosmological magnetic field and there are only upper limits of its strength based on observations of CMB. If a homogeneous cosmological magnetic field was present in the Universe, the expansion of spacetime would not be the same in the direction of the magnetic field and in the direction perpendicular to it. In the perpendicular direction to the cosmological magnetic field, the expansion would act together with the magnetic pressure resulting in a faster expansion and a reduced cosmological red-shift of objects in this direction would be observed. The upper limit of cosmological magnetic field based on angular anisotropy of the CMB was enumerated to be $\leq 3 \cdot 10^{-8}$ G [32].

Chapter 4

The Pierre Auger Observatory

The Pierre Auger Observatory ("PAO") [41] is an experiment dedicated to the study of cosmic rays of ultra-high energies, that is above 10^{18} eV. The experiment is situated in the Province of Mendoza, Argentina, covering the southern hemisphere of the sky with the mean altitude of detectors of ∼1400 m.a.s.l. The construction of the Observatory began in 2002 and was completed in 2008[1] and so far it is the largest cosmic-ray detector ever built. The aim of the Observatory is to reconstruct cosmic-ray showers of secondary particles and determine the energy, mass composition and directions of the primary particles inducing the showers with unprecedented statistics and precision of measurements.

4.1 Observatory Design

The Pierre Auger Observatory is a hybrid detector with the capability of observing cosmic-ray showers simultaneously by two different techniques - an array of surface detectors ("SD") surrounded by fluorescence detectors ("FD"). While the SD has almost 100% duty cycle and records the particle densities as the shower hits the ground, the FD measures the longitudinal development of the shower using fluorescence light emitted by excited and ionised nitrogen molecules[2]. FD operates only during dark moonless nights and therefore has a duty cycle ∼ 10%. This hybrid concept is useful for energy calibration of the SD signal by the precise measurement of energy by FD. Besides, it also allows very high accuracy of the determination of the primary particle direction including the time information of at least one SD station in the FD reconstruction.

[1] The construction of the Observatory was completed in 2008 but the Observatory has been collecting data since 2004 [41].

[2] Detection of the fluorescence light was previously used to detect the cosmic-ray showers for example by the by the Fly's Eye experiment [42].

There are more than 1660 surface detectors placed in a regular triangular grid with spacing of 1500 m and the total area of 3000 km^2. There is also a smaller array of SD stations separated by the distance of only 750 m, which allows detection of particles with lower energies, down to $\sim 10^{17}$ eV. The main grid is shown in the Figure 4.1, where each dot represents one SD station. Four air fluorescence detector sites are placed on the border of the array (labelled in yellow in the Figure 4.1) each consisting of six telescopes.

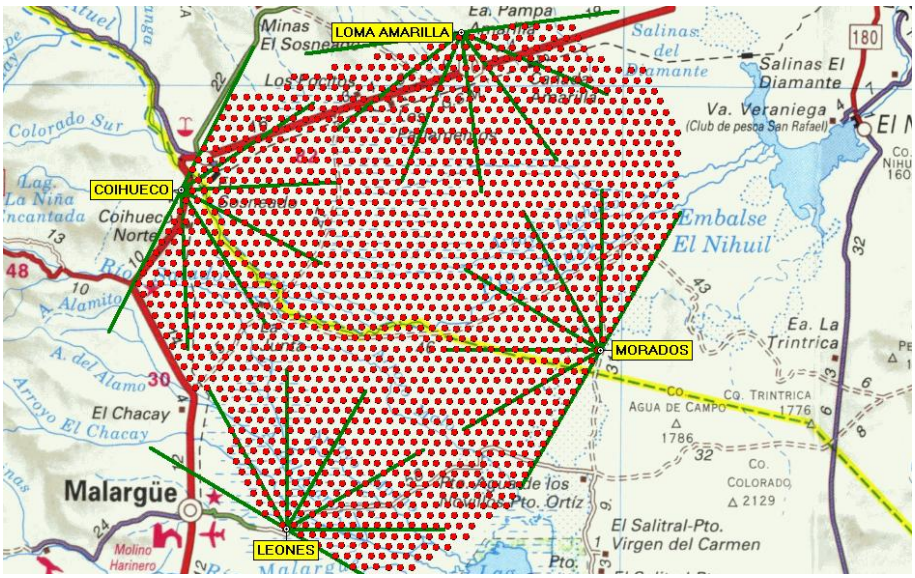

Figure 4.1: Detector layout of the Pierre Auger Observatory. Each red dot represents one SD station. Also the four FD sites, labelled in yellow, are shown with indicated field of view of the individual telescopes [41].

4.1.1 Surface Detectors

The SD stations are self-powered water-Cherenkov cylindrical tanks each containing 12,000 liters of pure de-ionised water [41] (1.2 m height and diameter of 3.6 m) inside of a sealed liner of reflective inner surface. Water-Cherenkov detectors were chosen because of their relatively low cost and also because of their properties suitable for this type of experiment, such as uniform exposure up to $\sim 60°$ of zenith angle or sensitivity to not only charged particles but also to high-energetic photons. Each station has a GPS receiver that is crucial for event timing and synchronization of communications among the individual stations. The power for the detector electronics is provided by the solar photovoltaic system.

When a charged particle with velocity higher than the speed of light in water crosses the detector, the Cherenkov light is created along the particle trajectory and subsequently collected by three 9-inch photomultiplier tubes that are symmetrically placed on top of the liner and look downwards through windows of clear polyethylene into the water. The Cherenkov light detected in the SD is measured in units of VEM (vertical equivalent muon) that corresponds to a signal induced by a single muon of energy 250 MeV trespassing the detector in vertical direction. Energy reconstruction from the SD signals is based on the signal size of a given distance from the shower axis. Another important observable derived from SD is the direction of the primary particle which is reconstructed from arrival times of the signals at individual triggered stations. The reconstruction of the direction of the shower axis is better than 1° at energy 10^{19} eV. Techniques that would allow reconstruction of mass composition of primary cosmic rays based only on SD information are also being developed [19, 43].

4.1.2 Fluorescence Detectors

Charged particles created during the development of cosmic-ray shower in the atmosphere excite and ionise the nitrogen atoms that afterwards emit the fluorescence light in the wavelength range of $\sim (300-430)$ nm [44]. The fluorescence light is emitted isotropically in the ultraviolet part of the spectrum and is induced mainly by the electromagnetic component of the shower.

There are four sites of air-fluorescence detectors (Los Leones, Los Morados, Loma Amarilla, and Coihueco) at the border of the SD array each consisting of six telescopes. These telescopes are oriented towards the array all with the field view of $30^\circ \times 30^\circ$ covering in total 180° in azimuth. Each telescope has an entrance window, a circular aperture, a corrector ring, a segmented mirror of total area 13 m^2 and a camera with photomultipliers. The fluorescence light travels through the UV-passing window and is focused by the mirror into a camera composed of a matrix of 440 pixels located on the focal surface of the telescope [44].

The FD measures the so called longitudinal profile $\frac{\mathrm{d}E}{\mathrm{d}X}$, where X is the slant depth and E is the deposited energy. Therefore, the $X_{\max}$ quantity, that is a key observable for the mass composition studies, can be directly measured [41]. Since the produced fluorescence light is proportional to the collisional energy deposit in the atmosphere, this technique is a near-calorimetric method for the determination of primary energy. Integral of the longitudinal development profile corresponds to approximately 90% of the primary particle's energy [44]. On the contrary, surface detectors sample only a small fraction of the air-shower energy resulting in less precise reconstruction of total energy in the case of the

SD reconstruction.

4.2 Shower Reconstructions

Recorded signals from surface detectors and fluorescence detectors are inputs to the reconstruction of the air-shower geometry (SD, FD), shower size (SD, FD) and longitudinal profile (FD). Different reconstruction methods are used depending on whether both FD and SD recorded the signal (hybrid reconstruction) or the shower signal was collected only by SD stations. The mono-FD reconstruction and stereoreconstruction are not discussed in this thesis, see e.g. [45, 46].

4.2.1 Hybrid Reconstruction

In the hybrid reconstruction, both FD and SD data are used to obtain a final image of the recorded shower. First step for the reconstruction is the processing of triggered FD signals. The background noise is estimated from the variance of the ADC signals at early time bins, where there are no shower signals. Then all triggered FD pixels are searched for shower signals. Only pulses with signal to noise ratios ≥ 5 are taken into account in the reconstruction.

The shower detector plane ("SDP") that is defined as the plane containing shower axis and triggered fluorescence telescopes is obtained from the FD data by minimalization of the function

$$S = \frac{1}{\sum_i q_i} \sum_i q_i \left(\frac{\frac{\pi}{2} - \arccos(\vec{p}_i \cdot \vec{n}_\perp^{\,\mathrm{SDP}})}{\sigma_{\mathrm{SDP}}} \right)^2 \tag{4.1}$$

over all pulses i, where q_i is the integrated signal in pixels, $\vec{n}_\perp^{\,\mathrm{SDP}}$ is a vector normal to the SDP in spherical coordinates, $\vec{p}_i$ is the pointing direction of the pixel and σ_{SDP} is the pointing uncertainty for the SDP fit, which was evaluated as 0.35° [41].

Time information (t) of each triggered FD pixel is used to fit three important parameters T_0, R_p and χ_0, depicted in Figure 4.2 describing the angular movement of the shower within the SDP seen by the triggered telescope

$$t(\chi_i) = T_0 + \frac{R_\mathrm{p}}{c} \tan\left(\frac{\chi_0 - \chi_i}{2} \right). \tag{4.2}$$

The speed of light is denoted as c and χ_i is the angle of ith pixel along the SDP with respect to the horizontal axis at the telescope. T_0 stands for the time of the closest approach of the shower to the fluorescence detector, R_p corresponds

to the perpendicular distance between the telescope and the shower axis and χ_0 is the angular orientation of the shower axis.

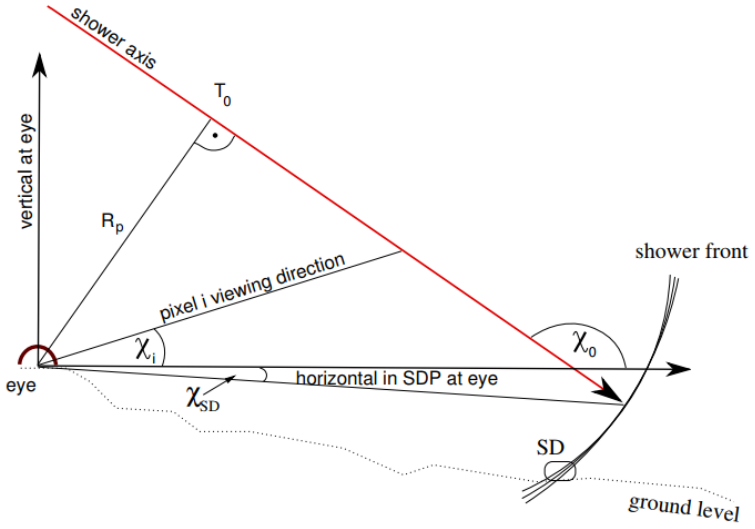

Figure 4.2: Hybrid reconstruction of an air shower [41].

Light collected by the FD as a function of time is then converted to the energy deposited by the shower as a function of the slant depth X. This longitudinal profile of energy deposit is obtained from the fit by the so called Gaisser-Hillas function [47]

$$f_{GH}(X) = \left(\frac{\mathrm{d}E}{\mathrm{d}X}\right)_{\max} \left(\frac{X - X_0}{X_{\max} - X_0}\right)^{(X_{\max}-X_0)/\lambda} \cdot e^{(X_{\max}-X)/\lambda}, \tag{4.3}$$

where $\left(\frac{\mathrm{d}E}{\mathrm{d}X}\right)_{\max}$ is the maximum of the energy deposit at depth $X = X_{\max}$ and X_0 and λ are parameters without a clear physical meaning. The $X_{\max}$ quantity is then derived as one of the fitted parameters.

4.2.2 SD Reconstruction

A typical air shower initiated by a cosmic-ray particle of energy above 10^{19} eV extends over more than 25 km^2 on the ground inducing signals in multiple surface detector stations. Timing and sizes of signals in individual stations are vital parameters for the reconstruction of the shower energy and arrival direction of the primary particle.

The shower geometry is obtained by fitting the start time of the signal in each individual station t_i to the shower plane front. The shower-front development is approximated with a speed-of-light inflating sphere with its centre denoted as virtual shower origin.

The lateral distribution function ("LDF") of the SD signals is described by a modified Nishimura-Kamata-Greisen function [48, 49]

$$S(r) = S(r_{\text{opt}})(\frac{r}{r_{\text{opt}}})^{\beta}(\frac{r+r_1}{r_{\text{opt}}+r_1})^{\beta+\gamma}, \tag{4.4}$$

where S is the predicted signal at distance r from the shower axis, r_{opt} is the optimum distance selected as 1000 m, r_1 was chosen to be 700 m and β and γ are the fitted parameters. An example of dependence of the signal size on the distance from the shower core is shown in Figure 4.3. Axis of the shower $\hat{a}$ is obtained from the shower impact point on the ground $\vec{x_{\text{gr}}}$ and from the virtual shower origin $\vec{x_{\text{sh}}}$ of the geometrical reconstruction as

$$\hat{a} = \frac{\vec{x_{sh}} - \vec{x_{gr}}}{|\vec{x_{sh}} - \vec{x_{gr}}|}. \tag{4.5}$$

The angular resolution for events with more than three active stations is better than 1.6° and for events with more than six active stations it is better than 0.9° for events with an energy above $3 \cdot 10^{18}$ eV [41].

The value of $S(1000)$ decreases with zenith angle θ for a given energy. The shape of the attenuation curve $f_{CIC}(\theta)$ was extracted from the data by the Constant Intensity Cut method [50]. The median angle $\bar{\theta} = 38°$ is used to define $S_{38} = S(1000)/f_{CIC}(\theta)$ that corresponds to the signal produced by a shower of the same energy arriving from $\theta = 38°$. S_{38} is than directly related to the shower energy for all zenith angles.

4.3 Selected Results of the Pierre Auger Observatory

The Pierre Auger Observatory has been collecting data for more than 14 years so far. Since then, many events of UHECR were detected and their analysis led to some interesting results. In this section, results by the PAO concerning the very end of cosmic-ray energy spectrum will be shown and compared with measurements by the Telescope Array ("TA") [51], an experiment located on the northern hemisphere. Also results concerning mass composition of cosmic rays measured by the PAO will be described. Finally, a recent discovery of a dipole in arrival directions of cosmic rays with energies above 8 EeV will be presented.

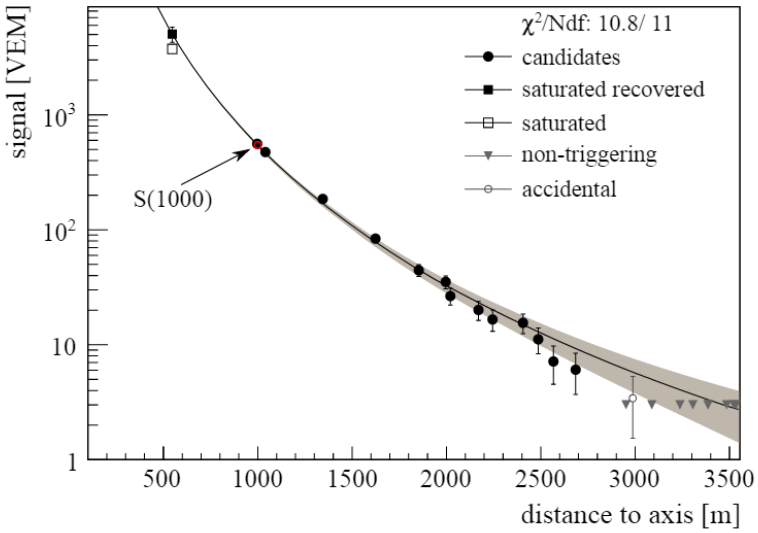

Figure 4.3: Dependence of the signal size on the distance from the shower core for a typical event of energy 10^{20} eV and zenith angle $\sim 25°$ detected in SD of 2the Pierre Auger Observatory [41].

4.3.1 Energy Spectrum

A combination of both FD and SD measurements is used to reconstruct the energy of primary cosmic rays as it was described in previous section. The combined energy spectrum measured by the PAO scaled by E^3 is shown in Figure 4.4. The spectrum can be well described by a broken power law corrected by a smooth suppression at the highest energies. The spectral index of the power law changes rapidly at the ankle energy around 5 EeV from $\gamma_1 \approx 3.3$ to $\gamma_2 \approx 2.5$ [52]. At the very end of the energy spectrum a steep fall ($\gamma_3 \sim 4.8$) is visible that corresponds to the predictions of GZK cutoff, but it can also be a result of maximal energy to which the sources of UHECR are capable to accelerate the particles.

The Telescope Array is an observatory of cosmic rays located in Utah, USA. Measurements of cosmic ray energy-spectrum observed by the PAO and the TA vary at the highest energies. An energy $E_{1/2}$ is defined as the energy where the integral spectrum drops by a factor of two below what would be expected, if there was no cutoff. The value of this quantity for the PAO energy spectrum is $E_{1/2}^{\mathrm{PAO}} = 23 \pm 1 \pm 4$ EeV [52] and for the TA $E_{1/2}^{\mathrm{TA}} = 60 \pm 7$ EeV [53]. The two measured energy spectra are depicted in Figure 4.5. The difference between the two spectra is very distinctive at the very end where the cutoff is expected. Since the PAO is located on the southern hemisphere and the TA on the northern hemisphere, the

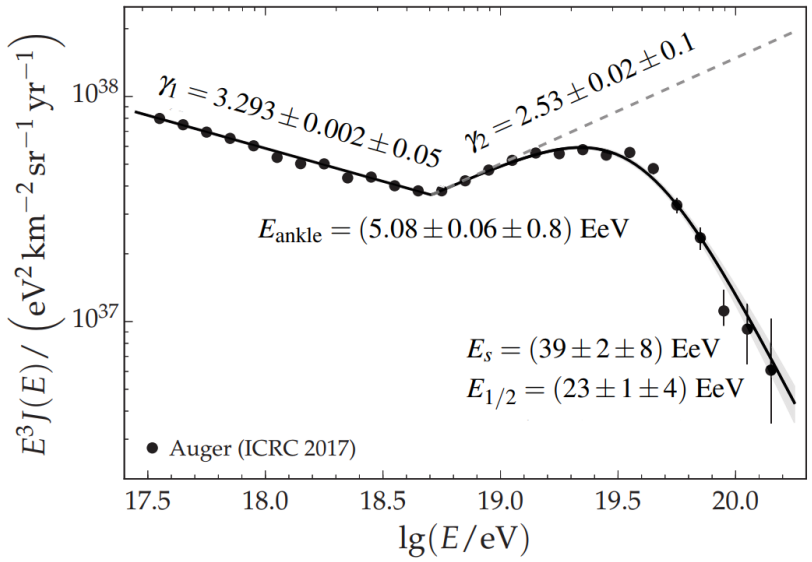

Figure 4.4: Energy spectrum of cosmic rays measured by the PAO. The spectrum is scaled by E^3 [52].

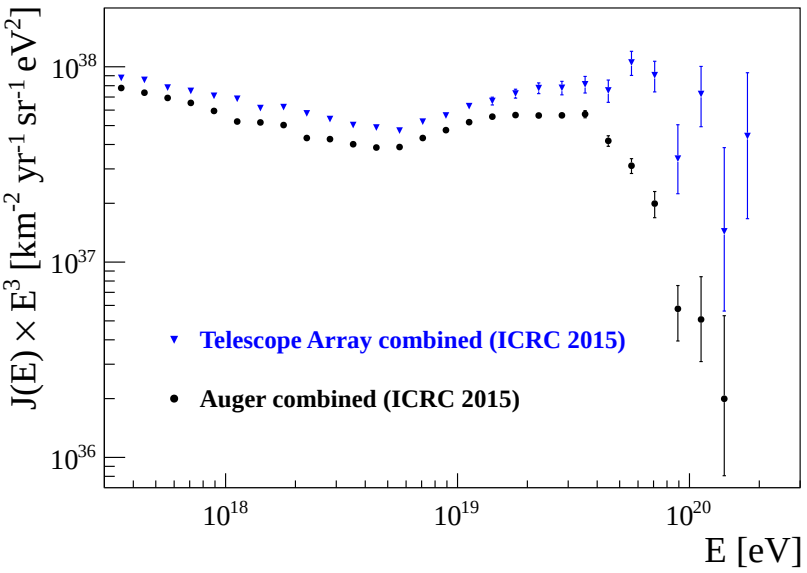

Figure 4.5: Combined energy spectrum of cosmic rays measured by the PAO and the TA. The spectra are scaled by E^3 [53].

diversity between the two measured energy spectra could indicate an anisotropy

of arrival directions of cosmic rays at the highest energies. However, the two experiments differ in measured shower components, shower reconstruction and energy scale, which are also influencing the reconstructed energy spectrum.

4.3.2 Mass Composition

Mean values of $X_{\max}$ measured by the fluorescence detectors of the Pierre Auger Observatory are illustrated in Figure 4.6. The plot shows also predictions for the energy dependence of $X_{\max}$ for protons and iron nuclei for different models of hadronic interactions. The data indicates that in the range of energy from 10^{17} eV to 10^{20} eV the composition is the lightest around the energy $2 \cdot 10^{18}$ eV. For higher energies, as well as for lower energies, the composition becomes heavier and we can probably exclude that the particles arriving to Earth at these energies would be predominantly protons. As the mass composition tends towards heavier primary particles with increasing energy above $2 \cdot 10^{18}$ eV, it seems that for the highest energies the mean atomic number of particles observed on Earth should lay somewhere between helium and nitrogen. Nevertheless, even if these measurements were completely correct, we still can not say much about the composition at the sources of particle's origin except that it is definitely equal or heavier that the one observed on Earth. The original composition at the source and its similarity to the observed one depends on multiple features, mainly on the injection energy at the source and the source distance.

The energy dependence of the mean $\ln A$, where A is the nucleon number of a cosmic-ray particle, derived from $X_{\max}$ and $X^{\mu}_{\max}$ measurements are shown in Figure 4.7 for QGSJetII-04 (left) and for EPOS-LHC (right). Obviously, EPOS-LHC suggests non-physical conclusions based on $X^{\mu}_{\max}$ predictions, since components of cosmic-ray particles heavier than iron nuclei are astrophysically improbable. In this figure, it can be seen that the average mass number is increasing with energy above $2 \cdot 10^{18}$ eV, where the mass composition seems to be the lightest in the studied region, as it already appeared in Figure 4.6.

4.3.3 Large Scale Anisotropy in Arrival Directions of UHECR

The origin of the most energetic cosmic rays still remains a mystery. The anisotropy studies, which are looking for nonuniformities in the distribution of arrival directions of UHECR, are a strong tool which could lead us to the origins of these particles one day.

An evident large-scale anisotropy of arrival directions of cosmic rays with energies above 8 EeV was recently discovered in the PAO data [2]. A harmonic

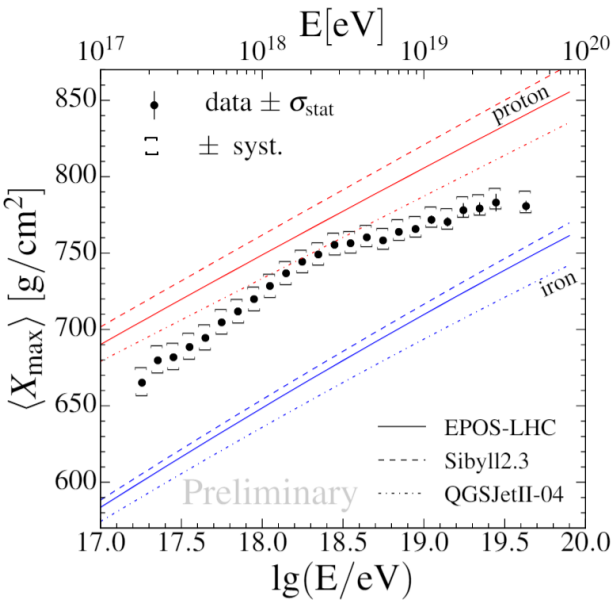

Figure 4.6: Energy dependence of the mean $X_{\max}$ measured by the fluorescence detectors of the Pierre Auger Observatory [54].

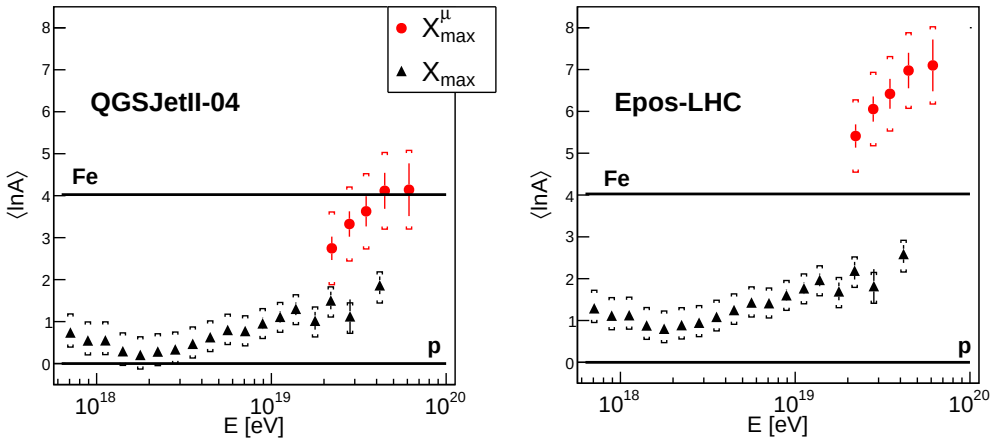

Figure 4.7: Energy dependence of the mean ln A interpreted from $X_{\max}$ (black) and $X^{\mu}_{\max}$ (red) measurements at the Pierre Auger Observatory based on predictions by EPOS-LHC (right) and QGSJetII-04 (left) [18].

analysis in right ascension was performed on events recorded between 2004-2016 with energies 4 EeV $< E <$ 8 EeV and $E >$ 8 EeV. For the lower energies, the data are consistent with isotropic distribution of arrival directions, while an anisotropy was found in the set of particles with $E >$ 8 EeV. The normalized

rates of total 32 187 events with $E > 8$ EeV depending on right ascension are depicted in Figure 4.8 together with the first harmonic with an amplitude $4.7^{+0.8}_{-0.7}\%$ obtained from the Rayleigh analysis [2]. The distribution of recorded events smoothed by a 45° top-hat function is shown in Figure 4.9 in galactic coordinates.

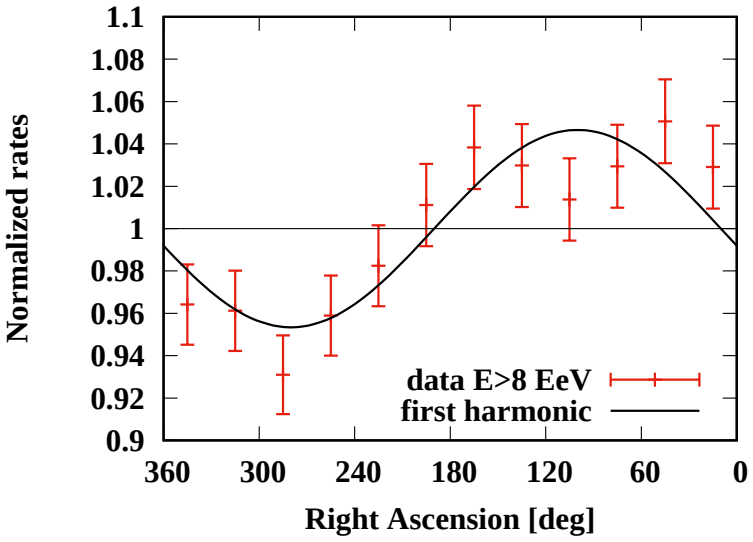

Figure 4.8: Distribution of normalized rates of events with $E > 8$ EeV in right ascension as measured by the PAO together with the first harmonic obtained from the Rayleigh analysis [2].

Since the direction of the dipole is far from the Galactic centre (by $\sim 125°$), this analysis suggests that these particles are of an extragalactic origin. The authors in the article also argue that this anisotropy should come from an anisotropic distribution of extragalactic sources and that "Because of Liouville's theorem, the distribution of cosmic rays must be anisotropic outside of the Galaxy for an anisotropy to be observed at Earth. An anisotropy cannot arise through deflections of an originally isotropic flux by a magnetic field." [2]. However, we show in Chapter 7 that quadrupole and dipole patterns can arise from the originally isotropic flux due to the influence of Galactic magnetic field.

It is worth mentioning that the PAO observed a middle-scale anisotropy for events above 58 EeV around Centaurus A ($\sim 18°$) at the level of $\sim 3\sigma$ significance [55]. The TA published an indication of an intermediate-scale anisotropy of cosmic rays above 57 EeV found at right ascension $\alpha \sim 147°$ and declination $\delta \sim 43°$ (diameter $\sim 30° - 40°$) [56] with local significance $\sim 5\sigma$. Moreover, recently the PAO performed a correlation analysis with star burst galaxies where an interesting signal at the level of $\sim 4\sigma$ was observed, however, this significance

was calculated without a penalisation for a catalogue scan [57].

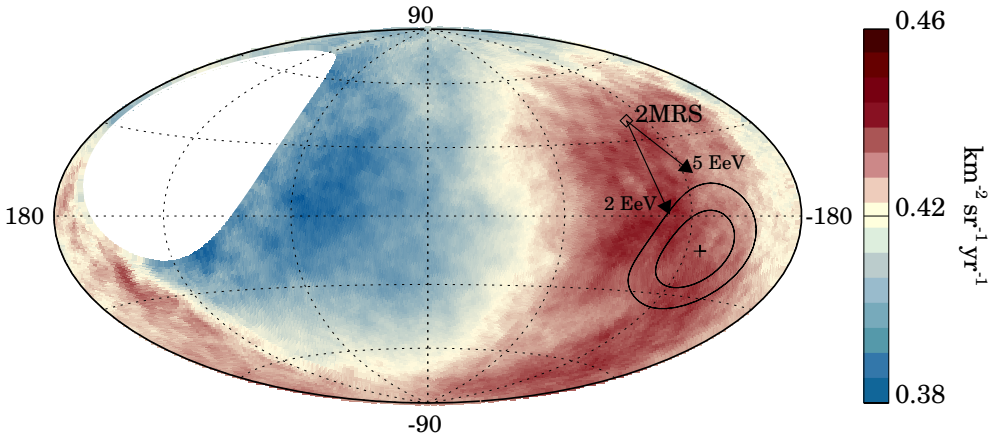

Figure 4.9: Distribution of events with energies $E > 8$ EeV in galactic coordinates smoothed with a 45° top-hat function. The cross represents the direction of the measured dipole and the contours denote the 68% and 95% confidence level regions. The dipole in the 2MRS galaxy distribution is indicated. Arrows show the deflections expected for particles with E/Z = 5 EeV or 2 EeV in the JF12 model of GMF [2].

Chapter 5

Simulation of Propagation of Cosmic-ray

The UHECR are thought to be of an extragalactic origin. This hypothesis is supported by the fact that the galactic plane does not correlate with arrival directions of the particles with energies above $\sim 10^{18}$ eV as the arrival directions are rather isotropic. Since the high-energetic particles most likely travel long distances from their sources to the Earth (in orders even tens of Mpc) the original particles from the source might noticeably differ from the ones we observe on Earth because of the processes described in Section 3.1. For that reason, simulation frameworks are being developed for the propagation of UHECR. One of them is CRPropa that was used for purposes of this thesis and it will be briefly described in the following section. Another code used by the cosmic-ray community, SimProp, is presented in this chapter as well.

5.1 CRPropa

CRPropa is a publicly available code to simulate the propagation of UHECR in the Universe. We used the newest version of the code CRPropa 3 [38]. CRPropa 3 is written in C++ and interfaced into Python. SWIG allows to work with both Python scripts and custom or existing C++ modules [38]. The simulation is divided into modules where the separate properties of the simulation are set, such as properties of the source, properties of the observer, included particle interactions etc. The individual modules are mutually independent in most of the cases and are combined in the simulation to create the required environment. The modular structure is visualised in Figure 5.1.

User can set what kind of interactions will be included in the simulation as well as the type of photon background that will be used. CRPropa can in-

clude interactions on CMB and EBL, which is divided into infra-red background ("IRB") and radio background. The spectral shape of the CMB is well known, but IRB is not that well measured and user can choose from multiple models in the simulation. In this work, the default model of IRB Dominguez 2011 [58] was used.

The following interactions are included in CRPropa 3: photo-pion production, electron-pair production, photodisintegration of the nucleus, nuclear decay and cosmological redshift. While energy losses by photodisintegration of nucleus and photo-pion production are calculated from the cross sections of given processes, the electron-pair production is approximated as a continuous energy loss given by its low energy threshold. The code can also be used for tracking neutral secondary particles (photons and neutrinos) originating from charged cosmic rays.

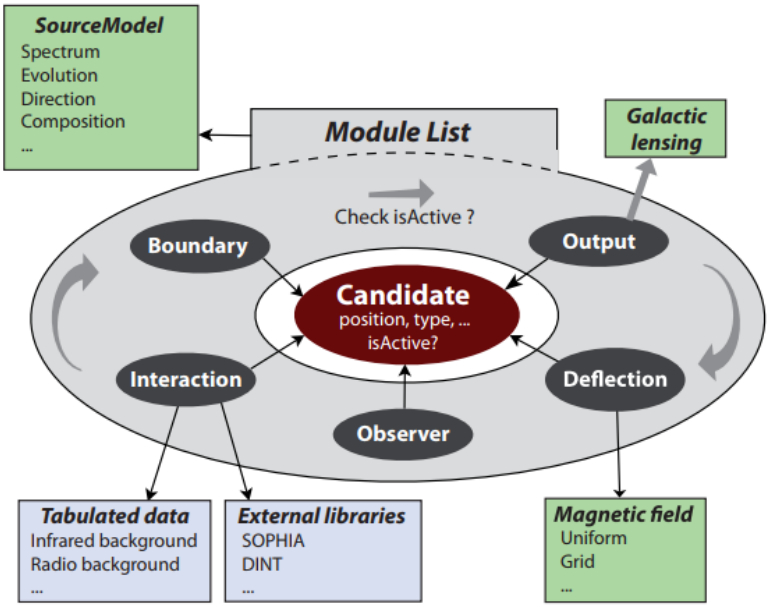

Figure 5.1: Illustration of the CRPropa 3 modular structure [38].

Simulations can be run in one-dimensional, three-dimensional or four-dimensional mode. In the one-dimensional simulation, the deflections by magnetic fields are not taken into account, only the aforementioned interactions with ambient photons cause energy losses and/or a change of the type of particle. The source or multiple sources are placed on a line in a negative x and particles propagate in a positive direction along x to the observer point placed

at $x = 0$. The output is a set of positions, energies, types of nuclei and travelled distances either at each step of the propagation or only at the observer.

Three-dimensional simulations include the effects of magnetic fields. The path and properties of the injected particle and its secondaries are calculated from Lorentz equations and interactions with ambient photons. In this case, user sets features of his observer. Depending on an investigated phenomenon, one can detect particles, for example, when they hit a sphere with a given radius (object ObserverSmallSphere()), when they leave a sphere with a given radius (object ObserverLargeSphere()) or one can detect all particles (object ObserverDetectAll()). Since the distances between the sources and observer are in orders of Mpc, the observer is usually simulated as an observer sphere of a quite large radius so that sufficient amount of particles can reach it. The output information is much more extensive than in the case of one-dimensional mode. Output file can include type of the nucleus, its energy, position and unit momentum vector together with the serial number of particle in the simulation at the source, at the origin of the particle (differs from the source in case of secondary particles) and at current position. Travelled distance and redshift are also included in the output file.

Another approach used in the three-dimensional simulation of galactic propagation is the backtracking of cosmic rays with opposite charge from the observer to the edge of the Galaxy, which reduces the computational time since all the particles are included in the final output. In this case, the energy losses including photodisintegration of nucleus are neglected. This, however, if used only for galactic propagation, is an acceptable approximation since the energy loss lengths are rather of orders of Mpc.

A four-dimensional mode of the simulations can be used when multiple sources with large differences of their distances are used. In this mode user sets a so called redshift window, corresponding to a time interval in which particles hitting the observer will be detected. This mode serves for extensive simulations where the time of detection must be taken into account.

CRPropa 3 can simulate any custom magnetic field including galactic and extragalactic magnetic fields. Some models of galactic magnetic fields are implemented into the simulation code and can be easily used by the user including Jansson & Farrar model and Pshirkov 2011 model, both described in Chapter 3.

An example of a simple python script of a one-dimensional simulation in CRpropa is depicted below. It is a simulation propagating $10,000$ helium nuclei from a uniform distribution of sources in distances between 10 Mpc and 100 Mpc with a power law energy spectrum of injected particles with spectral index $\gamma = 3$ from minimal energy 1 EeV up to the maximal rigidity 100 EeV. The initial

redshift of the injected particle is determined by the source distance. Only interactions on CMB are allowed in this script and all particles that fall under $E = 0.5$ EeV are excluded from the simulation.

```
from crpropa import *

simulation = ModuleList()
simulation.add( SimplePropagation(100*pc,1000*pc))
simulation.add( PhotoPionProduction(CMB) )
simulation.add( ElectronPairProduction(CMB) )
simulation.add( PhotoDisintegration(CMB) )
simulation.add( NuclearDecay() )
simulation.add( RedShift() )
simulation.add( MinimumEnergy(0.5 * EeV) )

obs = Observer()
obs.add( ObserverPoint() )
output = TextOutput( 'output.txt', Output.Event1D() )
obs.onDetection( output )
simulation.add( obs )

src = Source()
src.add( SourceUniform1D(10 * Mpc, 100 * Mpc) )
src.add( SourceRedshift1D() )
src.add( SourceParticleType(nucleusId(4,2)) )
src.add( SourcePowerLawSpectrum(1 * EeV, 100 * EeV, -3) )

simulation.run(src,10000,True)
```

5.2 SimProp

Another simulation code for the UHECR propagation is SimProp [59]. SimProp is a one-dimensional algorithm where magnetic fields are not included into computations and only interactions with CMB and EBL are influencing the propagated particle state.

Protons simulated with SimProp interact only with CMB in the form of electron pair production and photo-pion production. Interaction of protons with EBL are neglected due to their low probability. Heavier nuclei interact on CMB by electron-pair production and on both CMB and EBL by photodisintegration

of nucleus. Photo-pion production is neglected for heavier nuclei since its cross-section decreases linearly with atomic number. Differences between SimProp and CRPropa given by different interactions arise only for high energies (Lorentz factor $\Gamma > 10^{11}$ corresponding to energy $\approx 10^{20}$ eV for proton) and result in differences in the energy spectra.

Beside protons, the code can simulate propagation of nuclei of atomic number $A = 2$ up to $A = 56$ with one stable isotope for each atomic mass. Unstable nuclei $5 \leq A \leq 8$ are excluded. The computations of particle properties during propagation are based on the continuous energy loss approximation or an exact conservation of the particle's Lorentz factor in the photo-disintegration process. The code also includes the adiabatic energy loss over time due to the expansion of the Universe given by equation (3.7) or in the case of change of the Lorentz factor Γ

$$-\frac{1}{\Gamma}\left(\frac{\mathrm{d}\Gamma}{\mathrm{d}t}\right)_{\text{adiabatic}} = H(z), \tag{5.1}$$

where $H(z) = H_0\sqrt{(1+z)^3\Omega_\mathrm{m} + \Omega_\lambda}$ is the Hubble parameter at red-shift z, $H_0 = 71$ km/s/Mpc is the Hubble constant, $\Omega_\mathrm{m} = 0.24$ is the density of matter, both visible and dark, and $\Omega_\lambda = 0.72$ corresponds to the density of dark energy. These values are taken from WMAP data [60].

The code is developed in C++. Initial parameters of the Monte Carlo simulations are red-shift of the source, type of the primary nucleus and injection energy at the source. The code computes the propagation in steps of red-shift in one dimension up to the observer at red-shift equal to zero. The scheme of simulation procedure in SimProp is shown in Figure 5.2. SimProp follows propagation of the original nuclei and its secondary nuclei and protons created by photodisintegration. Particles are following a branch of the code where all of the interactions happen and the energy and/or the type of nucleus changes. This process continues in steps down to $z = 0$ corresponding to the observer. The intervals in red-shift have an exponentially decreasing size towards the source, or to the original point of the nucleus creation.

The output is in the form of ROOT file containing information about the propagation in individual branches with information about the branch, the energy of particle, the mass and the charge of nucleus, the initial and final energy and red-shift, the number of interactions passed by the current particle and the distance covered in the current step [59].

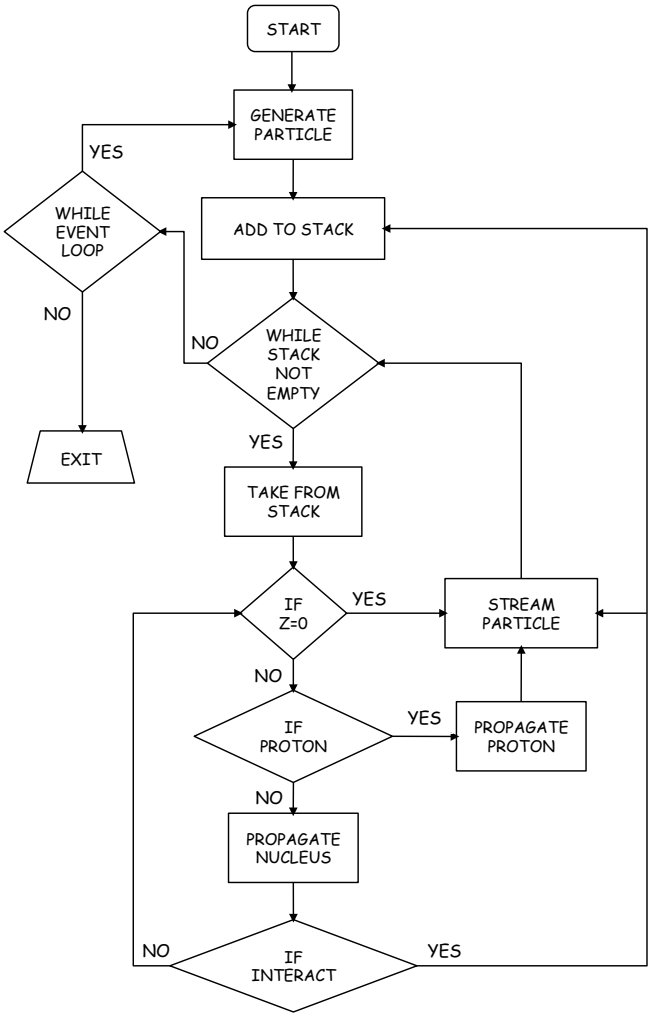

Figure 5.2: Simulation procedure in SimProp [59].

Chapter 6

The Very End of the Cosmic-ray Energy Spectrum

The data of the very end of cosmic-ray energy spectrum measured by the Pierre Auger Observatory and the Telescope Array do not coincide as it was described in Section 4.3. Both of the experiments are located on different hemispheres and therefore it is possible that this disagreement might not be caused by technical differences between the experiments, such as differences in air shower reconstructions, different measured components of air showers or different energy scales, but rather by observation of different sources capable to accelerate particles up to the highest energies. In our simplified model, we proposed a question, if the very end of energy spectrum ($\log(E/\mathrm{eV}) \geq 19.5$), as measured by the Pierre Auger Observatory, could be explained by a single source? And if so, what properties should such a source possess?

6.1 Simulations and Data

Simulations of cosmic-ray propagation were produced using the one-dimensional mode of CRPropa 3. Single sources were placed in distances from 3 Mpc to 100 Mpc, in a step of 1 Mpc up to the distance 10 Mpc and in a step of 10 Mpc farther off. We assumed 4 types of injected nuclei at the source: proton, helium (^{4}He), nitrogen (^{14}N) and iron (^{56}Fe). Simulation for a given distance of the source and type of nuclei contained $10,000$ primary particles. These particles were injected with power law energy spectrum of spectral index $\gamma = 2$ up to a maximal rigidity of $\log_{10}(R_{\mathrm{max}}/\mathrm{V}) = 20.5$.

Simulations were processed in such a way that the energy spectra at the source were in the form of a power law of energy E with a broken-rigidity

exponential cutoff:

$$\frac{\mathrm{d}E}{\mathrm{d}N} = E^{-\gamma} \cdot f_{\mathrm{cut}} \tag{6.1}$$

where γ is the spectral index and f_{cut} is the rigidity exponential cutoff function defined for a given rigidity cutoff R_{cut} as

$$f_{\mathrm{cut}} = \begin{cases} 1 & (E < ZeR_{\mathrm{cut}}) \\ e^{\left(1-\frac{E}{ZeR_{\mathrm{cut}}}\right)} & (E > ZeR_{\mathrm{cut}}) \end{cases}, \tag{6.2}$$

where Z is the proton number of the primary particle, see e.g. [21]. The exponential rigidity cutoff was used as an approximation of a steep vanishing of particles at the highest energies, which assumes the electromagnetic means of their acceleration.

Injected four types of particles were mixed with a step of 10% for all possible combinations of four primaries, which makes the total number of 286 combinations for all 17 simulated distances for each γ and each R_{cut}. Individual combinations of injected particles for a given distance of the source were subsequently weighted to obtain different spectral indices γ of the source and different rigidity cutoffs R_{cut}. The rigidity cutoff was chosen from $\log(R_{\mathrm{cut}}/\mathrm{V}) = 20.5$ down to $\log(R_{\mathrm{cut}}/\mathrm{V}) = 18.0$ in steps of 0.1. However, at the lower limit of R_{cut} the energy spectrum at the source in the investigated energy range $\log(E/\mathrm{eV}) = (19.5 - 20.2)$ becomes dominated by the exponential cutoff and no longer follows the predicted power-law dependence. Investigated spectral indices obtained by reweighting the simulated energy spectrum were in the range $\gamma \in < -1.0, 5.0 >$ in steps of 0.5.

Simulated data were compared with the combined energy spectrum measured by the Pierre Auger Observatory (taken from [52]) from energy $\log(E/\mathrm{eV}) = 19.5$ to $\log(E/\mathrm{eV}) = 20.2$ in 7 bins in steps of the logarithm of energy 0.1. Data of the combined energy spectrum measured by the PAO in the investigated energy range are listed in Table 6.1.

6.2 Comparison of Simulations and Data

Since we are interested only in the shape of the energy spectrum, the measured energy spectrum was scaled in a way that the first bin corresponds to the value of 1.0. Simulated energy spectra for all the combinations of γ, R_{cut}, distances of the source and composition of injected particles were scaled to the measured spectrum in the first bin. In order to quantify which of our simulations are in a good agreement with the measured data a quantity L was defined as

Centre of energy bin ($\log_{10}(E/\mathrm{eV})$)	$E \cdot J$ [$\mathrm{m^{-2}s^{-1}sr^{-1}}$]
19.55	$1.42 \cdot 10^{-15} \pm 5.30 \cdot 10^{-17}$
19.65	$7.60 \cdot 10^{-16} \pm 3.96 \cdot 10^{-17}$
19.75	$3.30 \cdot 10^{-16} \pm 2.50 \cdot 10^{-17}$
19.85	$1.49 \cdot 10^{-16} \pm 1.71 \cdot 10^{-17}$
19.95	$4.45 \cdot 10^{-17} \pm 1.06 \cdot 10^{-17}$
20.05	$2.33 \cdot 10^{-17} \pm 7.01 \cdot 10^{-18}$
20.15	$9.66 \cdot 10^{-18} \pm 6.77 \cdot 10^{-18}$

Table 6.1: Measured data by the PAO of cosmic-ray flux multiplied by energy E in energy bins $\log_{10}(E/\mathrm{eV})$ with a step of 0.1 at the highest energies [52].

$$L = \sum_{i}^{N_b} \frac{|x_i^{\mathrm{MC}} - x_i^{\mathrm{data}}|}{\sqrt{((\sigma_i^{\mathrm{MC}})^2 + (\sigma_i^{\mathrm{data}})^2)}}, \tag{6.3}$$

where N_b is the number of bins, x_i^{MC} and x_i^{data} are values in the ith bin of the simulated energy spectrum and measured data, respectively, and σ_i^{MC} and σ_i^{data} are respective uncertainties. For better insight, L-reduced was defined as

$$L_{\mathrm{red}} = \frac{L}{N_b - 1}. \tag{6.4}$$

Energy spectrum was calculated for each set of R_{cut} and γ for all distances and possible compositions and subsequently compared with the data measured by the PAO from Table 6.1 in the means of L_{red} evaluation. Upper value of L_{red} that still corresponds to an energy spectrum describing the measured data well was chosen to be $L_{\mathrm{red}} = 1.0$. Another cut requesting that the simulated spectra have to contain particles in all energy bins ($19.5 \leq \log(E/\mathrm{eV}) \leq 20.2$) was also applied to exclude some solutions that did not contain any particles in the last energy bin.

6.3 Results

Some of the source parameters have a substantial impact on the resulting energy spectrum and some are not that crucial. In the following paragraphs, the most important trends are highlighted and the relations between individual parameters of simulations are presented. The more detailed scan over the source

parameters and observed cosmic-ray properties is provided in the Appendix A of this thesis.

Firstly, there is a close connection of the rigidity cutoff and the spectral index of the source. Values of both variables are usually predicted by models of UHECR acceleration at their sources. A dependency of the value of L_{red} on spectral index γ and rigidity cutoff R_{cut} is depicted in Figure 6.1 for $\gamma = (-1.0, 5.0)$ and in Figure 6.2 for $\gamma = (-1.0, 3.0)$. Coloured scale represents the minimal value of L_{red} found for given γ and R_{cut} set. The regions of dark contours represent combinations of rigidity cutoff and spectral index of the source that have appropriate conditions to describe well the data measured by the PAO.

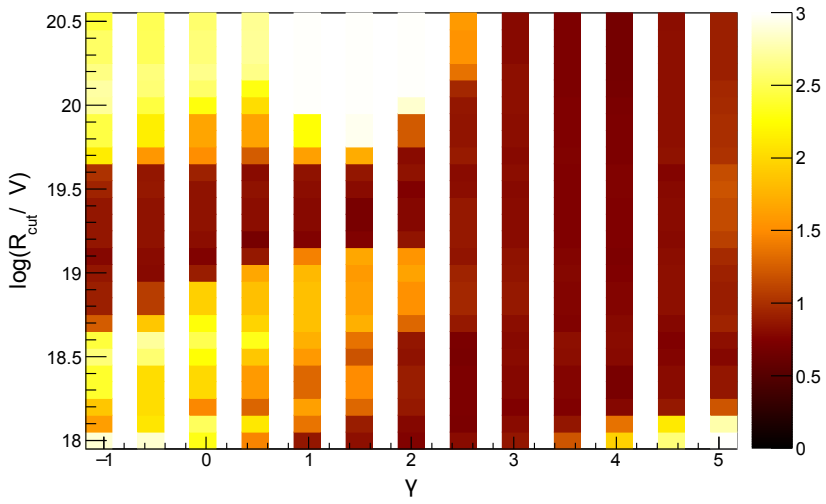

Figure 6.1: Minimal value of L_{red} (represented in colour) for given combination of spectral index γ and rigidity cutoff R_{cut}.

High values of spectral indices (3.5-5.0) describe the measured energy spectrum well in almost the whole range of R_{cut} for at least one combination of primaries and source distance (see Figure 6.1), except for the lowest R_{cut}. This is probably caused by the closeness of spectral indices of the measured data by the PAO ($\gamma \sim 4.8$) and simulated energy spectra. Such high values of γ are not usually predicted by the astrophysical models of particle acceleration (see Section 2.3) and they will not be considered any further in this work. Another solutions that will not be further considered are the solutions for $\log(R_{\mathrm{cut}}/\mathrm{V}) \leq 18.5$ since at the lowest rigidity cutoffs the energy spectra at the source are no longer in the form of power law but their shape in the investigated energy range is dominated by the exponential cutoff function. In these cases, predominantly the exponential cut-off shape was compared with the measured data as the

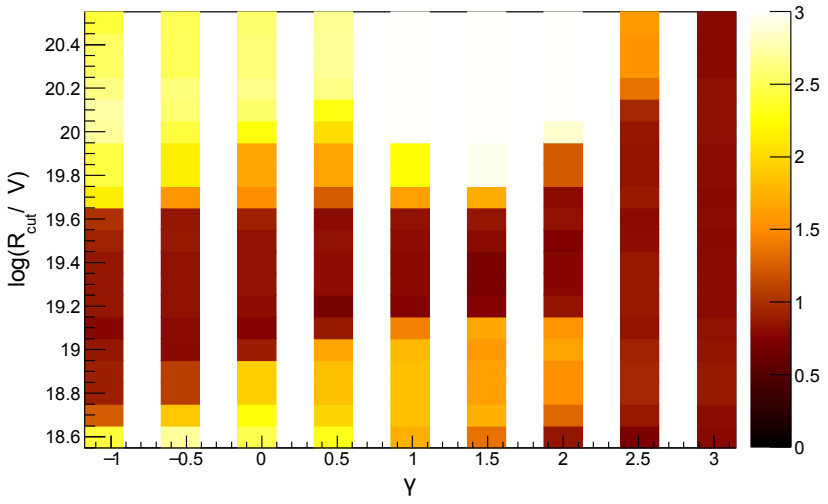

Figure 6.2: Minimal value of L_{red} (represented in colour) for given combination of spectral index γ and rigidity cutoff R_{cut}.

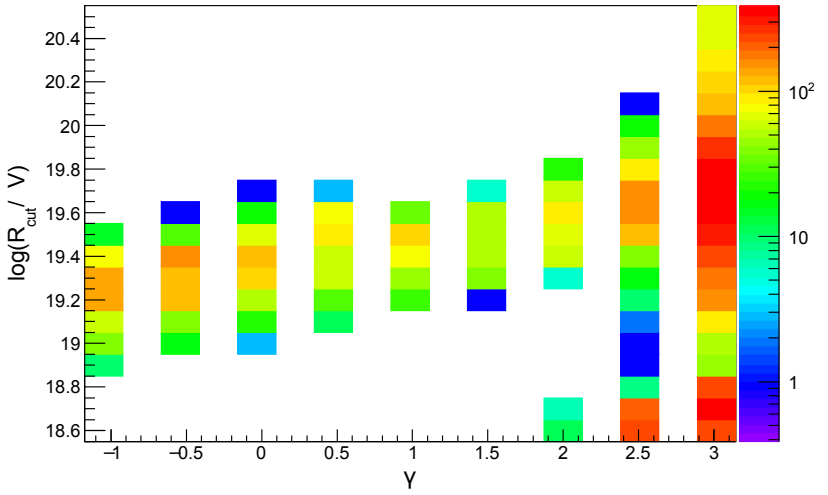

Figure 6.3: Number of possible solutions ($L_{\mathrm{red}} < 1$) for combinations of spectral index γ and rigidity cutoff R_{cut}.

power-law behaviour produced particles up to energies $\sim Z \cdot R_{\mathrm{cut}}$. This corresponds to maximal energy $\log(E/\mathrm{eV}) \sim 19.9$ for irons and $\log(E/\mathrm{eV}) \sim 19.3$ for nitrogen nuclei in the case of $\log(R_{\mathrm{cut}}/\mathrm{V}) = 18.5$.

The values of L_{red} for combinations of γ in the range (-1.0,3.0) and R_{cut} are

shown in Figure 6.2 and the number of passed solutions for combinations of γ and R_{cut} are illustrated in Figure 6.3. We can see that each individual spectral index could describe the measured energy spectrum well for some range of R_{cut}. Spectral index $\gamma = 3$ is the only one that can fulfil the applied cuts at all considered rigidity cutoffs. However, as it was mentioned in Section 2.3, theories of UHECR acceleration mechanisms usually incline rather to lower spectral indices, either around $\gamma = 1$ or to spectral indices around $\sim 2.0 - 2.5$ predicted in theories based on the Fermi's first order acceleration. These values of spectral indices actually narrow the possible maximal rigidity of the source $\log(R_{\mathrm{cut}}/\mathrm{V}) \sim 18.9 - 19.8$.

Similar analysis was previously done in [21] where data were investigated in the energy range $18.7 < \log(E/\mathrm{eV}) < 20.2$. Deviances from the data of the best fit depending on the spectral index and maximal rigidity of sources are shown in Figure 6.4. Our results illustrated in Figure 6.2 differ. In our results, regions of best agreement with the data for given γ are generally shifted to higher maximal rigidities of the source and for higher spectral indices there are wider ranges of possible R_{cut} of the source. These differences are caused by different investigated energy ranges and also due to the fact that results obtained in [21] come from a combined fit of both energy spectrum and mass composition on Earth. Moreover, multiple sources distributed homogeneously were taken into account in contrast to single source scenario adopted in this thesis.

Another parameter of the simulations is the distance of the source. An illustration of the finest match between measured and simulated energy spectra throughout all spectral indices (-1.0-3.0) in terms of L_{red} is demonstrated in Figure 6.5 for combinations of rigidity cutoff and source distance. Information about the number of possible solutions for individual combinations of rigidity cutoff and source distance is shown in Figure 6.6. Overall, close sources are more likely to describe the measured energy spectrum by the PAO well rather than the distant sources since the probability that particles with energies above 10^{20} eV would reach the Earth decreases with their energy. Nevertheless, there are some solutions for distant sources as well in the region of maximal logarithm of rigidity of the source from $\log(R_{\mathrm{cut}}/\mathrm{V}) \sim 19.0$ to $\log(R_{\mathrm{cut}}/\mathrm{V}) \sim 19.8$, including even the most distant sources placed at distance 100 Mpc. Considering extragalactic magnetic fields in the simulations would increase the travelled distance of cosmic rays and restrict the source distance even more.

The number of solutions for individual spectral indices and source distances is plotted in Figure 6.7 for accepted solutions. Similarly to the previous relation of the rigidity of the source and the source distance, also Figure 6.7 indicates that close sources are preferred compared to farther ones. Generally, with increasing distance of the source and decreasing spectral index, there are fewer possible

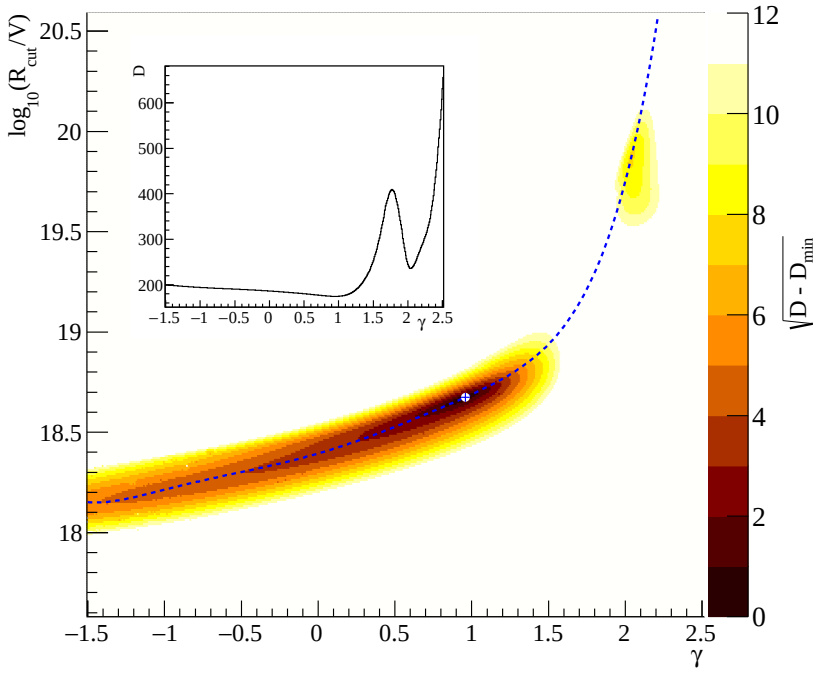

Figure 6.4: Deviance from the data of the best fit as a function of γ and logarithm of R_{cut} [21].

solutions describing the measured data well.

Figure 6.8 shows the number of solutions for the mean logarithmic mass at the source and different rigidity cutoffs. Four distinct regions of possible solutions are formed. Three of these regions have their maximum of passed solutions in the vicinity of $< \ln \mathrm{A} >_{\mathrm{source}}$ of single primaries, either helium, nitrogen or iron nuclei. Only few solutions of single protons are found for a narrow range of R_{cut}. Neither extremely heavy or extremely light composition at the source is predicted for the highest R_{cut}. Another island of solution is located between the atomic mass of nitrogen and iron for lower maximal rigidities of the source.

The number of solutions for combination of the mean logarithmic mass and different spectral indices is visualised in Figure 6.9. Spectral indices $\gamma < 1$ predict also solutions of pure iron nuclei at the source; such solutions are not found for higher spectral indices. No obvious development of the mass composition at the source with the spectral index is found.

The number of solutions for combination of the mean logarithmic mass source distance is depicted in Figure 6.10. This figure again indicates that close sources

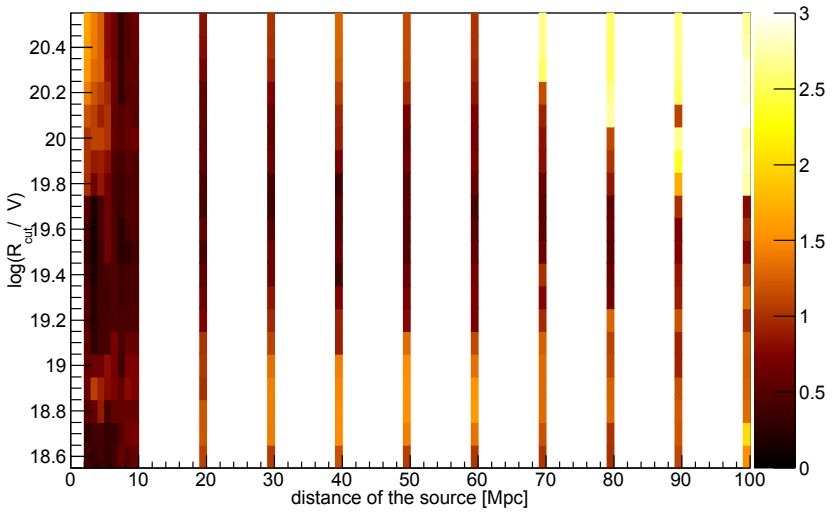

Figure 6.5: Minimal L_{cut} for combinations of rigidity cutoff and distance of the source found through all spectral indices ($\gamma = -1.0 - 3.0$) and mass compositions at the source.

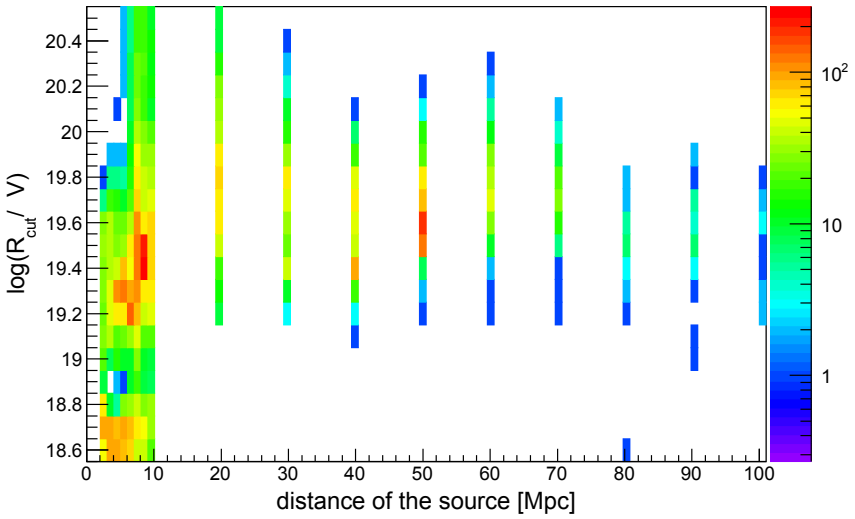

Figure 6.6: Number of possible solutions ($L_{\text{red}} < 1$) for combinations of rigidity cutoff and distance of the source found through all spectral indices ($\gamma = -1.0 - 3.0$) and mass compositions at the source.

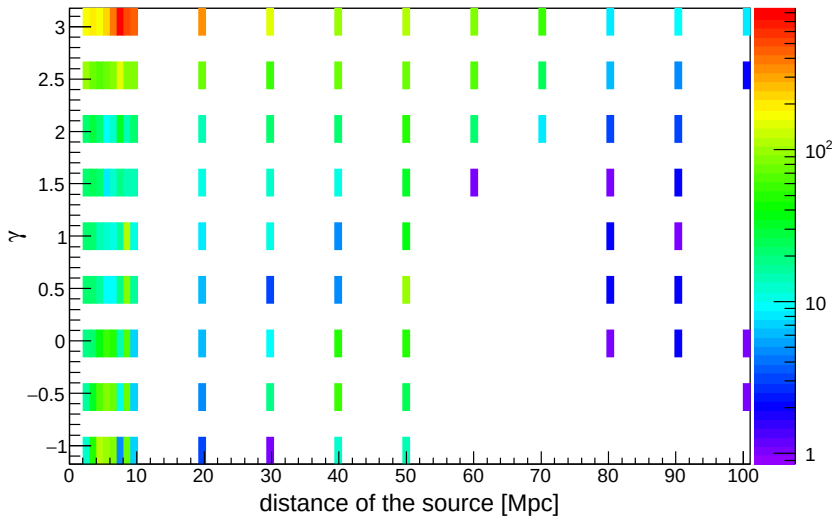

Figure 6.7: Number of possible solutions ($L_{\text{red}} < 1$) for combinations of spectral index and distance of the source found through all rigidity cutoffs and mass compositions at the source.

are more likely to describe the measured energy spectrum well. Similarly to Figure 6.8, large number of solutions is concentrated around the mean $\ln A$ of considered single primaries for close distances. The most distant sources need to be heavier ($\ln A \geq 1.7$) to describe the measured data well.

The spectral indices are divided into two groups that will be discussed separately. The first set of investigated spectral indices is $\gamma \in < 1.0 - 3.0 >$ and the second set contain spectral indices $\gamma \in < -1.0 - 0.5 >$.

Spectral Indices 1.0 - 3.0

As it was already mentioned at the beginning of this section, solutions with spectral index $\gamma = 3$ survive the cuts in the whole range of R_{cut}. Solutions with other spectral indices appear for a limited range of rigidities (see Figure 6.2).

For each rigidity cutoff, a sextuplet of plots was produced carrying a complete set of important information about all the possible solutions at given R_{cut}. Information about possible solutions for $\log(R_{\text{cut}}/\text{V}) = 20.5$ are shown in Figure 6.11, for $\log(R_{\text{cut}}/\text{V}) = 19.8$ in Figure 6.12 and for $\log(R_{\text{cut}}/\text{V}) = 19.6$ in Figure 6.13 for illustration. For a complete scan of solutions over the whole range of maximal rigidity see Apendix A. The top left plot in these figures shows all the possible energy spectra that passed the cuts for $L_{\text{red}} < 1$ together with the data measured by the PAO, different colours correspond to different spectral

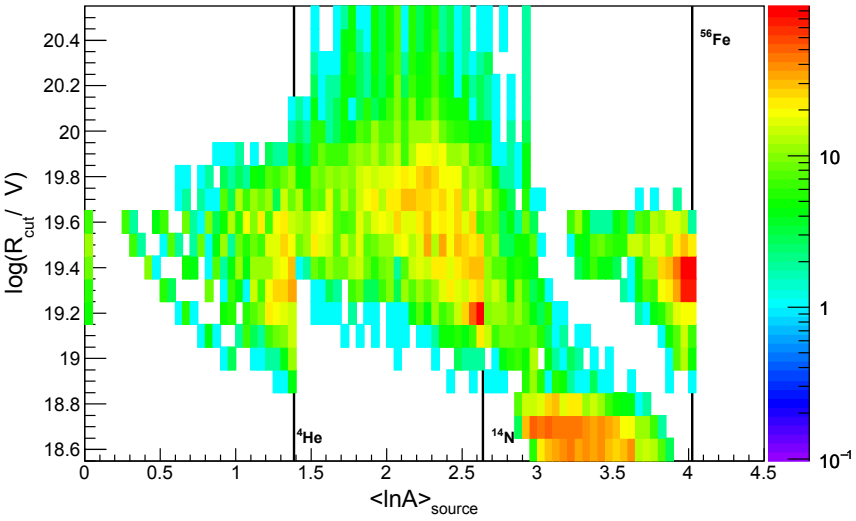

Figure 6.8: Number of possible solutions ($L_{\text{red}} < 1$) for combinations of the mean logarithmic mass at the source and different rigidity cutoffs.

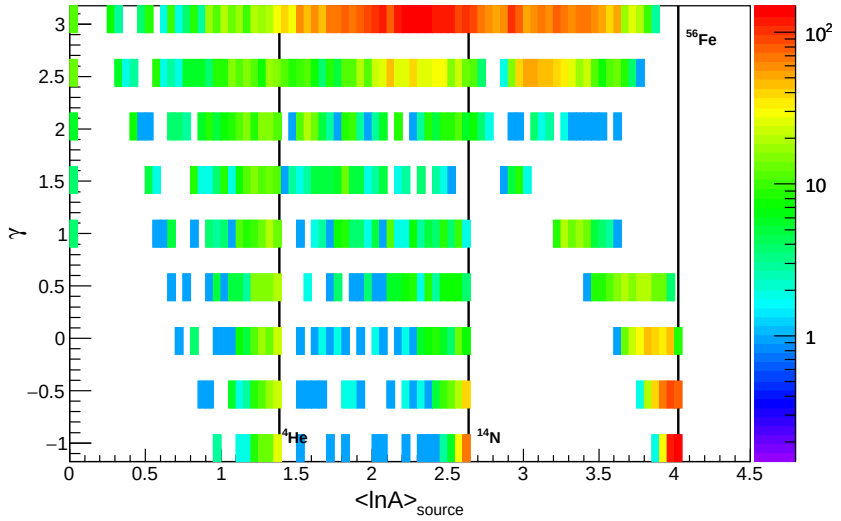

Figure 6.9: Number of possible solutions ($L_{\text{red}} < 1$) for combinations of the mean logarithmic mass at the source and different spectral indices.

indices. The top right plot visualises the evolution of the mean $\ln A$ on Earth with energy for each solution. This plot represents what energy evolution of $< \ln A >$ would be observed on Earth. The middle left figure demonstrates the

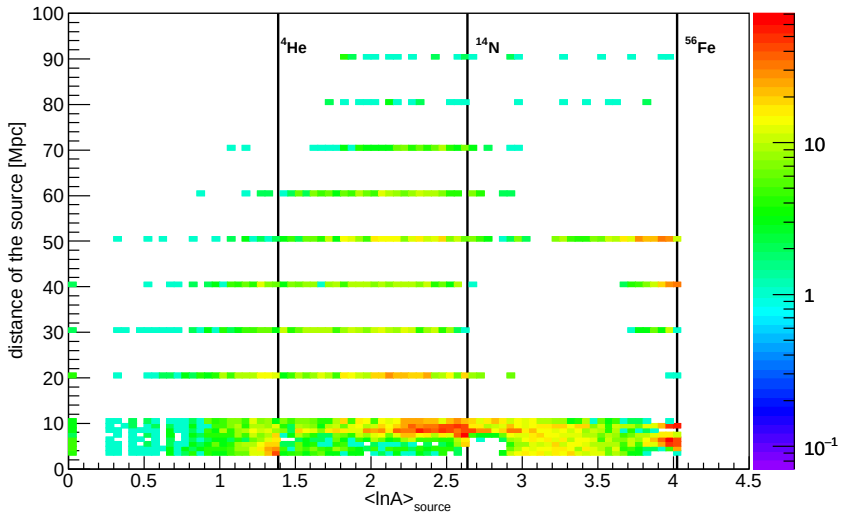

Figure 6.10: Number of possible solutions ($L_{\mathrm{red}} < 1$) for combinations of mean logarithmic mass at the source and individual distances of the source.

energy spectra for different primary particles at the source for given R_{cut}. The different energies of transition between the pure power law and the power law with exponential rigidity cutoff for individual primaries is exhibited here. The middle right plot shows the mean ln A at the source for different solutions that describe the measured energy spectrum well, which tells us if the composition at the source is rather heavy or light and how much the source is distant. The bottom left plot gives the distribution of fractions of primaries at the source of passed combinations and the bottom right plot shows values of L_{red} for all different combinations for different distances of the source. Plots for all the rigidity cutoffs are depicted in the Appendix A.

At the highest value of R_{cut} (see Figure 6.11), the energy spectrum is well described by close sources (up to 20 Mpc) with spectral index $\gamma = 3$. Mass compositions at the source that passed the cuts are mainly a mixture of nitrogen and helium with a small fraction of protons and iron nuclei.

As we go down with the rigidity cutoff, solutions with spectral index $\gamma = 2.5$ start to appear at $\log(R_{\mathrm{cut}}/\mathrm{V}) = 20.1$ (see Figure A.16) and energy spectra with $\gamma = 2.0$ pass the cuts starting at $\log(R_{\mathrm{cut}}/\mathrm{V}) = 19.8$ as depicted in Figure 6.12. Composition at the source scanned over all solutions is similar to the case of the ones at the highest R_{cut}, mainly its high fraction of nitrogen or helium nuclei with smaller fractions of protons and iron nuclei, but solutions with a large proton contribution start to appear as well. Gradually, solutions originating

also from more distant sources are passing the cuts. Solutions with $\gamma = 1.5$ and $\gamma = 1$ become part of the results at $\log(R_{\rm cut}/{\rm V}) = 19.7$ and $\log(R_{\rm cut}/{\rm V}) = 19.6$, respectively, as can be seen in Figure A.12 and Figure 6.13.

With further decrease of $R_{\rm cut}$, see Figures A.10-A.6, the individual spectral indices, except $\gamma = 3$ and $\gamma = 2.5$, are excluded from the set of possible solutions and at $\log(R_{\rm cut}/{\rm V}) = 19.1$ only solutions with $\gamma = 3$ and two solutions with $\gamma = 2.5$ for close sources emitting a mixture of nitrogen with small fractions of iron and helium nuclei remain.

For the lowest considered rigidity cutoff region (around $\log(R_{\rm cut}/{\rm V} = 18.6)$), see Figure A.2 and Figure A.1, energy spectra with spectral indices 2.5 and 2.0 both satisfy our cuts together with $\gamma = 3$ and all the passed solutions predict very heavy composition on both the source and the Earth, composed mainly of iron nuclei (see Figure 6.8). Such effect is caused by the low $R_{\rm cut}$ which results in a strong suppression of lighter primaries when compared with the iron nuclei.

The top right panel of Figure 6.12 illustrates that the evolution of mean $\ln {\rm A}$ on Earth might be decreasing or increasing with energy and even flat for light mass composition of cosmic rays arriving to the Earth. The trend of evolution of mean $\ln {\rm A}$ on Earth with energy does not depend on the spectral index, but rather on the original composition of injected particles by the source. In Figure 6.14, the mean $\ln {\rm A}$ on Earth depending on the source distance for all the possible solutions is shown for $\log(R_{\rm cut}/{\rm V}) = 19.8$ together with illustrative lines dividing the solutions into three groups: bottom, middle and top. Evolutions of the mean $\ln {\rm A}$ with energy and the fractions of primary particles emitted from the source are depicted in Figures 6.15, 6.16, Figure 6.17 for solutions in the bottom, middle and top region from Figure 6.14, respectively.

The solutions for the bottom region provide low values of the mean $\ln {\rm A}$ on Earth (see left panel of Figure 6.15), also the evolutions of the mean $\ln {\rm A}$ on Earth with energy is rather flat. These solutions come from close sources emitting mainly helium nuclei with a small fraction of protons or nitrogen nuclei. No solution in this region predicts a presence of iron nuclei at the source.

The middle region demonstrates a clear decreasing tendency of the mean $\ln {\rm A}$ on Earth with the source distance. These solutions originate from sources emitting mainly nitrogen nuclei or protons with a small fraction of helium nuclei as is depicted in the right panel of Figure 6.16. As it can be seen in the left panel Figure 6.16, the evolution of mean $\ln {\rm A}$ observed on Earth with energy is gradually decreasing. In contrast with the previous case, the composition is heavier at the source, dominated by mixed composition of nitrogen nuclei and protons.

Solutions for the top region, illustrated in Figure 6.17, result in the heaviest composition on Earth out of these three regions and they indicate an increase

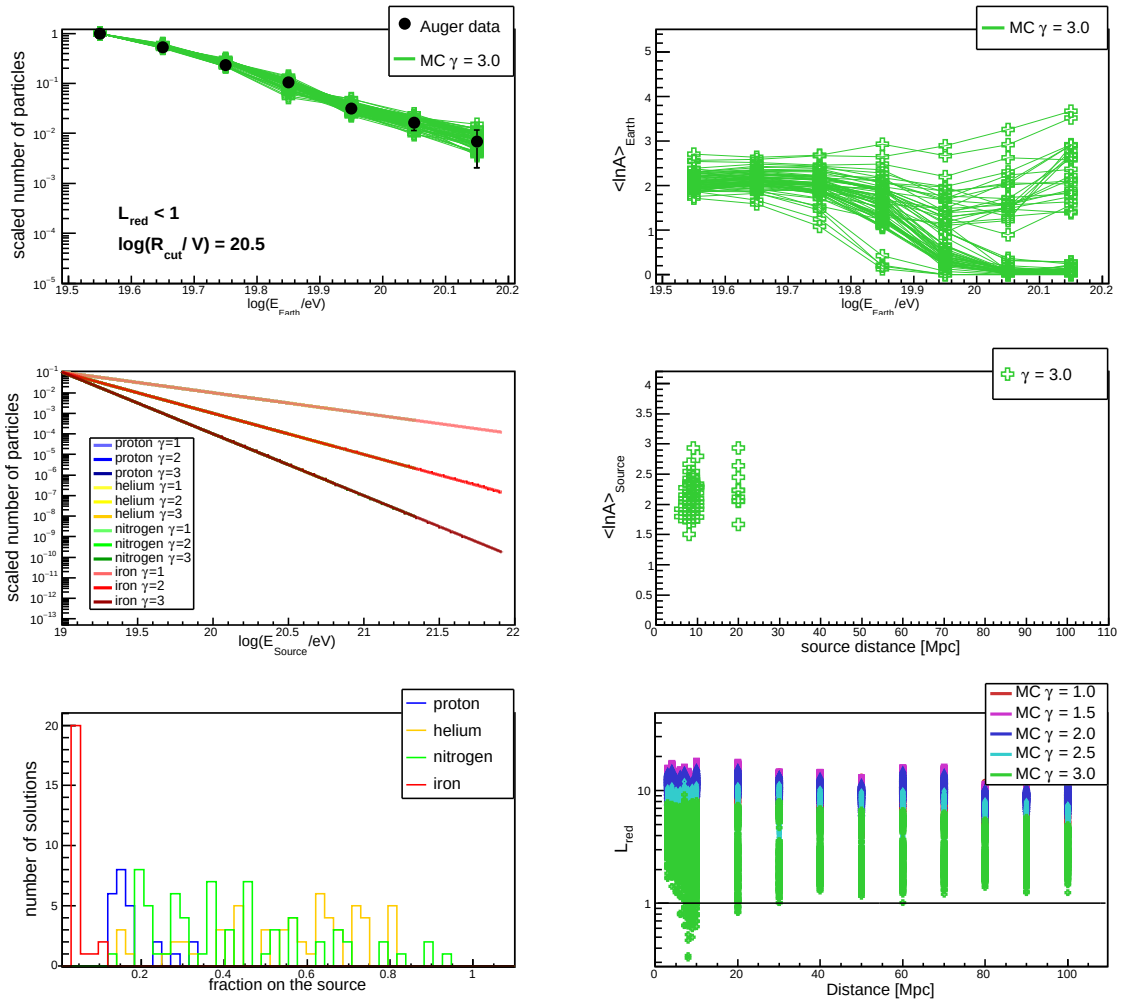

Figure 6.11: Properties of simulated energy spectra for rigidity cutoff $\log(R_{\mathrm{cut}}/\mathrm{V}) = 20.5$. Top left: Scaled energy spectra for all possible solutions with $L_{\mathrm{red}} < 1$ together with energy spectrum measured by the PAO (in black). Top right: Evolution of the mean $\ln \mathrm{A}$ on Earth with energy of individual solutions. Middle left: Scaled energy spectrum of individual primary particles at the source following equation (6.1) for given R_{cut} and different spectral indices γ. Middle right: The mean $\ln \mathrm{A}$ at the source depending on the source distance for individual solutions. Bottom left: Distribution of fractions of primary particles at the source for passed solutions. Bottom right: Values of L_{red} depending on the source distance for all combinations at given R_{cut}.

of the mean $\ln \mathrm{A}$ on Earth with energy. Such a heavy composition is caused by a small fraction of primary iron nuclei from the source that have a larger

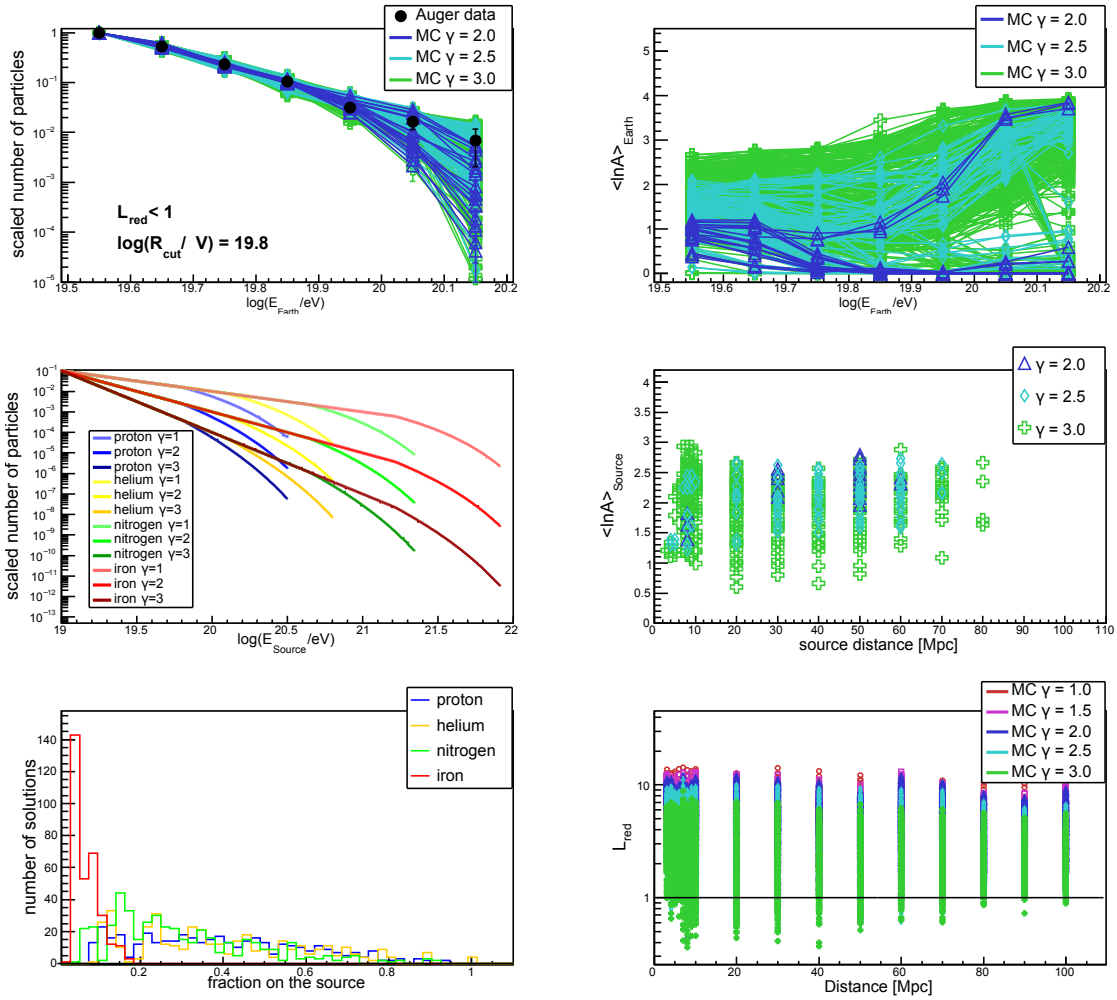

Figure 6.12: Properties of simulated energy spectra for rigidity cutoff $\log(R_{\rm cut}/{\rm V}) = 19.8$. For description see caption of Figure 6.11.

energy loss length than nitrogen (see Figures 3.1, 3.2) and therefore they are capable to arrive on Earth unchanged even from more distant sources. As the most energetic particles disintegrate, they form the light composition at lower energies, but some of them survive and create the heavy mass composition at the highest energies. Except of few solutions that predict pure protons in the last energy bin, the mass composition in the whole energy range differs from pure proton composition.

The maximal rigidity of the source, here defined as $R_{\rm cut}$, is in a close relation with the observed mean ln A at the source for the case of $\gamma = 3$, see middle right panels in Figures A.1-A.19 in Appendix A. With lower $R_{\rm cut}$ the composition

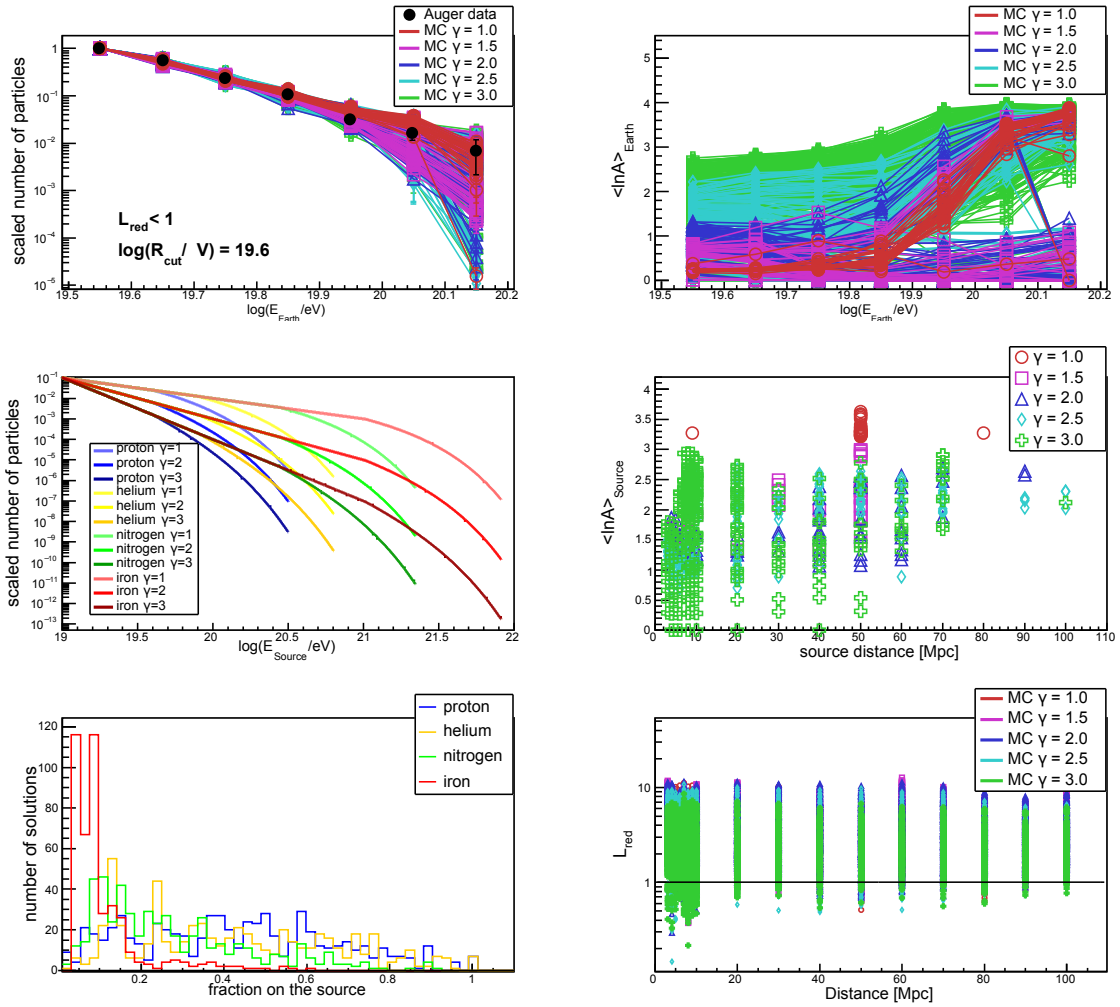

Figure 6.13: Properties of simulated energy spectra for rigidity cutoff $\log(R_{\rm cut}/{\rm V}) = 19.6$. For description see caption of Figure 6.11.

at the source is rather heavier and with increasing $R_{\rm cut}$ the mean $\ln {\rm A}$ at the source decreases. The heavy composition at the source for low $R_{\rm cut}$ is a result of a gradual drop out of lighter particles. This trend is valid up to $\log(R_{\rm cut}/{\rm V}) \approx 19.7$. For lower spectral indices ($\gamma = 1$ and $\gamma = 1.5$) this dependency seems to have an opposite behaviour. However, since the range of $R_{\rm cut}$ containing solutions for these small spectral indices is very narrow such a behaviour might be just coincidental.

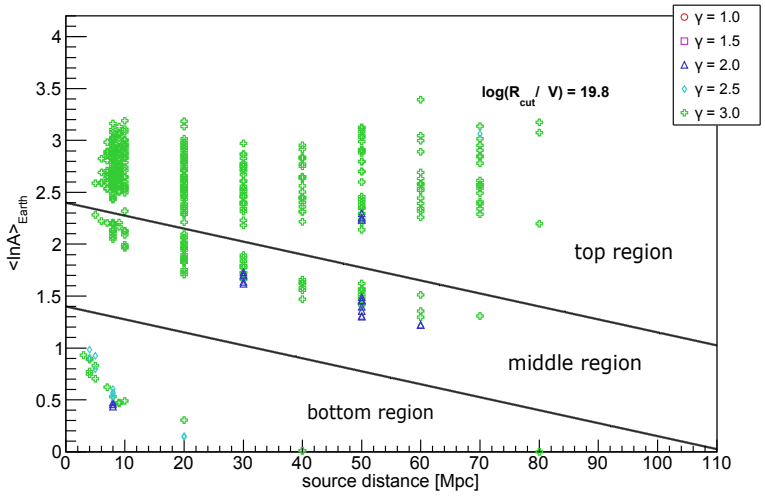

Figure 6.14: Mean ln A on Earth of all passed solutions for different source distances. Illustrative lines divide the solutions into three separate regions (bottom, middle and top) depending on the $< \ln A >$ value and its behaviour with source distance.

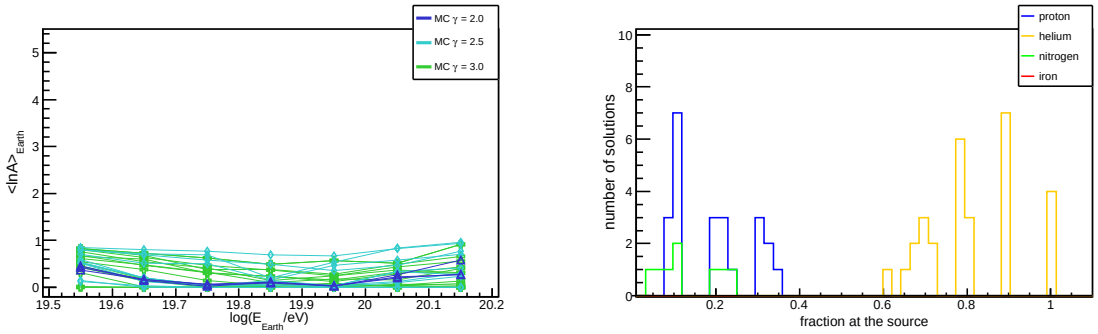

Figure 6.15: Left: Evolution of the mean ln A on Earth with energy for solutions in the bottom region from Figure 6.14. Right: Fraction of primaries at the source for all the possible solutions in the bottom region.

Spectral Indices -1.0 - 0.5

Even though the theories of particle acceleration at their sources usually predict a power law energy spectrum with spectral indices equal to 1 or larger, very small and even negative values of spectral indices are being discussed in some research works as being optimal to describe the measured energy spectrum by the PAO [21]. A set of spectral indices in the range (-1.0-0.5) was therefore examined

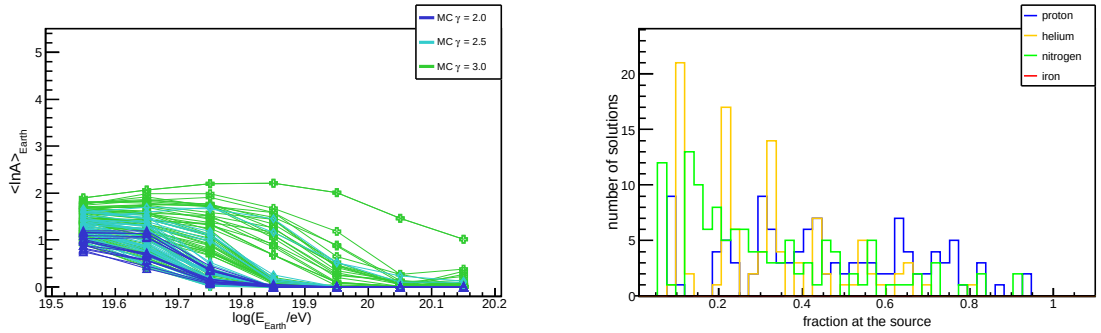

Figure 6.16: Left: Evolution of the mean ln A on Earth with energy for solutions in the middle region from Figure 6.14. Right: Fraction of primaries at the source for all the possible solutions in the middle region.

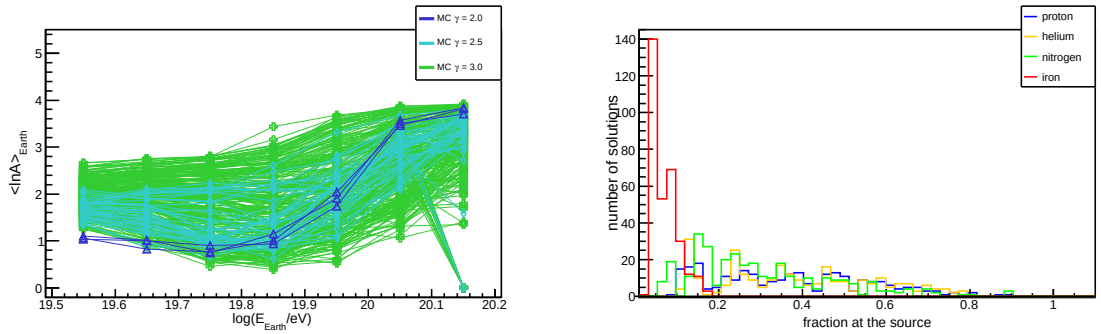

Figure 6.17: Left: Evolution of the mean ln A on Earth with energy for solutions in the top region from Figure 6.14. Right: Fraction of primaries at the source for all the possible solutions in the top region.

as well. The region of rigidity cutoffs where individual spectral indices $\gamma \leq 0.5$ pass the applied cuts and therefore describe the measured data well goes from $\log(R_{\text{cut}}/\text{V}) \cong 19.7$ down to $\log(R_{\text{cut}}/\text{V}) \cong 18.9$ as depicted in Figure 6.2.

Information about the solutions for $\log(R_{\text{cut}}/\text{V}) = 19.6$ and $\log(R_{\text{cut}}/\text{V}) = 19.1$ are shown in Figures 6.18, 6.19, respectively. Plots for other rigidity cutoffs can be found in the Appendix A. At the upper region of the possible rigidity cutoff, $\log(R_{\text{cut}}/\text{V}) = 19.7$, only solutions with spectral index 0.5 and 0.0 passed the cuts predicting a high abundance of iron nuclei at the source. Gradually, with decrease of R_{cut}, energy spectra with spectral index -0.5 and -1.0 become part of the set of solutions at $\log(R_{\text{cut}}/\text{V}) = 19.6$ and $\log(R_{\text{cut}}/\text{V}) = 19.5$. With further decrease of R_{cut}, the higher spectral indices are excluded. At the lowest R_{cut}, the spectral index -1.0 is the only one from the set describing the measured data well.

Most of the solutions at $\log(R_{\rm cut}/{\rm V}) > 19.2$ predict rather a light mass composition on Earth at lower energies as a result of photodisintegration of heavy mass composition at the source dominated by iron nuclei dominated by iron nuclei which have much longer energy loss length for photodisintegration process than lighter nuclei (see e.g. Figures 3.1, 3.2). This has a consequence of a steep increase of $< \ln {\rm A} >_{\rm Earth}$ at energies above 10^{20} eV. Most of the solutions are from very close sources (≤ 10 Mpc) or from medium distant sources (~ 50 Mpc).

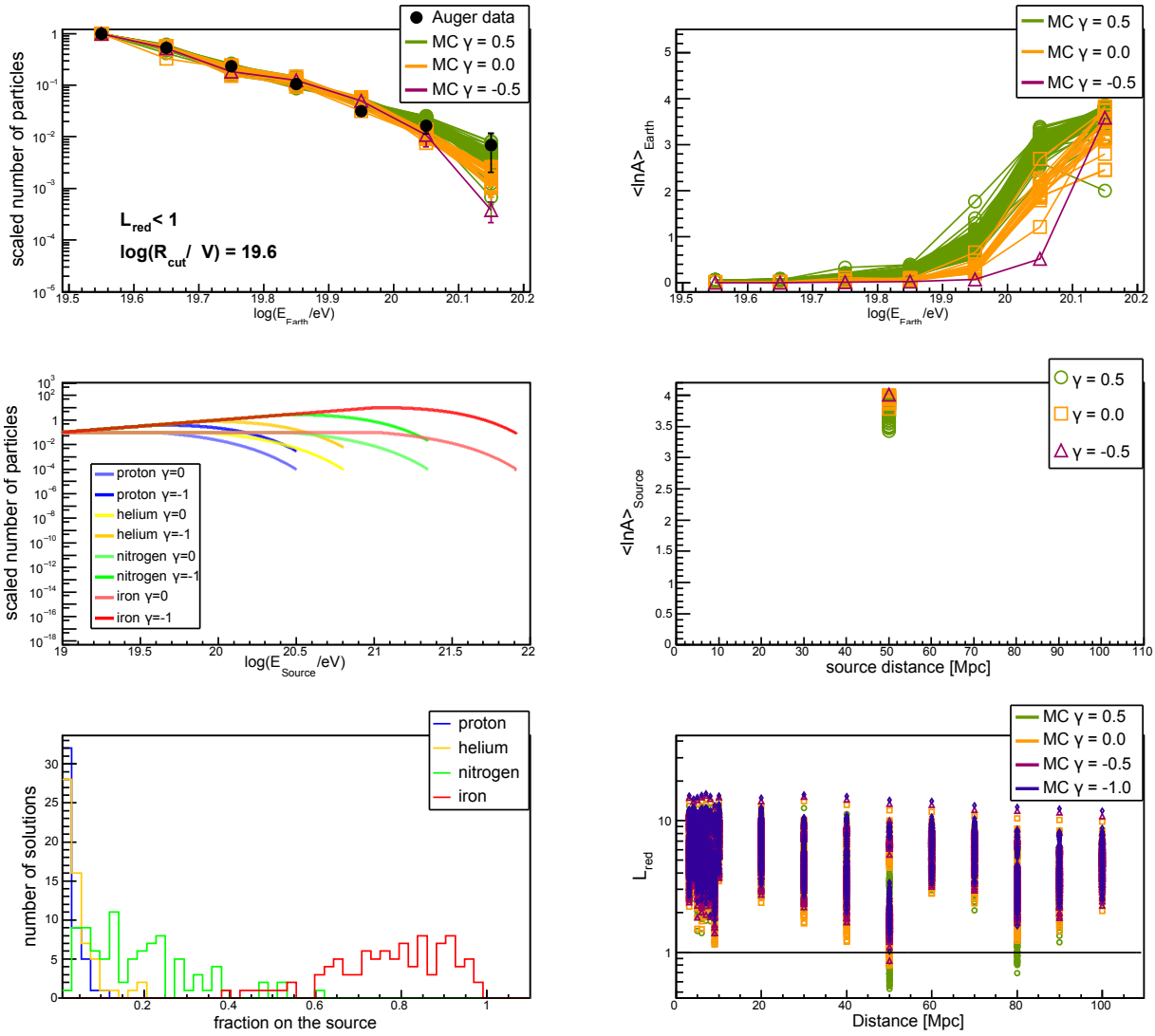

Figure 6.18: Properties of simulated energy spectra with low spectral indices for rigidity cutoff $\log(R_{\mathrm{cut}}/\mathrm{eV}) = 19.6$. For description see caption of Figure 6.11.

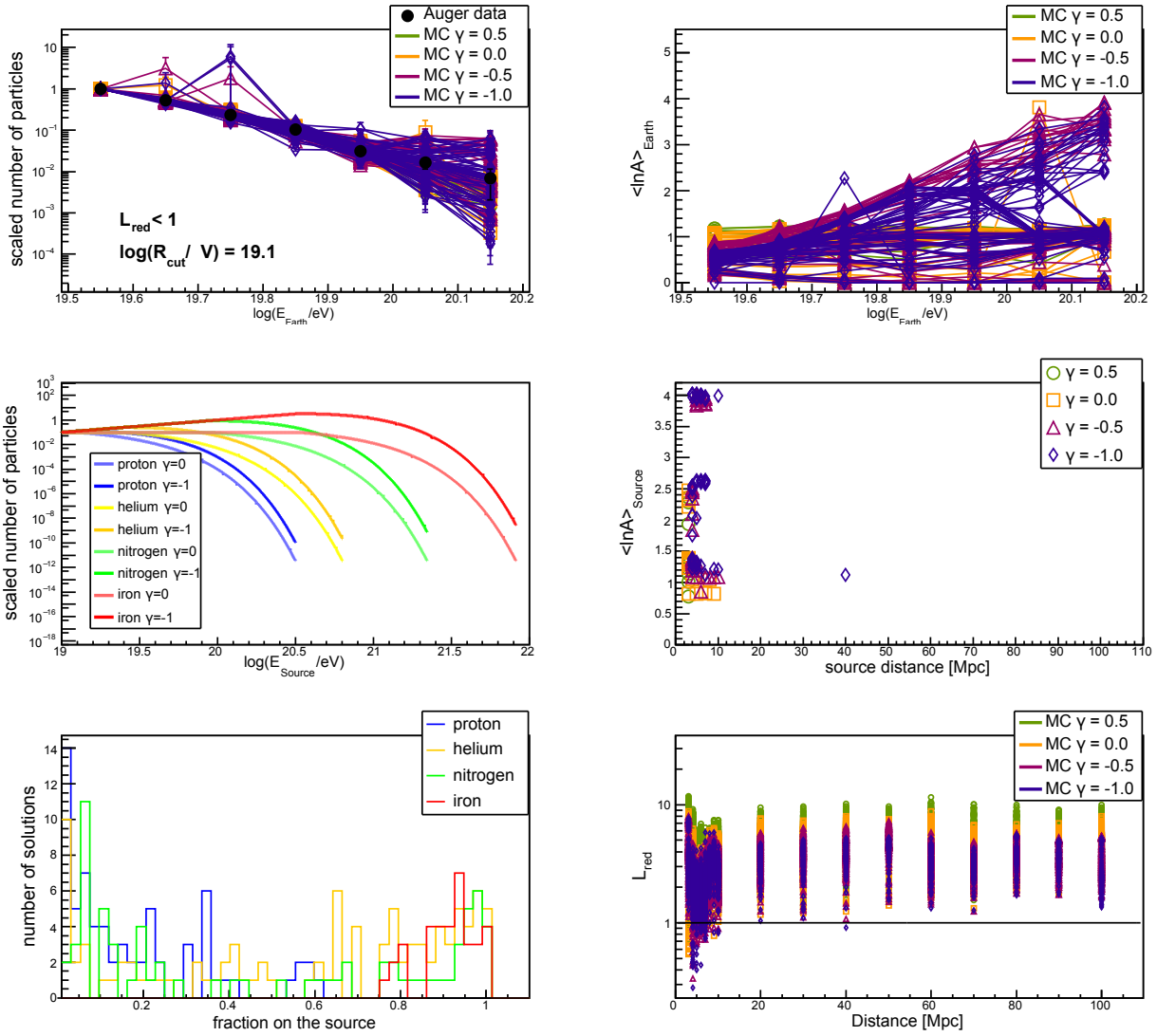

Figure 6.19: Properties of simulated energy spectra with low spectral indices for rigidity cutoff $\log(R_{\mathrm{cut}}/\mathrm{eV}) = 19.1$. For description see caption of Figure 6.11.

Chapter 7

Effects of GMF on Arrival Directions of Cosmic Rays

This chapter is dedicated to the analysis of arrival directions of isotropic extragalactic UHECR propagating in the galactic magnetic field using the simulation program CRPropa 3 (see Chapter 5). Backtracking is often used to study behaviour of UHECR in magnetic fields due to its high efficiency. However, results obtained from backtracking could be difficult to interpret in some studied effects, such as the particular case of arrival directions. As it was previously shown in [34, 61], the observer on Earth is blind to a large part of extragalactic sources of UHECR due to the galactic magnetic field. Moreover, as a result of deflections of cosmic rays by GMF, fluxes from individual sources could be magnified or demagnified and multiple images can be created similarly to gravitational lensing effects.

Following study was motivated by the observation of a large-scale anisotropy in the arrival directions of cosmic rays above 8 EeV by the PAO (described in Section 4.3). Particularly, the effects of GMF on extragalactic UHECR of different primaries were studied. The primary purpose of this work is to verify if the GMF truly conserves the isotropy of arrival directions of cosmic rays on the observer in case of an isotropic flux entering the Galaxy. For that purpose, direct simulations of extragalactic cosmic rays coming from the Galaxy border were performed.

7.1 Simulations of UHECR propagation in the Galaxy

Three-dimensional mode of CRPropa 3 was used to propagate particles from the border of the Galaxy to the observer. The Milky Way was set as a sphere

with radius of 20 kpc and the observer, a sphere with radius 100 pc[1], was placed to the position $(-8.5, 0, 0)$ kpc corresponding to the approximate coordinates of the Solar system in the Galaxy.

Particles were propagated from an isotropically emitting shell (galactic border) following a power law energy spectrum with spectral index $\gamma = 3$. The energy range of simulated particles goes from 8 EeV to 100 EeV. Three types of primary particles were simulated - protons, helium and nitrogen nuclei. A simulation including protons was also made with power law energy spectrum from 4 EeV up to 100 EeV. Inside the galactic sphere, particles are propagated in JF12 model of GMF and particles hitting the observer are detected. All three components of JF12 were used, including regular, turbulent and striated component of the magnetic field. For comparison, also the Pshirkov model of GMF was used to propagate protons and helium nuclei in the same way. For description of models of GMF see Section 3.2. Energy losses are neglected since the energy loss lengths on CMB are of orders of Mpc and more in the studied energy range.

7.2 Coordinate Transformations

CRPropa 3 saves positions and unit momentum vectors of particles hitting the observer in cartesian coordinates. The arrival direction of a cosmic ray is usually expressed in either galactic or equatorial coordinates. Galactic latitude b and longitude l can be calculated from cartesian coordinates x, y, z using transformation equations [62]

$$l = \mathrm{atan2(y, x)}, \tag{7.1}$$

$$b = \frac{\pi}{2} - \arccos\left(\frac{z}{x^2 + y^2 + z^2}\right). \tag{7.2}$$

The definition of the atan2 function can be found in [63]. The position where the particle entered the Galaxy was calculated using the original position of the particle in equations (7.1) and (7.2). The arrival direction of the particle to the observer was calculated from equations (7.1) and (7.2) using components of the reversed momentum vector of particle. Equatorial coordinates can be obtained from galactic longitude and latitude as

$$\begin{aligned}\alpha = \mathrm{atan2}[&\cos(\mathrm{b})\cos(\mathrm{l} - 122.9^\circ), (\sin(\mathrm{b})\cos(27.1^\circ) - \\ &\cos(b)\sin(27.1^\circ)\sin(l - 122.9^\circ))] + 192.9^\circ,\end{aligned} \tag{7.3}$$

[1]This particular size of the observer was chosen as it corresponds to the spacing of a grid on which the magnetic field is defined. This way no more deflections should influence the particle trajectory. Smaller observer was not used also due to the high computational time.

$$\delta = \arcsin(\cos(b)\cos(27.1^\circ)\sin(l - 122.9) + \sin(b)\sin(27.1^\circ)), \tag{7.4}$$

where α is the right ascension and δ denotes the declination [62].

A Mollweide projection is used in this diploma thesis to plot the galactic coordinates. The Mollweide projection is a pseudocylindrical equal-area map projection that is frequently used to visualise objects in the sky. The projection is visualised on an ellipse with axes ratio 2:1. The $(\widehat{x}, \widehat{y})$ positions in the projection plane are numerically calculated from latitude b and longitude l using equations [64]

$$\widehat{x} = R\frac{2\sqrt{2}}{\pi} l \cos\theta, \tag{7.5}$$

$$\widehat{y} = R\sqrt{2}\sin\theta \tag{7.6}$$

and

$$2\theta + \sin 2\theta = \pi \sin b, \tag{7.7}$$

where R is the radius of the projected ellipse and θ is an auxiliary angle.

7.3 Results

Simulated data from direct simulations of protons, helium and nitrogen nuclei using JF12 and simulations of protons and helium nuclei in Pshirkov model of GMF contain $\sim 100,000$ particles hitting the observer for each element and each model. Harmonic analysis in right ascension α was applied to study large-scale anisotropies in the arrival directions of cosmic rays. Simulated data were fitted by the first harmonic

$$f(\alpha) = r_{\mathrm{dip}} \cos(\alpha + \varphi_{\mathrm{dip}}) + 1, \tag{7.8}$$

where r_{dip} is the amplitude of the dipole and φ_{dip} is the phase of the dipole. In [2], the Rayleigh analysis was used to analyse the first harmonic, while χ^2 minimalization of the simulated data by function (7.8) was applied in this diploma thesis. Both of these procedures lead to very similar results and are almost equivalent. Obtained data were also fitted by the second harmonic

$$f(\alpha) = r_{\mathrm{quad}} \cos(2\alpha + \varphi_{\mathrm{quad}}) + 1, \tag{7.9}$$

where r_{quad} is the amplitude of the quadrupole and φ_{quad} is the phase of the quadrupole and, finally, the simulated data were also compared with an isotropic distribution.

The arrival directions of simulated data for each element and their combinations are not compatible with an isotropic distribution. Values of χ^2/ndf describing consistency of simulated data with isotropic distribution are introduced in Table 7.1 for individual simulated elements and their combinations for both JF12 model and Pshirkov model of GMF. Amplitudes and phases of dipole and quadrupole anisotropies of the simulated data obtained from fitted distributions of arrival directions by equations (7.8) and (7.9) are also listed in Table 7.1 together with their χ^2/ndf values.

Simulated data propagated in the JF12 and Pshirkov model of GMF both indicate anisotropies in arrival directions, but the resulting form of the anisotropy differs. Except of pure nitrogen composition, all other combinations are best described by a quadrupole distribution of arrival directions in the right ascension using the JF12 model of GMF. Normalized rates of particles in the right ascension for individual simulated primaries and their combinations are depicted in Figures 7.1-7.3 and Figures B.1-B.5 in the Appendix B for the JF12 model of GMF. Together with the simulated data, the best fit and the visualisation of the dipole measured by the PAO are shown.

The best fit by the second harmonic (7.9) is found for combination of all three simulated elements with energies > 8 EeV resulting with $\chi^2/n = 8.888/10$, where n is the number of degrees of freedom equal to number of bins minus number of free parameters of the fit (see Figure 7.3). The amplitude of the quadrupole is $(1.5 \pm 0.3)\%$. Generally, the amplitude of the quadrupole goes from $(3.2 \pm 0.4)\%$ for the case of pure protons illustrated in Figure 7.1 down to the mentioned $(1.5 \pm 0.3)\%$ for combination of all three simulated primaries, except pure nitrogen composition. Two observed minima in the right ascension are around $\alpha_{\mathrm{min1}} \sim (50 \pm 20)^\circ$ and $\alpha_{\mathrm{min2}} \sim (230 \pm 20)^\circ$.

For simulations propagating nitrogen nuclei, the JF12 rather forms a dipole than quadrupole distribution of arrival directions as it can be seen in Figure 7.2. This might be caused by much lower rigidities of simulated particles than in the case of protons or helium nuclei at same energies. This results in the different behaviour since the trajectories are much more influenced by the magnetic field.

While an anisotropy was found in simulated data in the energy range $4\,\mathrm{EeV} < \mathrm{E} < 8\,\mathrm{EeV}$ using the JF12 model of GMF (see Figure B.2), measured data by the Pierre Auger Observatory in this energy range are consistent with isotropic arrival directions [2]. However, our simulations contain only extragalactic cosmic rays while the measured data by the PAO probably contain also a contribution of cosmic rays from Galactic sources and also can contain heavier elements such as iron nuclei that would smear the mentioned effect. Our simulations show that large-scale anisotropies can arise due to the propagation in magnetic fields even for less energetic particles. This is not surprising, since anisotropies were

found also in simulations of nitrogen nuclei and the major quantity influencing deflections in magnetic field is the rigidity of the particle rather than its kinetic energy alone.

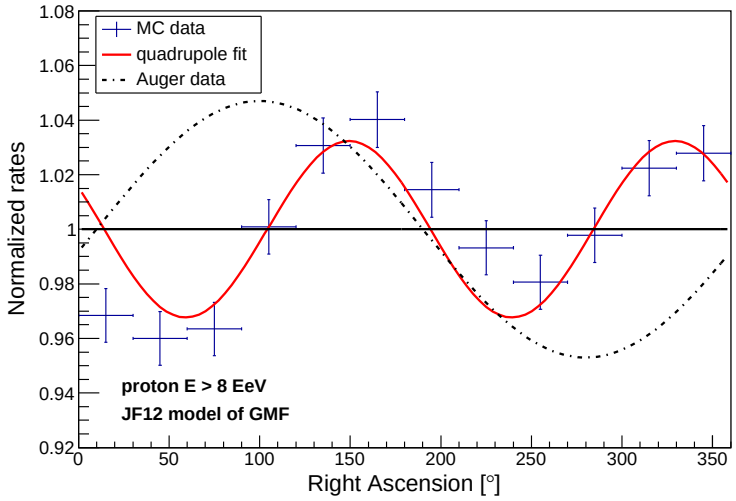

Figure 7.1: Normalized rate of protons with $E > 8$ EeV hitting the observer as a function of the right ascension. Red line corresponds to the best fit by function (7.9) from Table 7.1. JF12 model of GMF was used. Dashed line corresponds to the anisotropy measured by the PAO [2].

The Pshirkov model of GMF predicts a different behaviour of arrival directions originating from isotropic flux of extragalactic UHECR to the Galaxy than the JF12 model. Results of the individual fits of the data by equations (7.8) and (7.9) are listed in Table 7.1 together with the consistency of simulated data with isotropic distribution of arrival directions. In case of the Pshirkov model, large-scale anisotropies in the form of a dipole are created rather than the quadrupole behaviour of arrival directions. This is nicely demonstrated in the case of arrival directions in the right ascension of simulated helium nuclei in Figure 7.4. Distribution of arrival directions in this case resembles the measured anisotropy by the PAO shifted in phase of the dipole by $\sim 70°$. On the other hand, in the case of simulated protons the best consistency is also found for the dipole anisotropy but compatibility of the simulated data with the quadrupole anisotropy or even with the isotropic distribution can not be excluded as well ($\chi^2/n = 21.5/12$ for the isotropic distribution, $\chi^2/n = 13.6/10$ for the dipole modulation and $\chi^2/n = 14.8/10$ for the quadrupole behaviour).

The original positions where particles enter the Galaxy are visualised in Figure 7.5 in galactic coordinates for simulations in JF12 model of GMF for

primaries	Energy [EeV]	number of particles	χ^2/ndf (isotropy)	r_{dip}[%]	φ_{dip}[°]	χ^2/ndf (dipole)	r_{quad}[%]	φ_{quad}[°]	χ^2/ndf (quadrupole)
p	> 4	118,852	5.967	1.7 ± 0.4	60 ± 10	5.542	2.6 ± 0.4	80 ± 10	3.328
p	> 8	120,589	7.035	1.7 ± 0.4	20 ± 10	6.758	3.2 ± 0.4	62 ± 7	2.183
He	> 8	102,045	4.668	1.1 ± 0.4	60 ± 20	5.020	2.8 ± 0.4	85 ± 9	2.014
N	> 8	97,886	2.884	2.3 ± 0.4	10 ± 10	1.019	0.3 ± 0.5	58 ± 8	3.462
p+He	> 8	222,634	8.431	0.6 ± 0.3	10 ± 30	9.725	2.8 ± 0.3	75 ± 6	1.161
p+N	> 8	218,475	3.945	0.5 ± 0.3	70 ± 30	4.406	1.9 ± 0.3	64 ± 9	0.943
He+N	> 8	199,931	4.415	1.4 ± 0.3	10 ± 10	3.314	1.5 ± 0.3	80 ± 10	3.119
p+He+N	> 8	320,520	6.284	0.3 ± 0.3	10 ± 50	7.370	2.0 ± 0.3	77 ± 7	0.889
p (Psh)	> 8	114,490	1.792	1.2 ± 0.4	40 ± 20	1.360	1.1 ± 0.4	20 ± 20	1.481
He (Psh)	> 8	119,541	8.109	3.6 ± 0.4	30 ± 7	2.132	1.3 ± 0.4	80 ± 20	8.849
p+He (Psh)	> 8	234,031	5.975	2.1 ± 0.3	16 ± 8	1.918	0.9 ± 0.3	60 ± 20	6.169

Table 7.1: Results of the harmonic analysis in the right ascension of simulated data of protons, helium and nitrogen nuclei and their combinations in given energy ranges. Most of the values are for simulations in JF12 model of GMF, when (Psh) stated the Pshirkov 2011 model of GMF was used in the simulation. Values of χ^2/ndf of the simulated data when compared with isotropic distribution and dipole and quadrupole anisotropies in right ascension are listed in this table. r_{dip} is the amplitude and φ_{dip} is the phase of fitted sinusoidal function (7.8). Amplitude and phase of the quadrupole, r_{quad} and φ_{quad}, come from fits by a second harmonic (7.9).

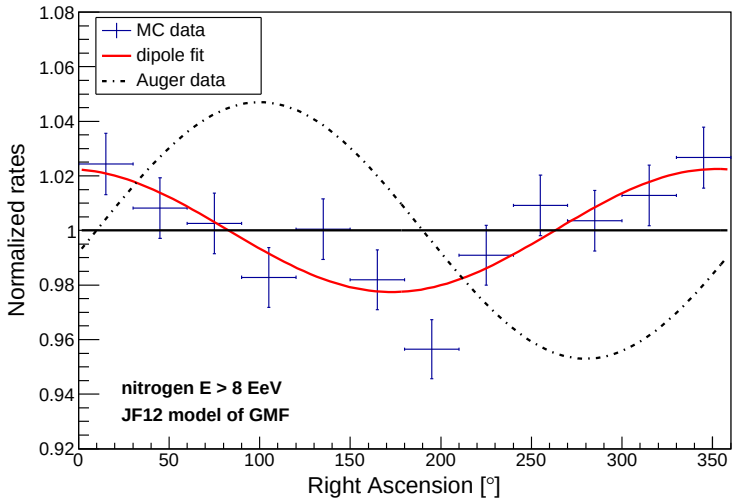

Figure 7.2: Normalized rate of nitrogen nuclei with $E > 8$ EeV hitting the observer as a function of the right ascension. Red line corresponds to the best fit by function (7.8) from Table 7.1. JF12 model of GMF was used. Dashed line corresponds to the anisotropy measured by the PAO [2].

particles reaching the observer. A clear shadowing by the centre of the Galaxy is demonstrated that has a consequence that a large amount of extragalactic sources are invisible to the observer on Earth. This result is consistent with previous simulations using JF12 model of GMF [61]. The shadowing effect seems to be more significant for heavier primary particles of the same energy. In other words, it depends on the rigidity of the particle. Positions of particles on the galactic border separately for simulated protons and nitrogen nuclei reaching the observer are visualised in Figure 7.6. The same tendency of shadowing by the galactic centre can be found in simulations using the Pshirkov model of GMF depicted in Figure 7.7. In the case of Pshirkov model of GMF particles arriving to the defined observer originally come from extragalactic sources with positions at the entrance to the Galaxy located predominantly in the galactic plane. On the contrary, JF12 allows arrival to Earth to particles even from larger latitudes, but with a preferred origin in the northern "hemisphere" of extragalactic space.

Simulated data contain arrival directions of particles to the observer of a radius of 100 pc. For more precise predictions of distribution of arrival directions on the Earth, more extensive simulations would have to be performed. However, if anisotropies arose from originally isotropic flux on the observer with radius 100 pc, anisotropies should be observed also for a smaller observer in the first approximation.

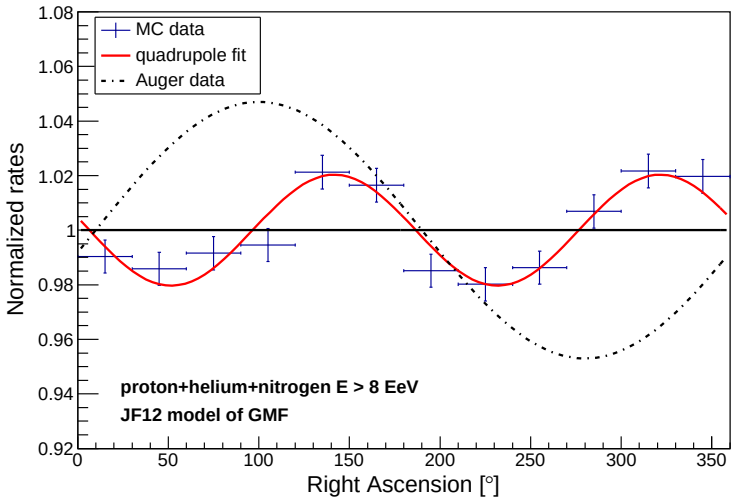

Figure 7.3: Normalized rate of particles with $E > 8$ EeV hitting the observer as a function of the right ascension. Combination of simulated protons and helium and nitrogen nuclei propagated in JF12 model of GMF is used. Red line corresponds to the best fit by function (7.9) from Table 7.1. Dashed line corresponds to the anisotropy measured by the PAO [2].

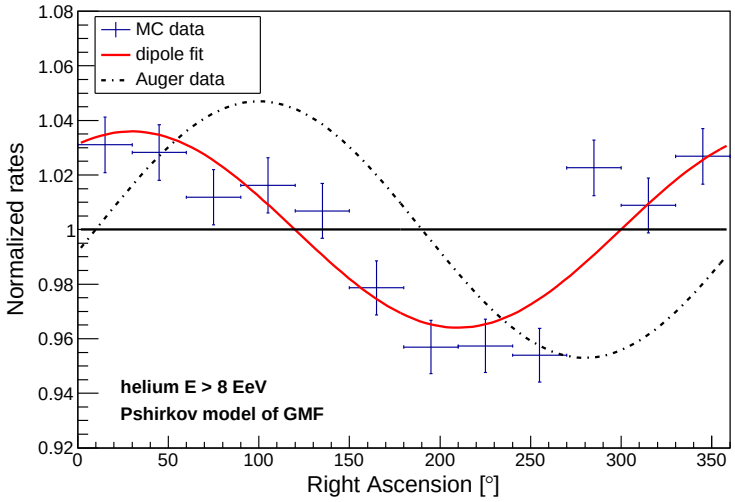

Figure 7.4: Normalized rate of helium nuclei with $E > 8$ EeV hitting the observer as a function of right ascension. Red line corresponds to the best fit by function (7.8) and the parameters of the fit are listed in Table 7.1. Dashed line corresponds to the anisotropy measured by the POA [2]. JF12 model of GMF was used.

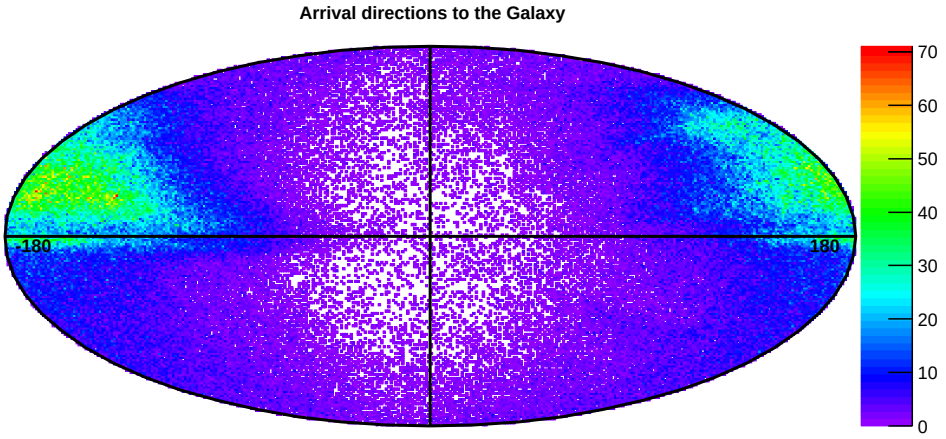

Figure 7.5: Original positions of particles hitting the observer when they enter the Galaxy in galactic coordinates. Colour scheme represents number of particles at given positions. Simulations of propagation of protons, helium and nitrogen nuclei in the JF12 model of GMF are used.

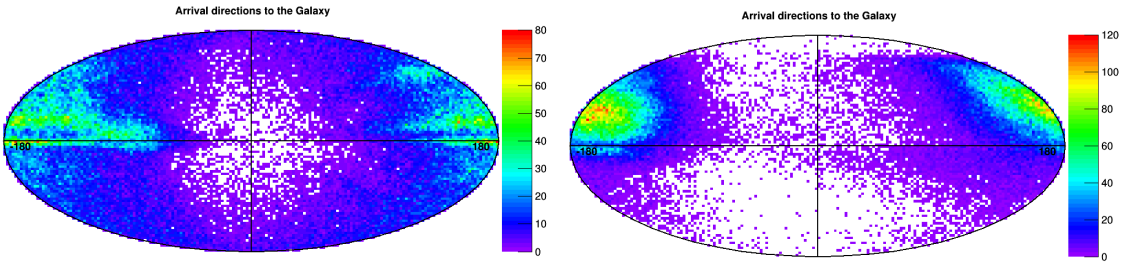

Figure 7.6: Comparison of original positions on the galactic border of protons (left) and nitrogen nuclei (right) hitting the observer simulated with the JF12 model of GMF. Colour scheme represents number of particles at given positions.

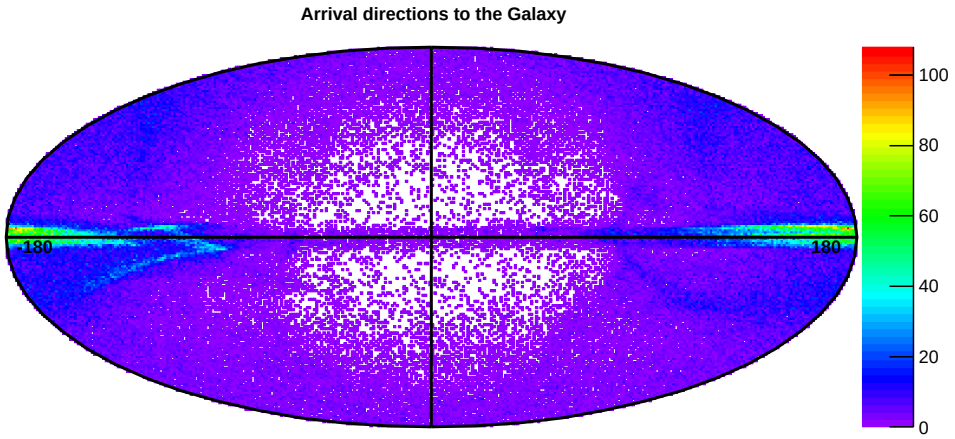

Figure 7.7: Original positions of particles hitting the observer when they enter the Galaxy in galactic coordinates. Colour scheme represents number of particles at given positions. Simulations propagating protons and helium nuclei in the Pshirkov model of GMF are used.

Chapter 8

Conclusions

This thesis was dedicated to predictions of observable aspects of extragalactic cosmic rays coming to Earth. Simulations of cosmic-ray propagation were performed in CRPropa 3 using one-dimensional mode of particle propagation and three-dimensional mode of propagation including the effects of Galactic magnetic fields. Two main phenomena were investigated including the shape of the energy spectrum of cosmic rays observed at the highest energies and large-scale anisotropies of arrival directions of ultra-high energy cosmic rays induced due to their propagation in Galactic magnetic field.

We performed simulations of cosmic rays from single sources in one-dimensional mode of CRPropa 3, and investigated the properties of the source required to form an energy spectrum compatible with the measured data of the Pierre Auger Observatory. Energy range from $10^{19.5}$ eV up to $10^{20.2}$ eV was investigated. Included properties of the source were the spectral index of injected particles, mass composition of injected particles, maximal rigidity and distance of the source. Simulated energy spectra on Earth were compared with the energy spectrum measured by the Pierre Auger Observatory.

No obvious restrictions were found concerning the distance of the source. However, most of the solutions come from sources not farther than 50 Mpc, and the number of possible solutions considerably decreases with a further increasing distance. Still, some solutions originating even from a source distant 100 Mpc appeared. The decrease of the number of solutions with distance of the source is caused by energy losses that particles undergo in the Universe. High spectral indices $\gamma \geq 3$ can describe the measured data well in the whole range of investigated rigidity cutoffs. This is probably caused by the closeness of the simulated spectral index and the spectral index of measured data $\gamma \sim 4.8$. Other spectral indices $\gamma = (-1.0, 2.5)$ can describe the measured data well for a limited range of the maximal source rigidity, mostly around $\log(R_{\mathrm{cut}}/\mathrm{V}) \sim 18.9 - 19.8$.

The energy evolution of the mean $\ln \mathrm{A}$ on Earth strongly depends on the

composition of particles emitted by the source. Generally, a small fraction of iron nuclei emitted by the source results in an increase of the mean $\ln A$ on Earth with energy. This statement is also independent on the source distance. Sources emitting particles without the iron nuclei habitually generate smaller mean $\ln A$ on Earth with rather decreasing or flat energy evolution of the mean $\ln A$. This result is very promising since it could lead to estimations of the particle composition at their sources in the future when higher event statistics and more data about the mass composition of cosmic rays at the highest energies are available.

Following the recent finding of large-scale anisotropies of arrival directions of cosmic rays above 8 EeV by the Pierre Auger Observatory, simulations of particle propagation in Galactic magnetic fields were performed in the three-dimensional mode of CRPropa 3. Two models of galactic magnetic fields were used - Jansson-Farrar 2012 model and Pshirkov 2011 model of Galactic magnetic field. We simulated an isotropic flux of extragalactic cosmic rays entering the Galaxy with energies above 8 EeV. Protons and helium and nitrogen nuclei were propagated in the Galactic magnetic field and detected if they reached the observer of radius 100 pc placed at the coordinates (-8.5,0,0) kpc. Consistently with previous simulations of particle propagation in Jansson-Farrar 2012 model of Galactic magnetic field a "shadowing" of a large amount of extragalactic sources by the galactic centre was found. Therefore, most of the extragalactic cosmic rays reaching Earth come from sources located in the closer part of extragalactic space rather than from behind the galactic centre.

The simulated data in both models of Galactic magnetic fields are not consistent with isotropic distribution of arrival directions in most of the studied cases. An anisotropy of arrival directions in the form of a quadrupole occurred in most of the simulated data with the Jansson-Farrar 2012 model of Galactic magnetic field. The two observed minima in the right ascension are located at $\alpha \sim (50 \pm 20)^\circ$ and $\alpha \sim (230 \pm 20)^\circ$ with the amplitude of the quadrupole from $(3.2 \pm 0.3)\%$ down to $(1.5 \pm 0.3)\%$, depending on the type of simulated primary particles. On the contrary, particles simulated with the Pshirkov model of Galactic magnetic field form rather a dipole than a quadrupole in the distribution of arrival directions on the observer. The dipole measured by the PAO cannot be a consequence of Galactic magnetic field according to our current simulations. However, helium nuclei propagated with the Pshirkov model of GMF indicate a large-scale anisotropy in arrival directions of extragalactic cosmic rays in the form of a dipole with a similar amplitude, but with a phase shifted by $\sim 70^\circ$ when compared to the measured data.

Appendices

Appendix A

The Very End of the Energy Spectrum

Section 6.3 was dedicated to the results concerning possible features of sources of extragalactic cosmic rays that could produce the very end of energy spectrum consistent with the measured data. Resulting plots for some maximal rigidities were presented in Section 6.3. Figures containing informations about all the passed solutions for multiple values of R_{cut} that were not demonstrated in Section 6.3 are presented here. Figures A.1-A.20 and A.21-A.29 show all the possible solutions for given R_{cut} of spectral indices in the range (1.0 - 3.0) and (-1.0 - 0.5), respectively.

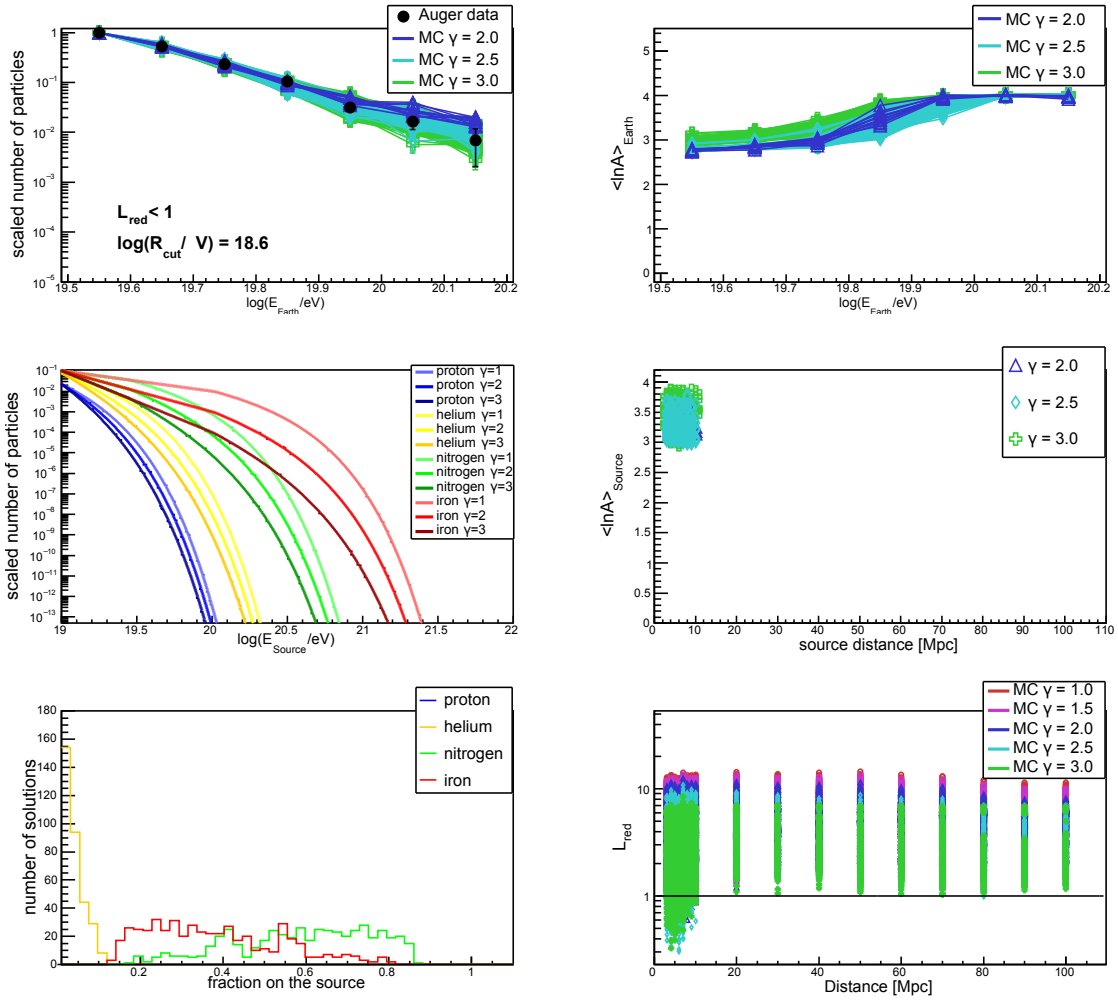

Figure A.1: Properties of simulated energy spectra for rigidity cutoff $\log(R_{\mathrm{cut}}/\mathrm{V}) = 18.6$. For description see caption of Figure 6.11.

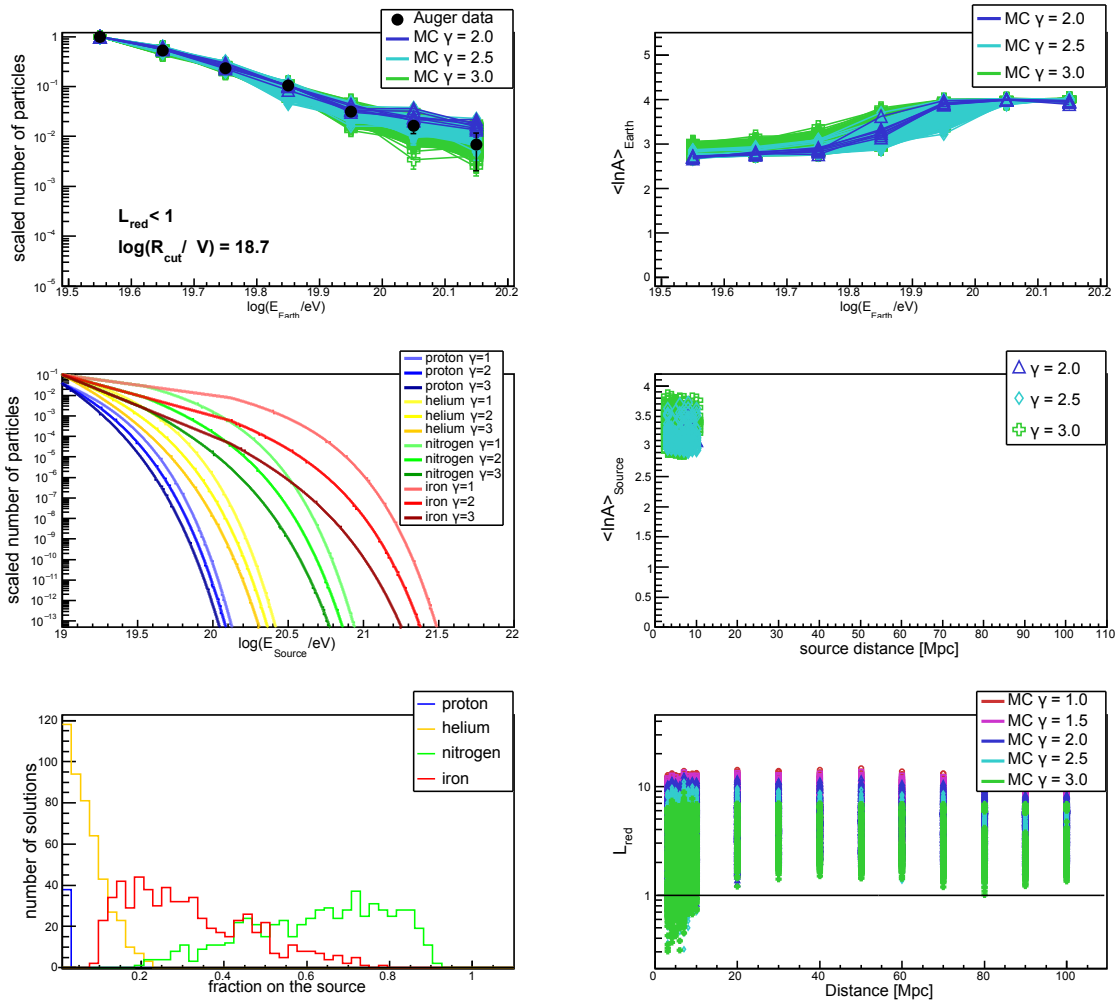

Figure A.2: Properties of simulated energy spectra for rigidity cutoff $\log(R_{\mathrm{cut}}/\mathrm{V}) = 18.7$. For description see caption of Figure 6.11.

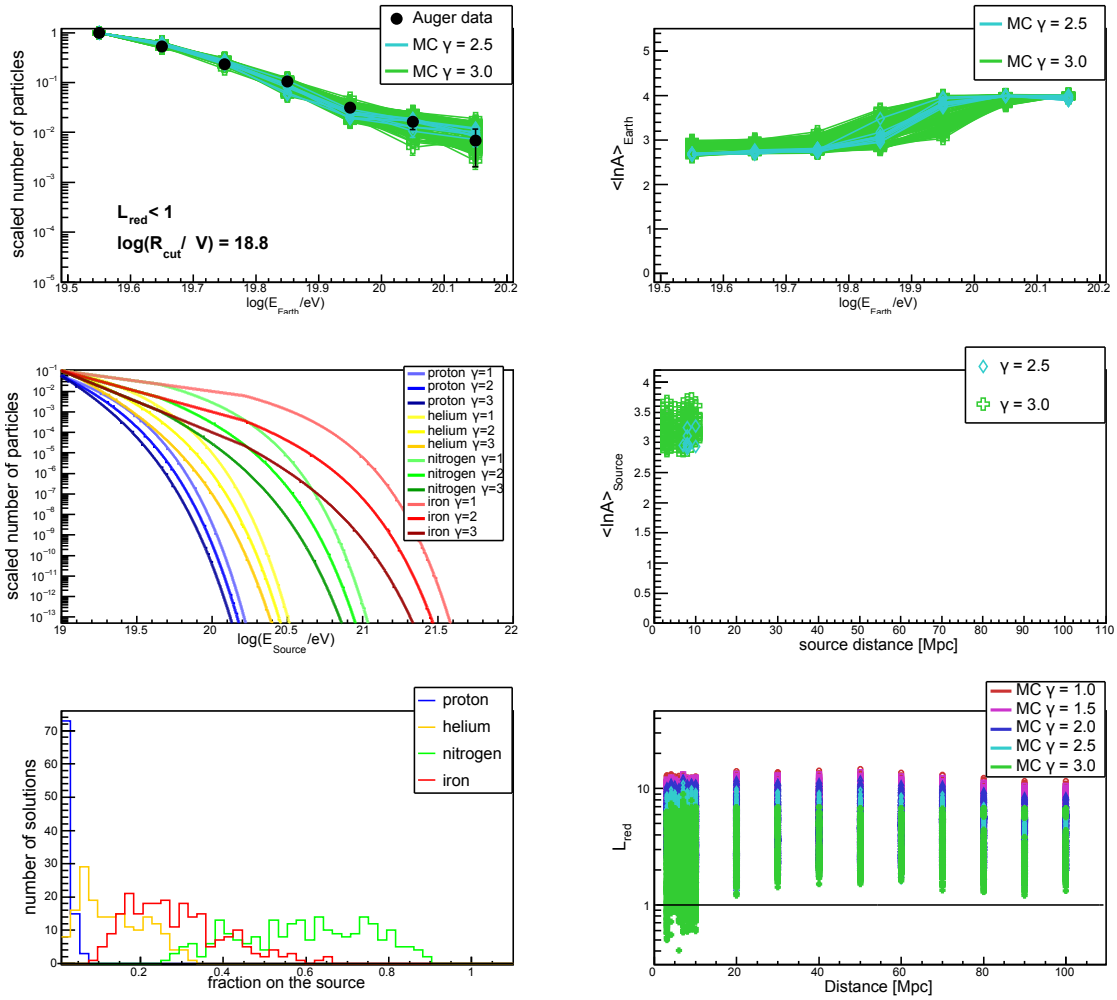

Figure A.3: Properties of simulated energy spectra for rigidity cutoff $\log(R_{\mathrm{cut}}/\mathrm{V}) = 18.8$. For description see caption of Figure 6.11.

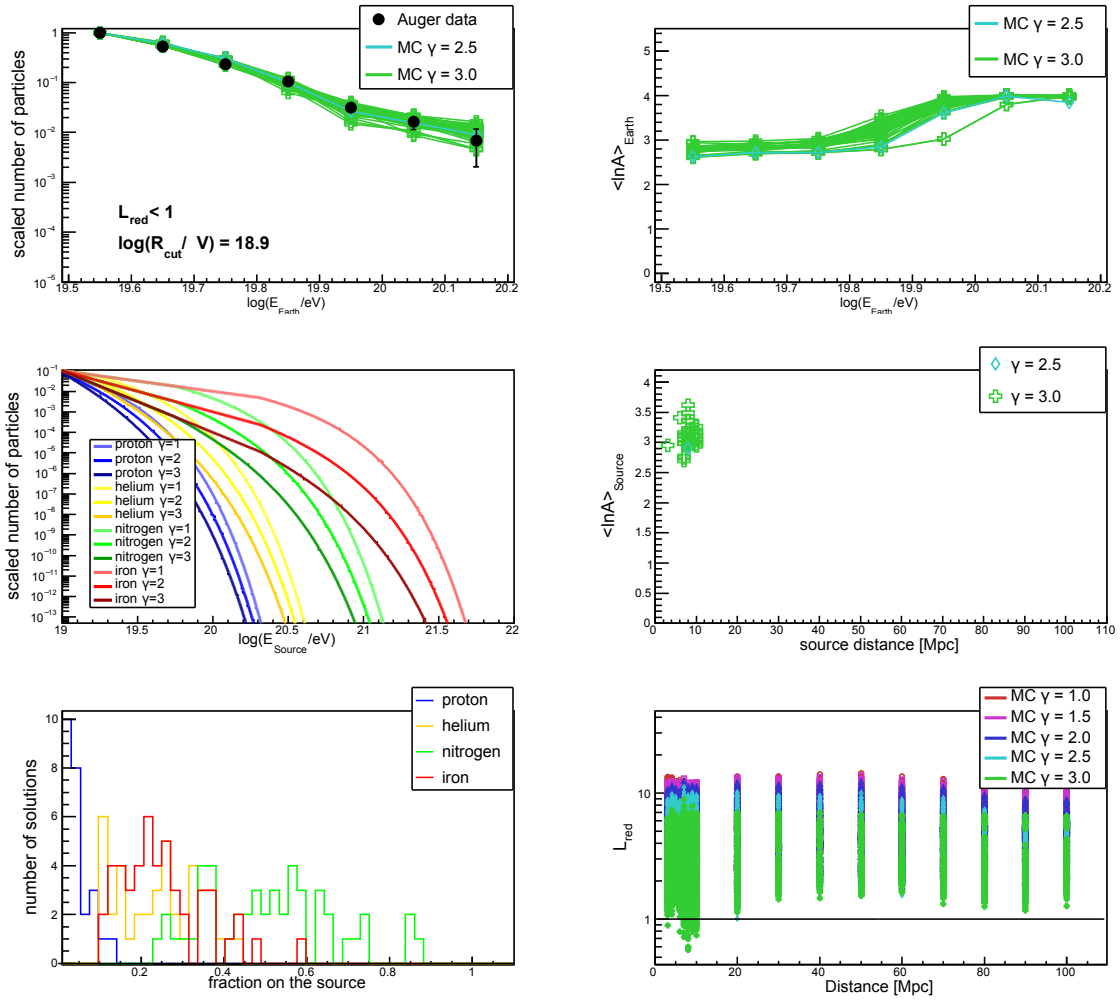

Figure A.4: Properties of simulated energy spectra for rigidity cutoff $\log(R_{\mathrm{cut}}/\mathrm{V}) = 18.9$. For description see caption of Figure 6.11.

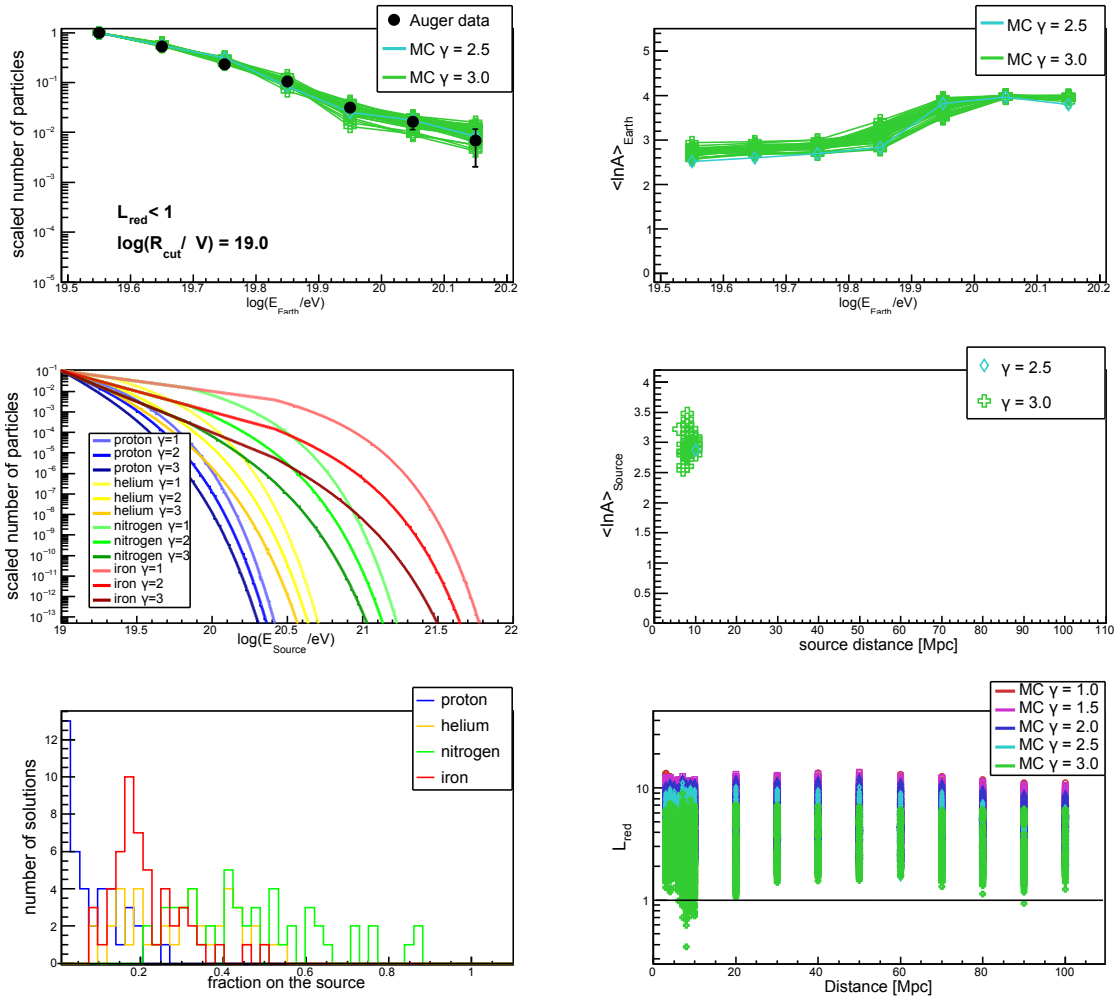

Figure A.5: Properties of simulated energy spectra for rigidity cutoff $\log(R_{\rm cut}/{\rm V}) = 19.0$. For description see caption of Figure 6.11.

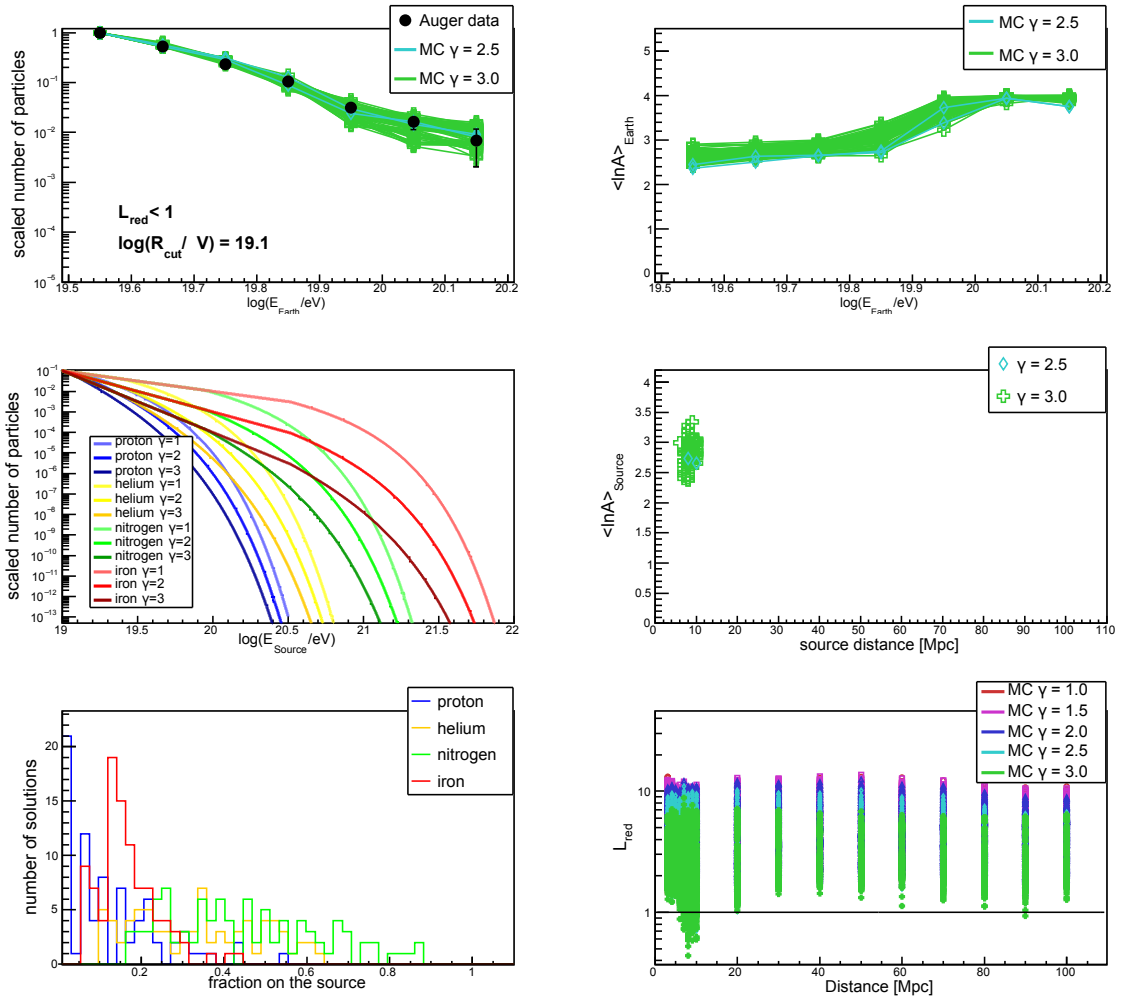

Figure A.6: Properties of simulated energy spectra for rigidity cutoff $\log(R_{\mathrm{cut}}/\mathrm{V}) = 19.1$. For description see caption of Figure 6.11.

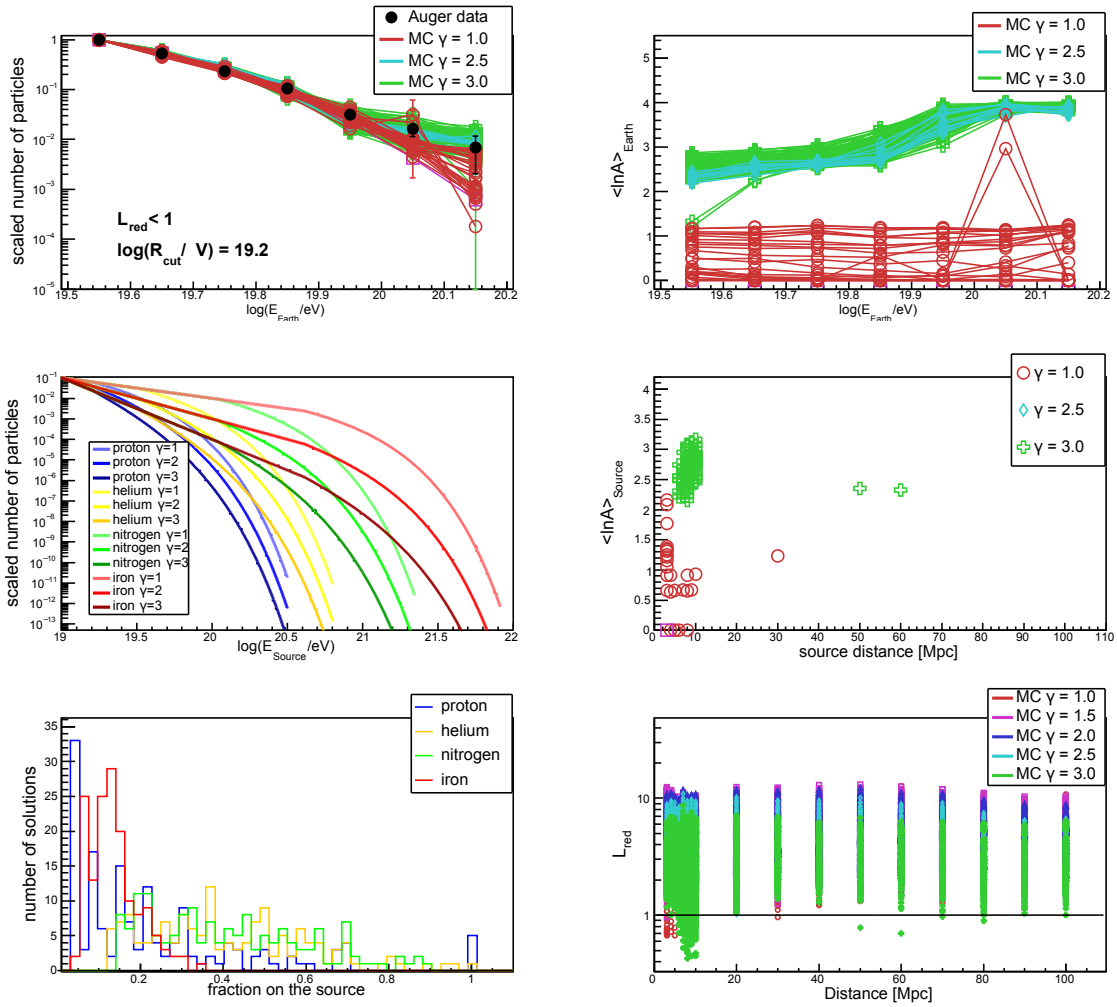

Figure A.7: Properties of simulated energy spectra for rigidity cutoff $\log(R_{\rm cut}/{\rm V}) = 19.2$. For description see caption of Figure 6.11.

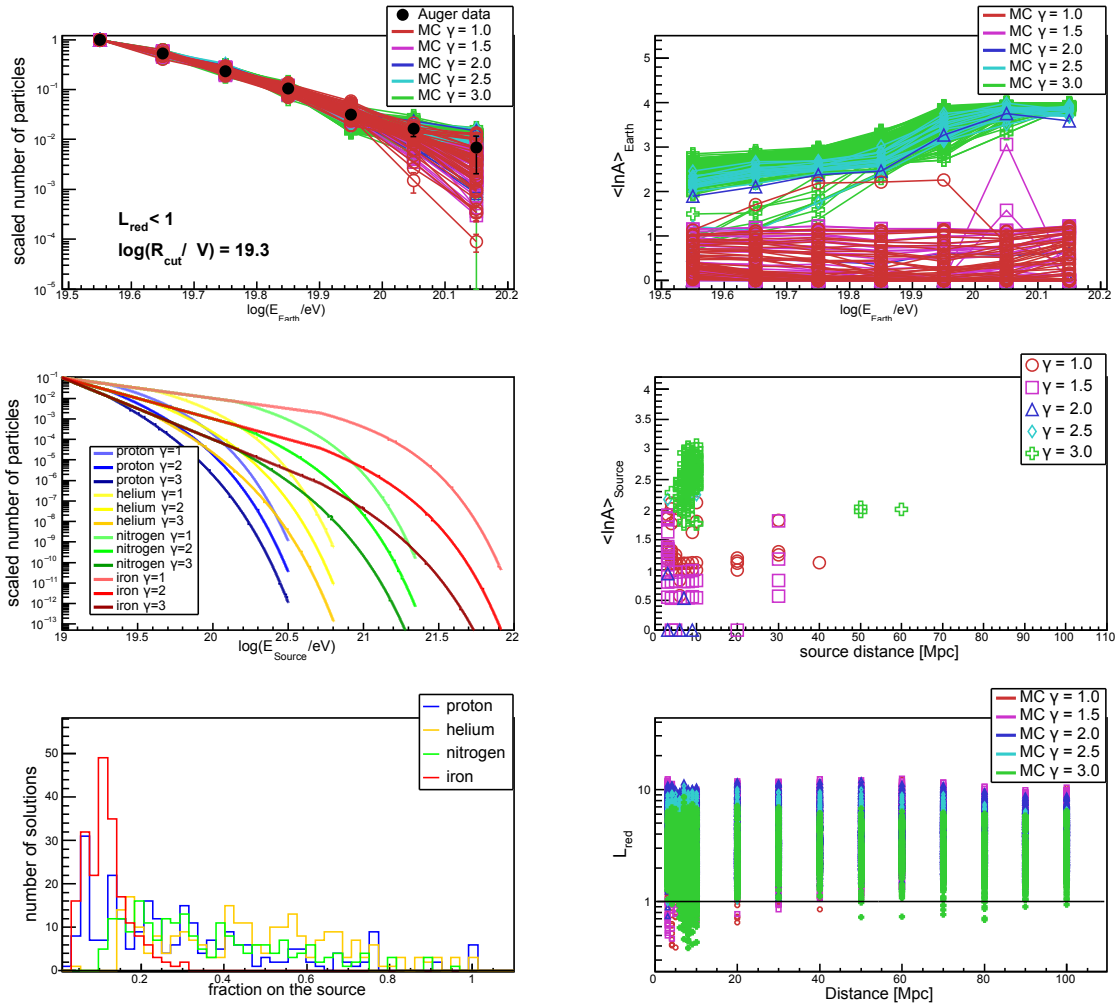

Figure A.8: Properties of simulated energy spectra for rigidity cutoff $\log(R_{\mathrm{cut}}/\mathrm{V}) = 19.3$. For description see caption of Figure 6.11.

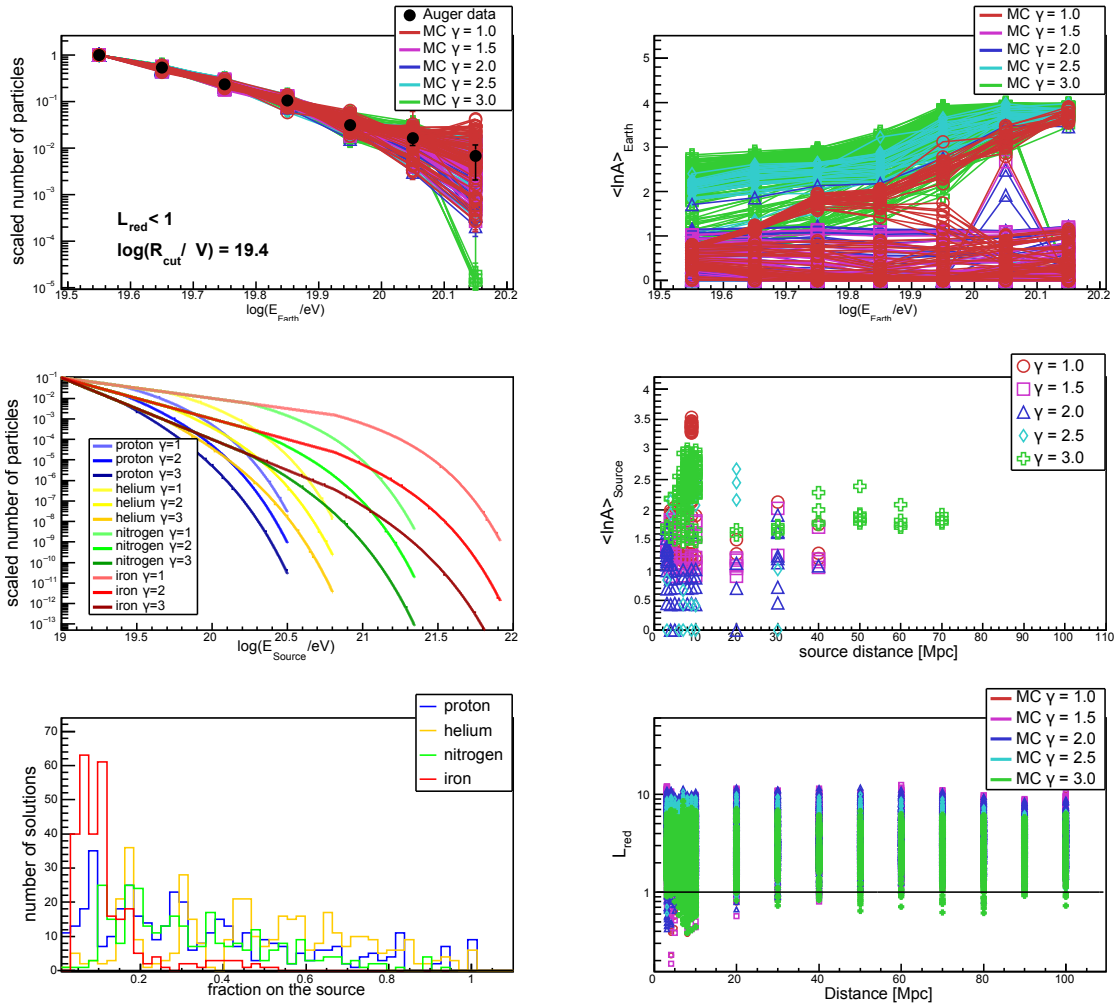

Figure A.9: Properties of simulated energy spectra for rigidity cutoff $\log(R_{\rm cut}/{\rm V}) = 19.4$. For description see caption of Figure 6.11.

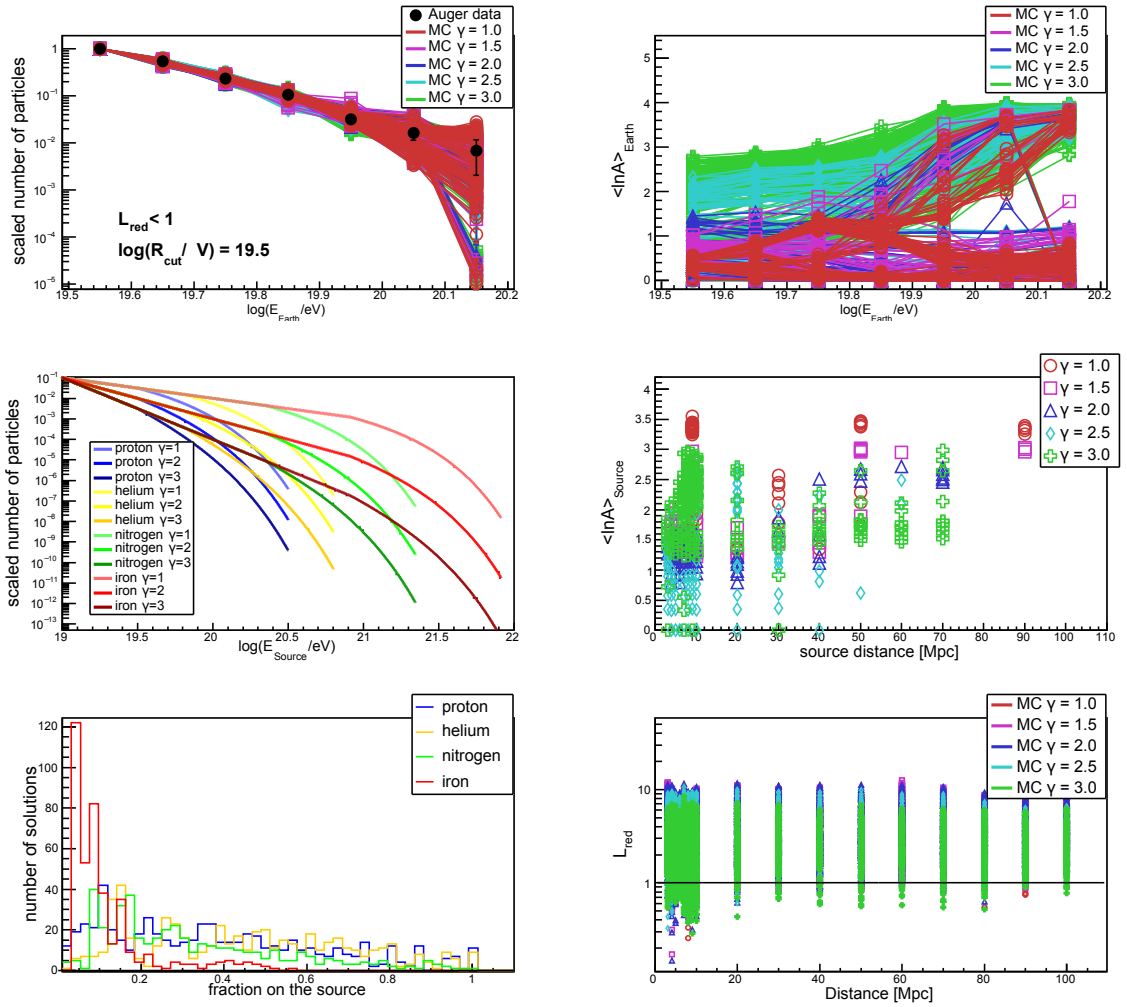

Figure A.10: Properties of simulated energy spectra for rigidity cutoff $\log(R_{\rm cut}/{\rm V}) = 19.5$. For description see caption of Figure 6.11.

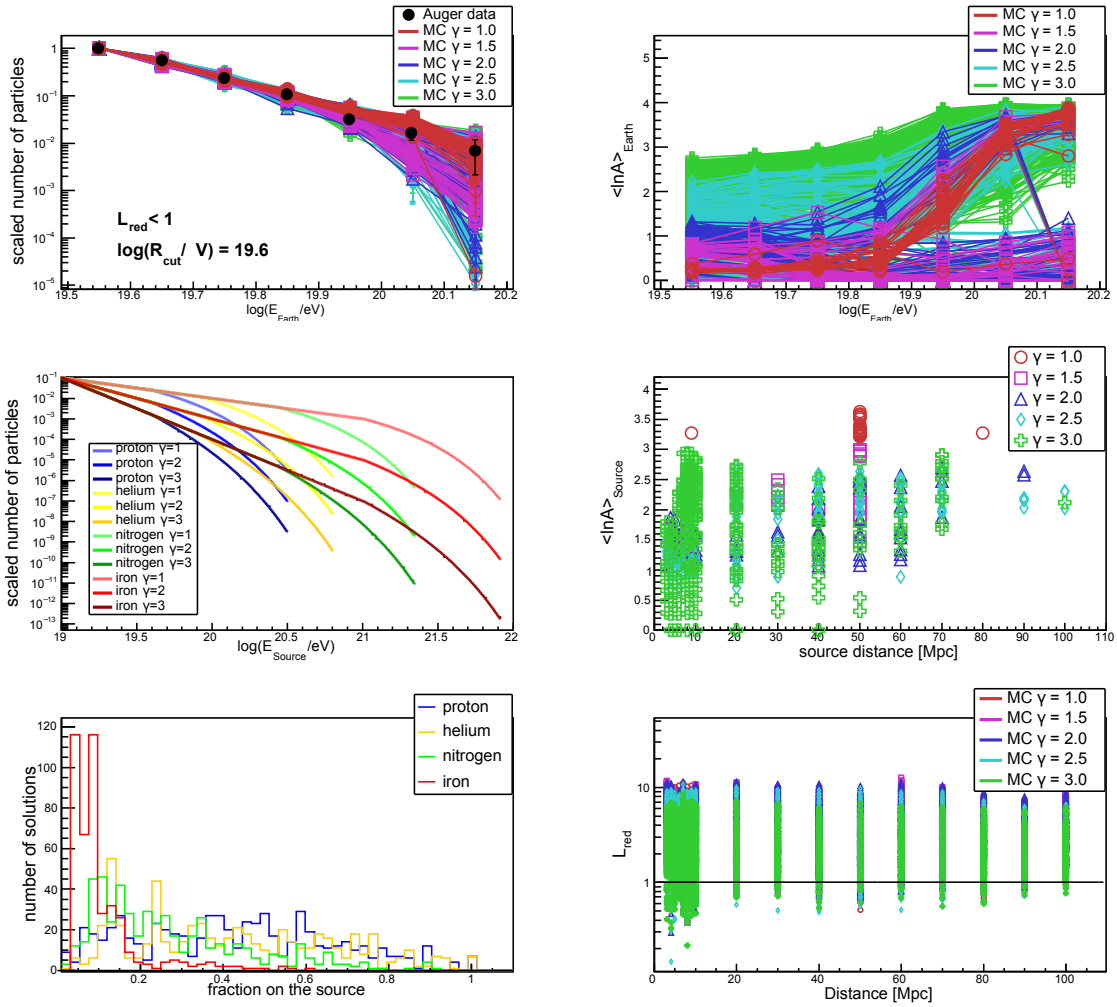

Figure A.11: Properties of simulated energy spectra for rigidity cutoff $\log(R_{\rm cut}/{\rm V}) = 19.6$. For description see caption of Figure 6.11.

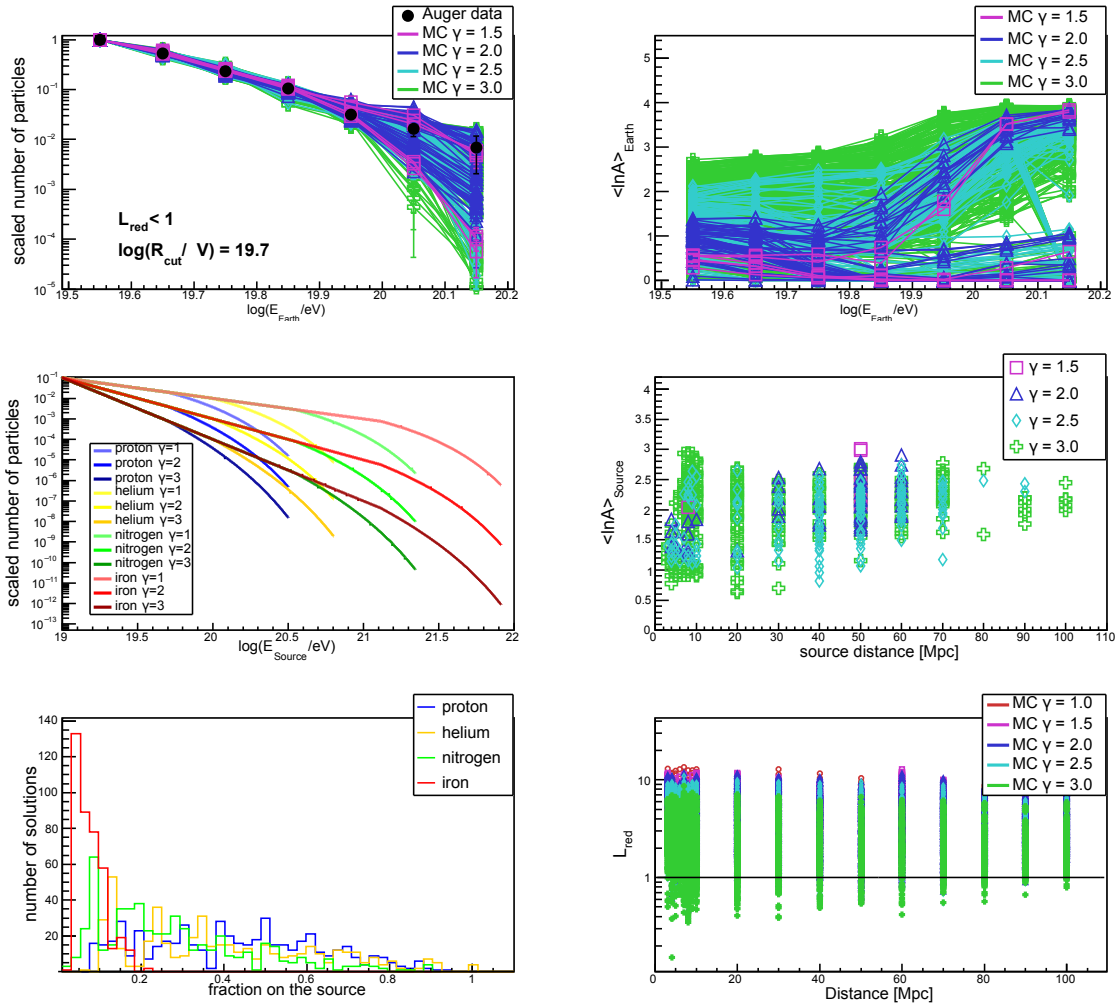

Figure A.12: Properties of simulated energy spectra for rigidity cutoff $\log(R_{\mathrm{cut}}/\mathrm{V}) = 19.7$. For description see caption of Figure 6.11.

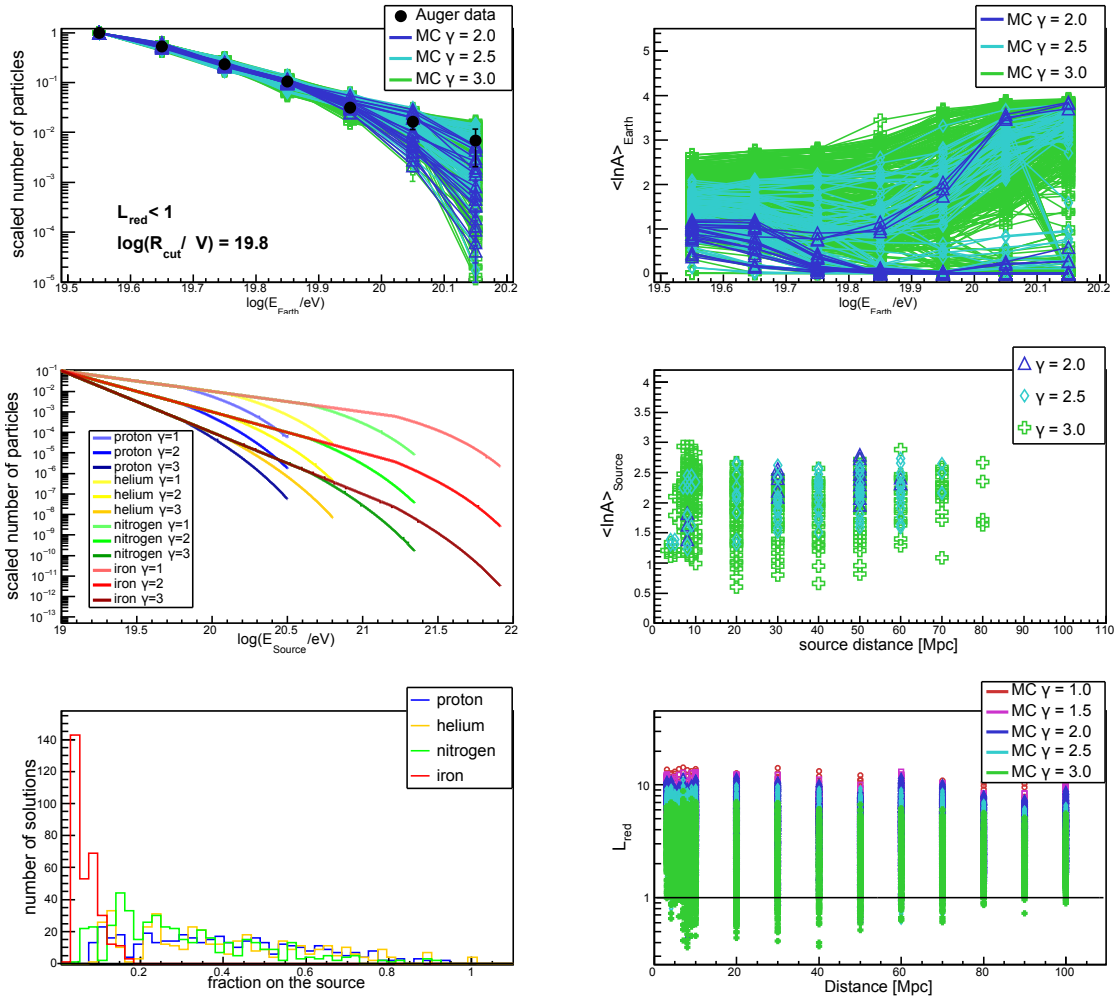

Figure A.13: Properties of simulated energy spectra for rigidity cutoff $\log(R_{\rm cut}/{\rm V}) = 19.8$. For description see caption of Figure 6.11.

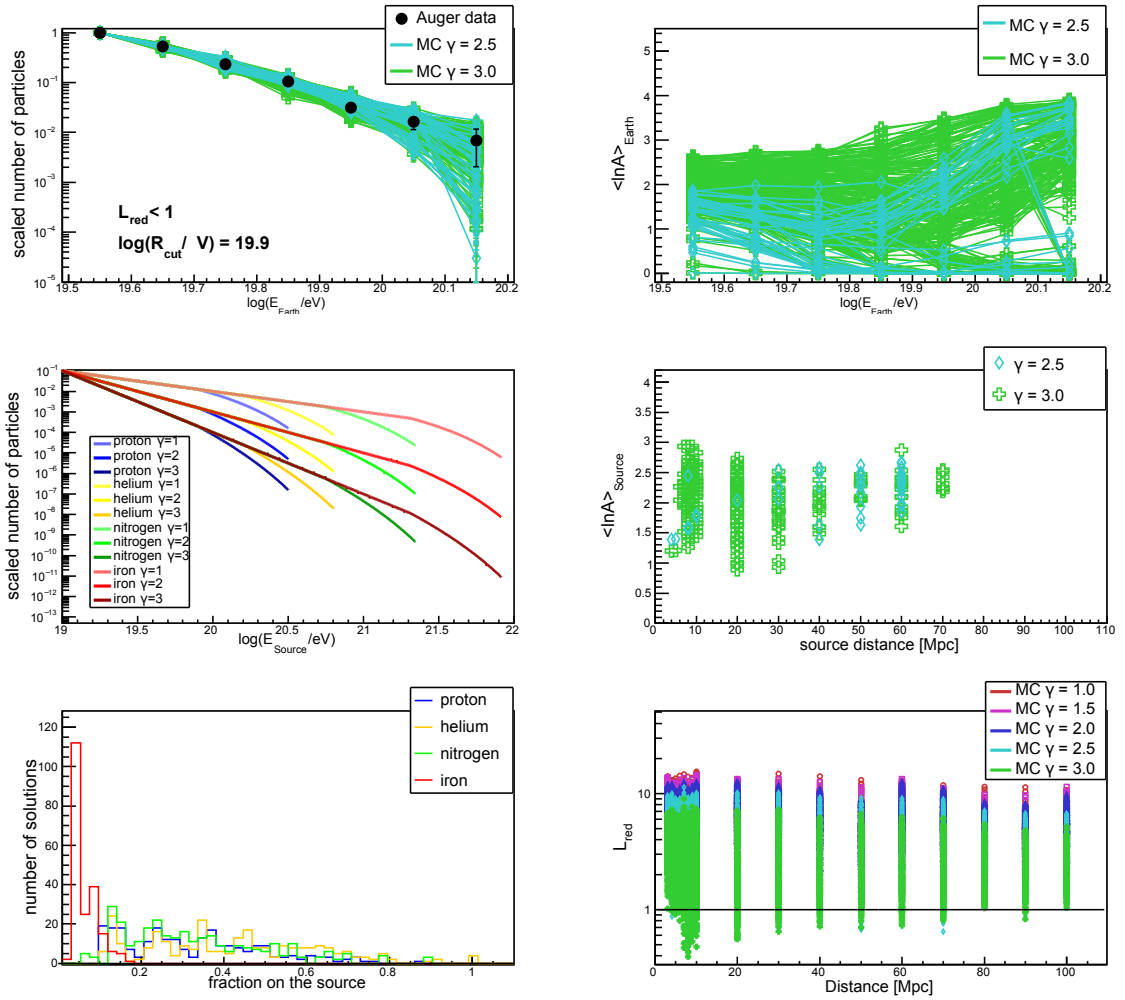

Figure A.14: Properties of simulated energy spectra for rigidity cutoff $\log(R_{\mathrm{cut}}/\mathrm{V}) = 19.9$. For description see caption of Figure 6.11.

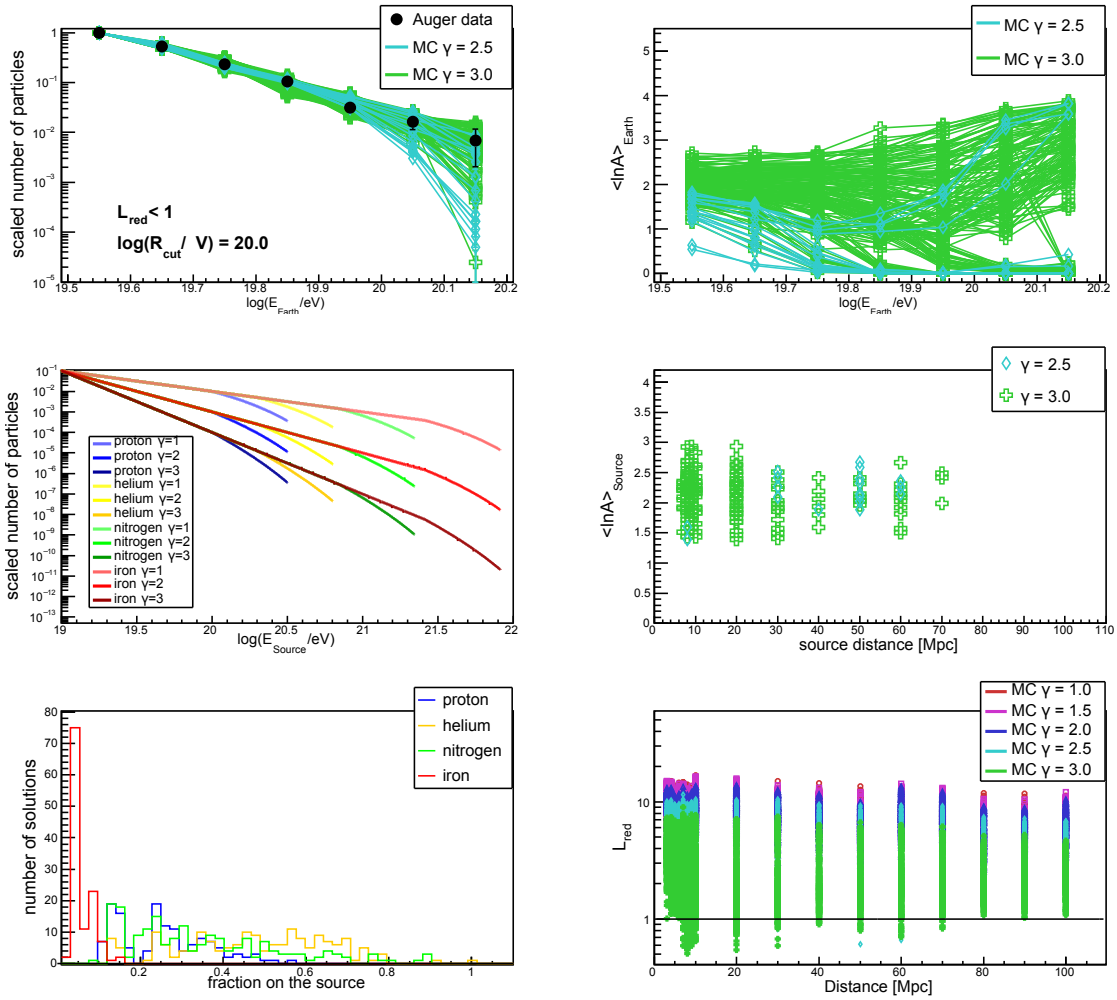

Figure A.15: Properties of simulated energy spectra for rigidity cutoff $\log(R_{\rm cut}/{\rm V}) = 20.0$. For description see caption of Figure 6.11.

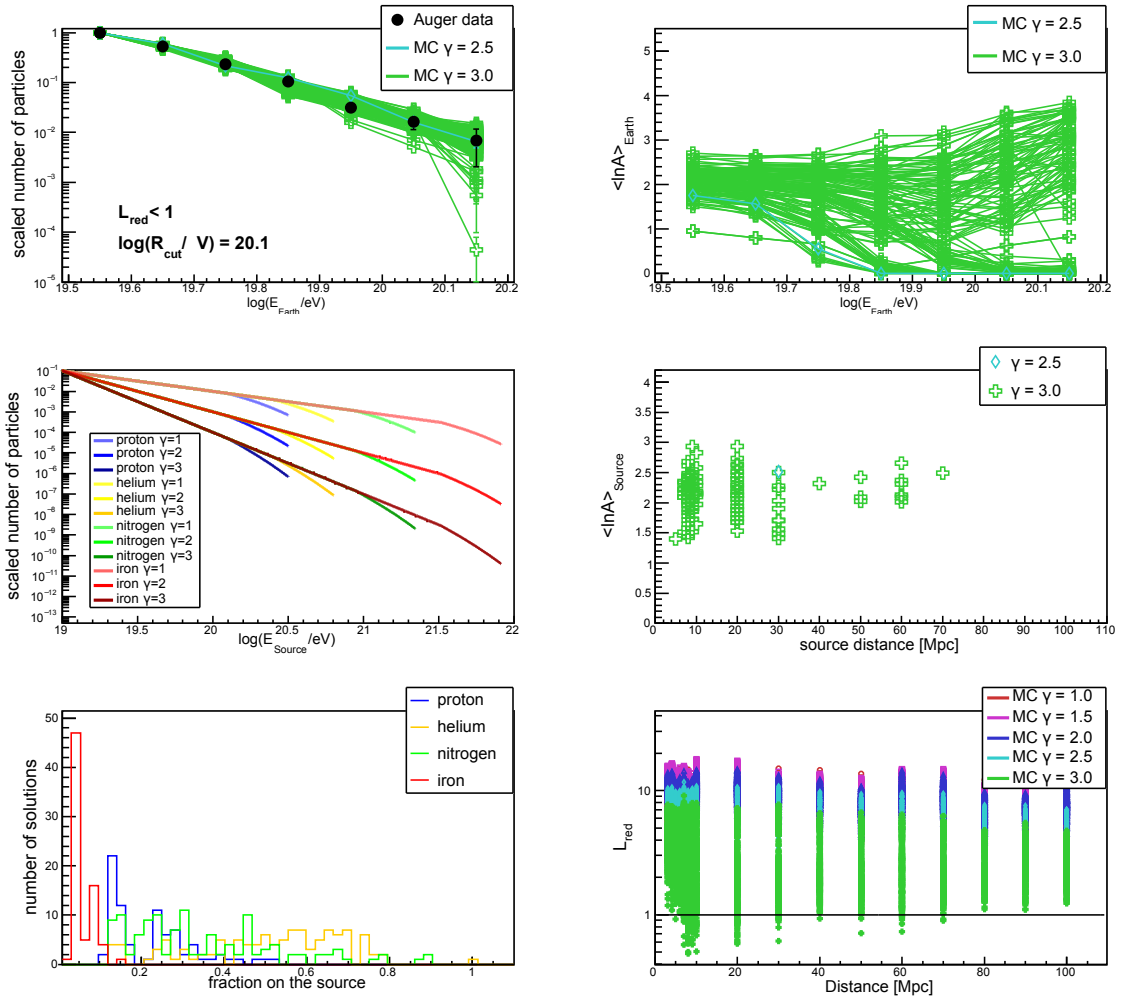

Figure A.16: Properties of simulated energy spectra for rigidity cutoff $\log(R_{\mathrm{cut}}/\mathrm{V}) = 20.1$. For description see caption of Figure 6.11.

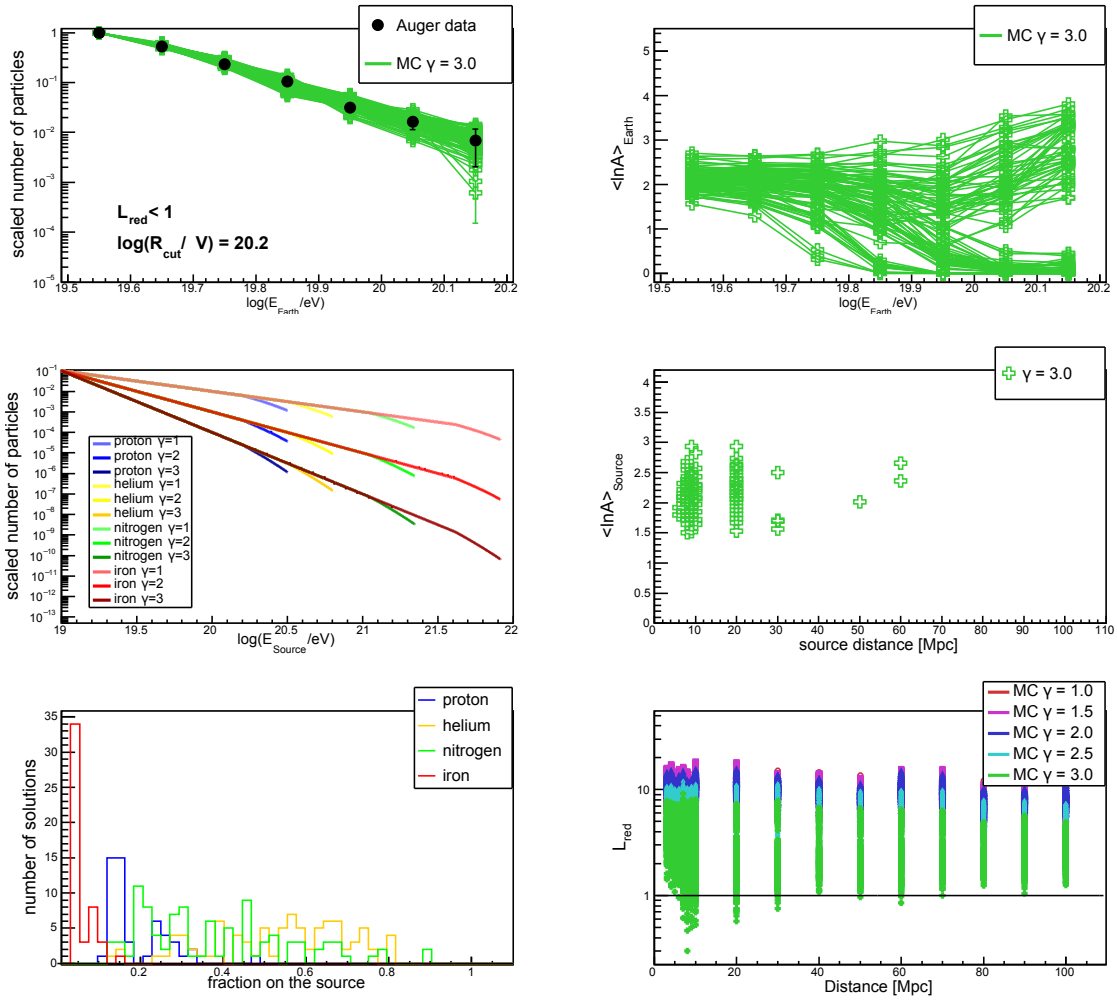

Figure A.17: Properties of simulated energy spectra for rigidity cutoff $\log(R_{\rm cut}/{\rm V}) = 20.2$. For description see caption of Figure 6.11.

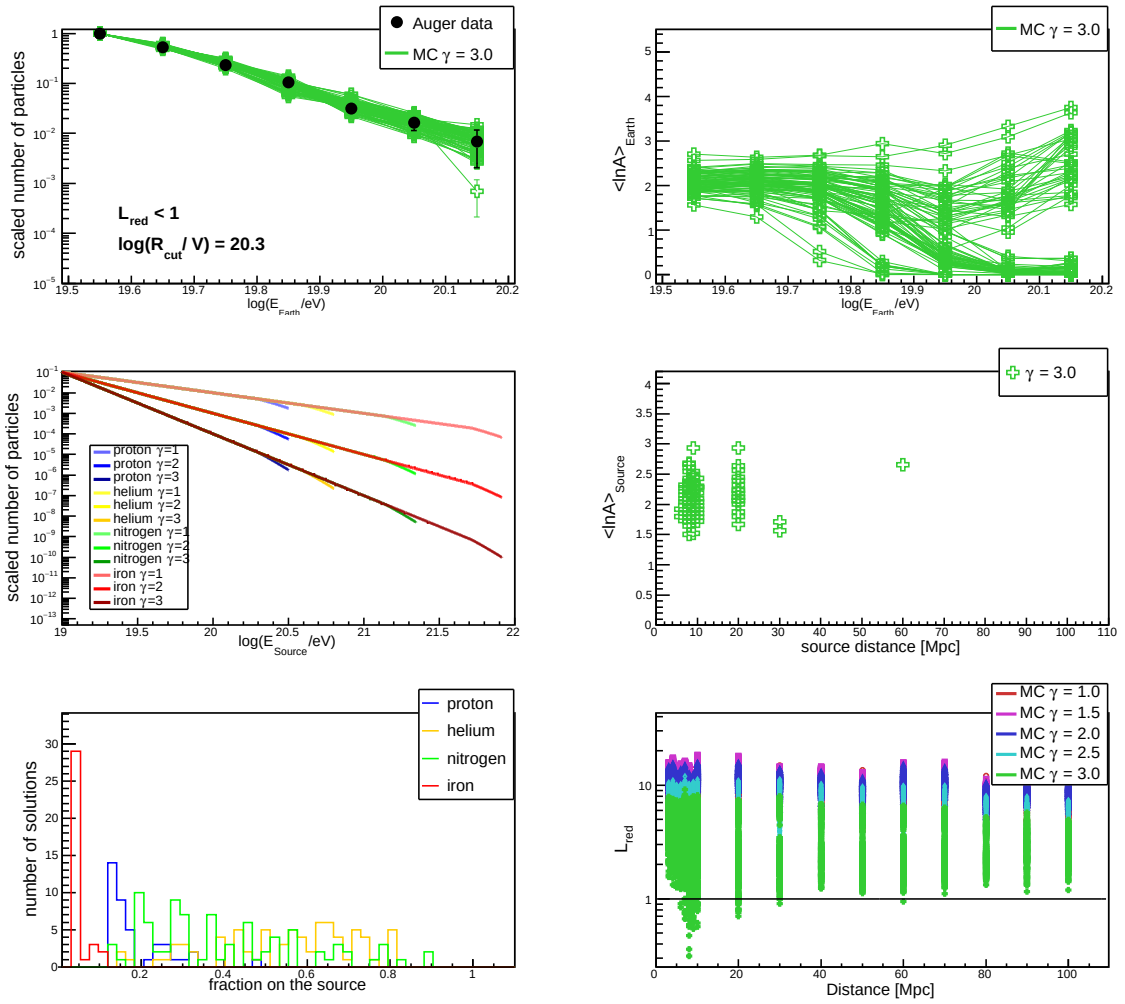

Figure A.18: Properties of simulated energy spectra for rigidity cutoff $\log(R_{\rm cut}/{\rm V}) = 20.3$. For description see caption of Figure 6.11.

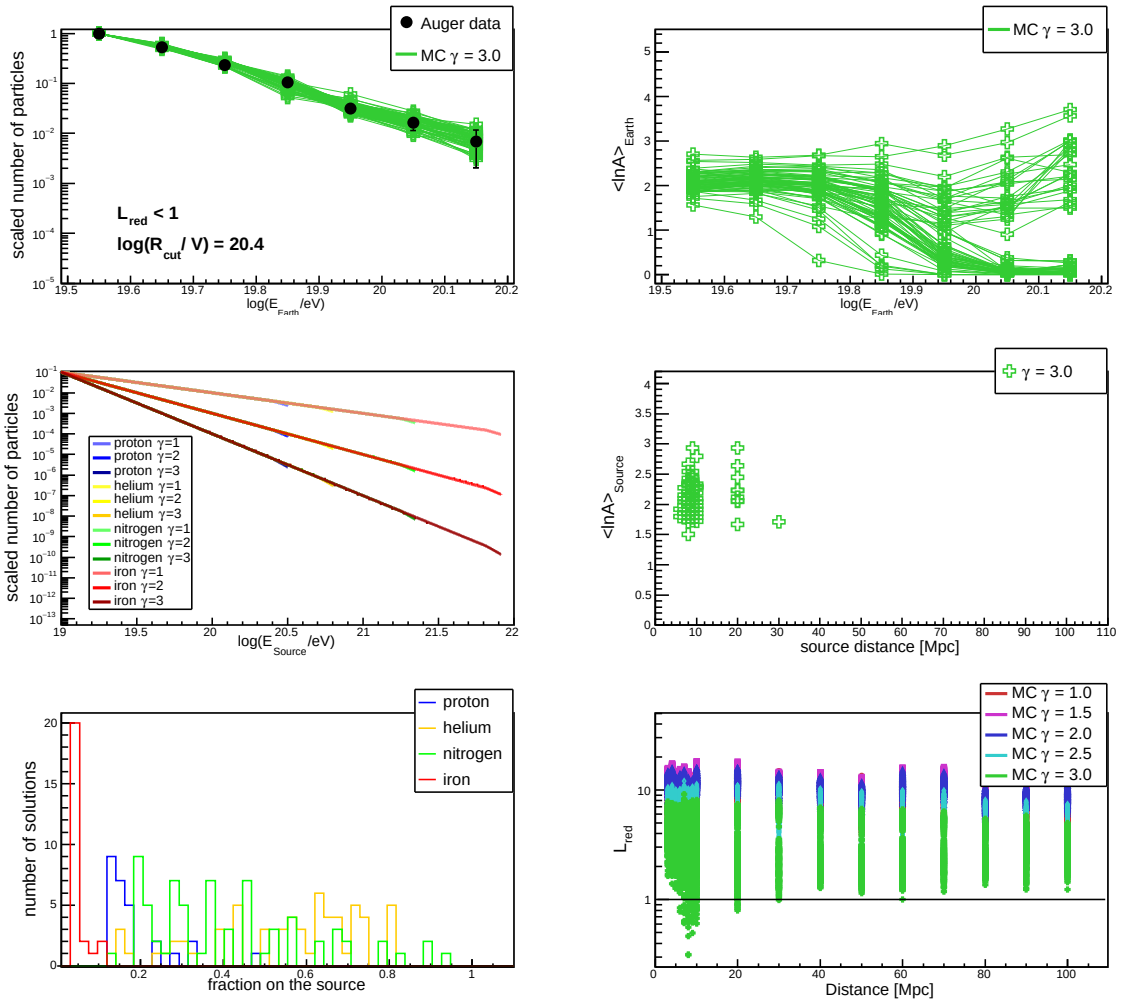

Figure A.19: Properties of simulated energy spectra for rigidity cutoff $\log(R_{\rm cut}/{\rm V}) = 20.4$. For description see caption of Figure 6.11.

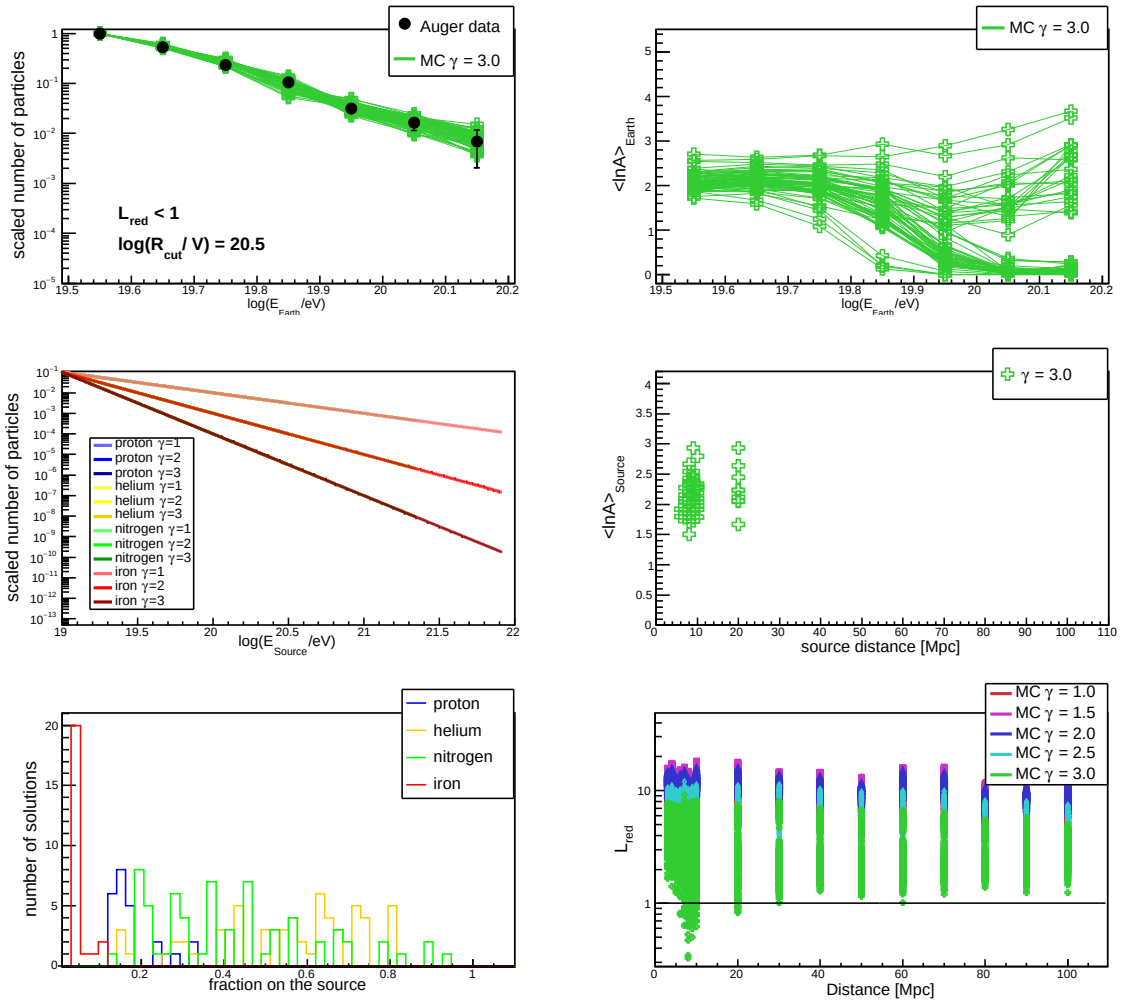

Figure A.20: Properties of simulated energy spectra for rigidity cutoff $\log(R_{\mathrm{cut}}/\mathrm{V}) = 20.5$. For description see caption of Figure 6.11.

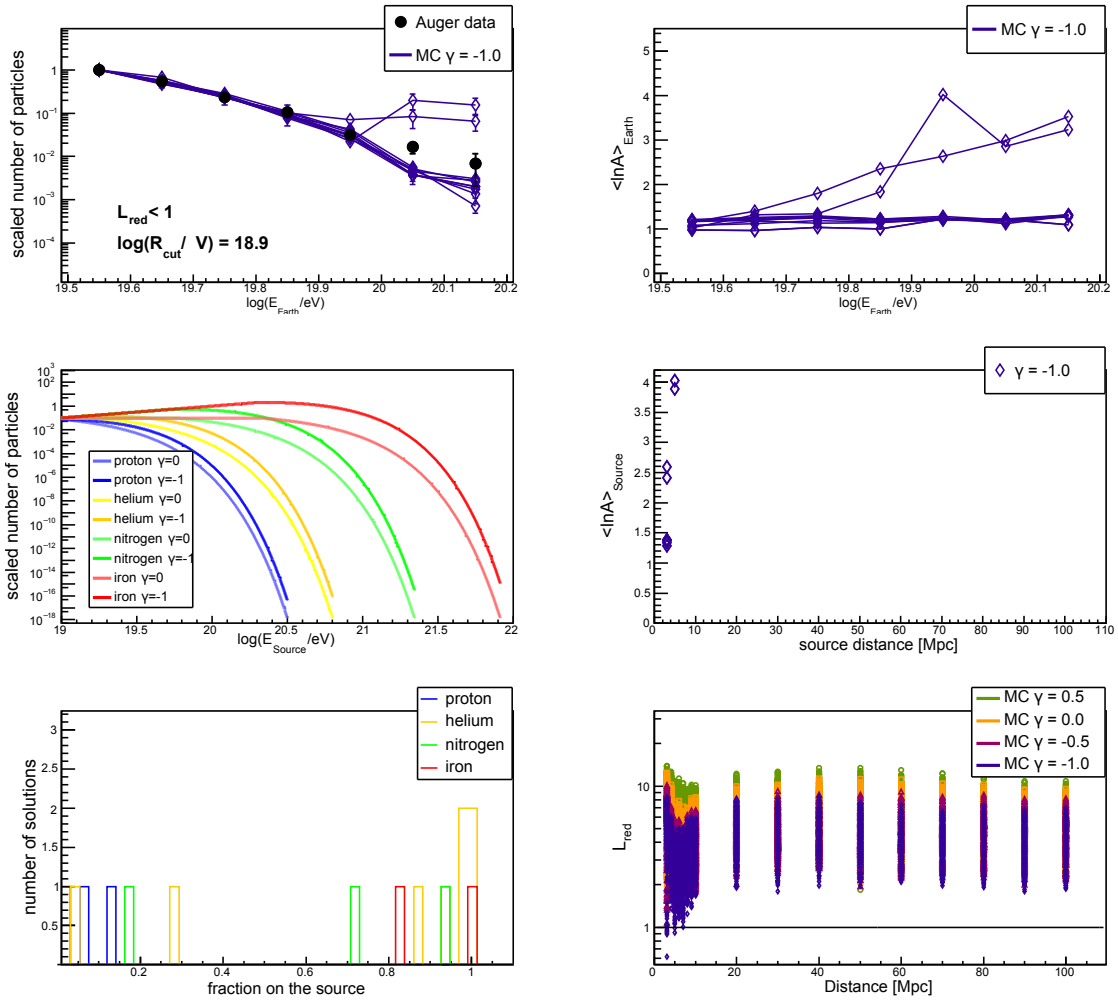

Figure A.21: Properties of simulated energy spectra with low spectral indices for rigidity cutoff $\log(R_{\rm cut}/{\rm V}) = 18.9$. For description see caption of Figure 6.11.

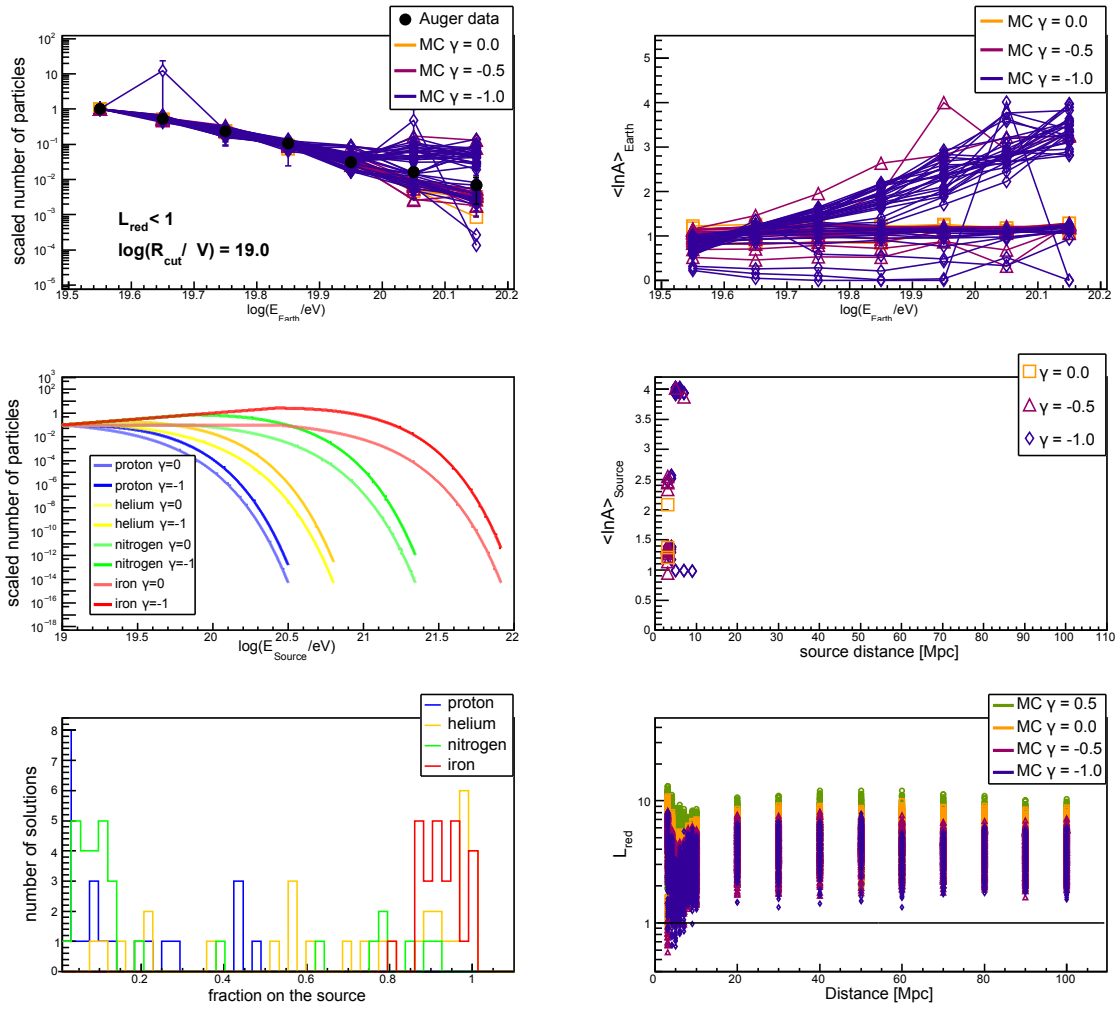

Figure A.22: Properties of simulated energy spectra with low spectral indices for rigidity cutoff $\log(R_{\rm cut}/{\rm V}) = 19.0$. For description see caption of Figure 6.11.

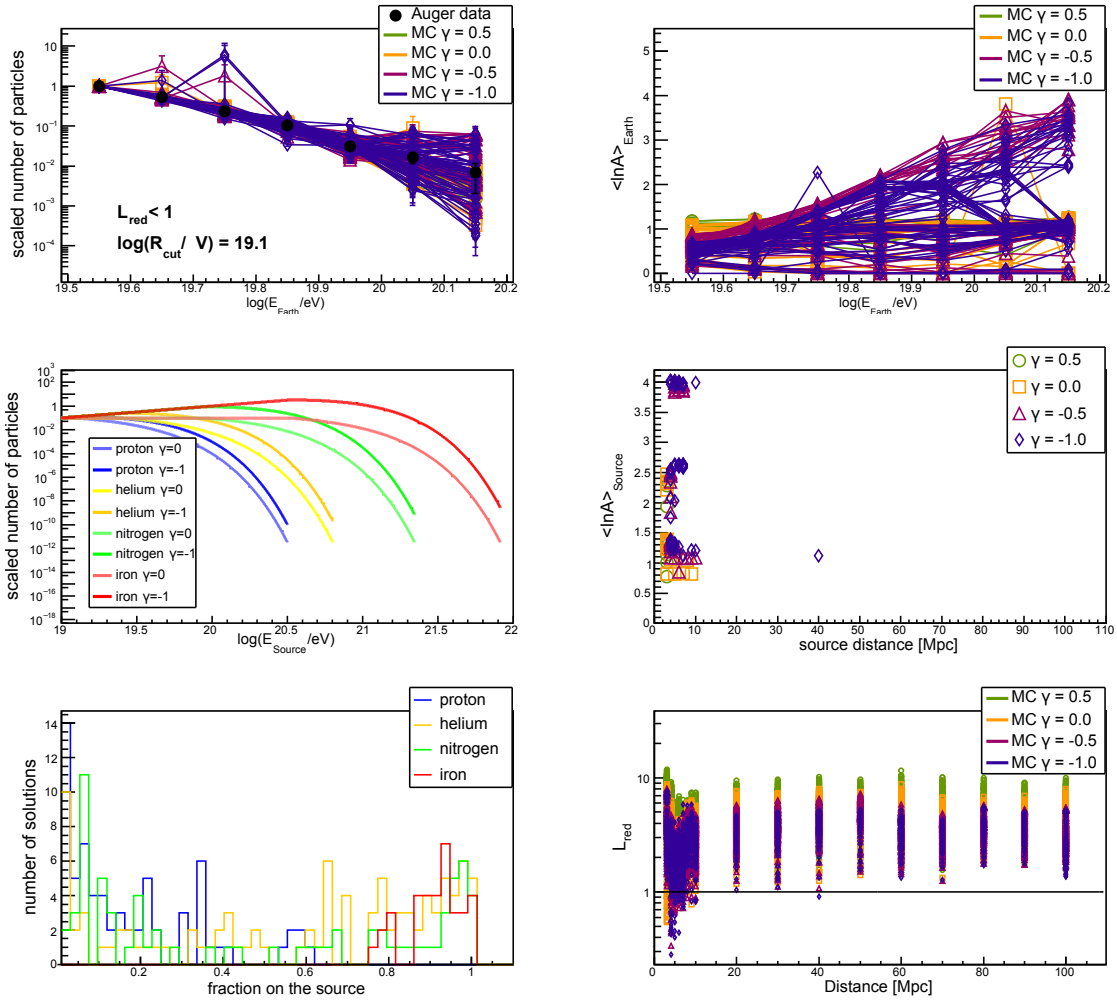

Figure A.23: Properties of simulated energy spectra with low spectral indices for rigidity cutoff $\log(R_{\rm cut}/{\rm V}) = 19.1$. For description see caption of Figure 6.11.

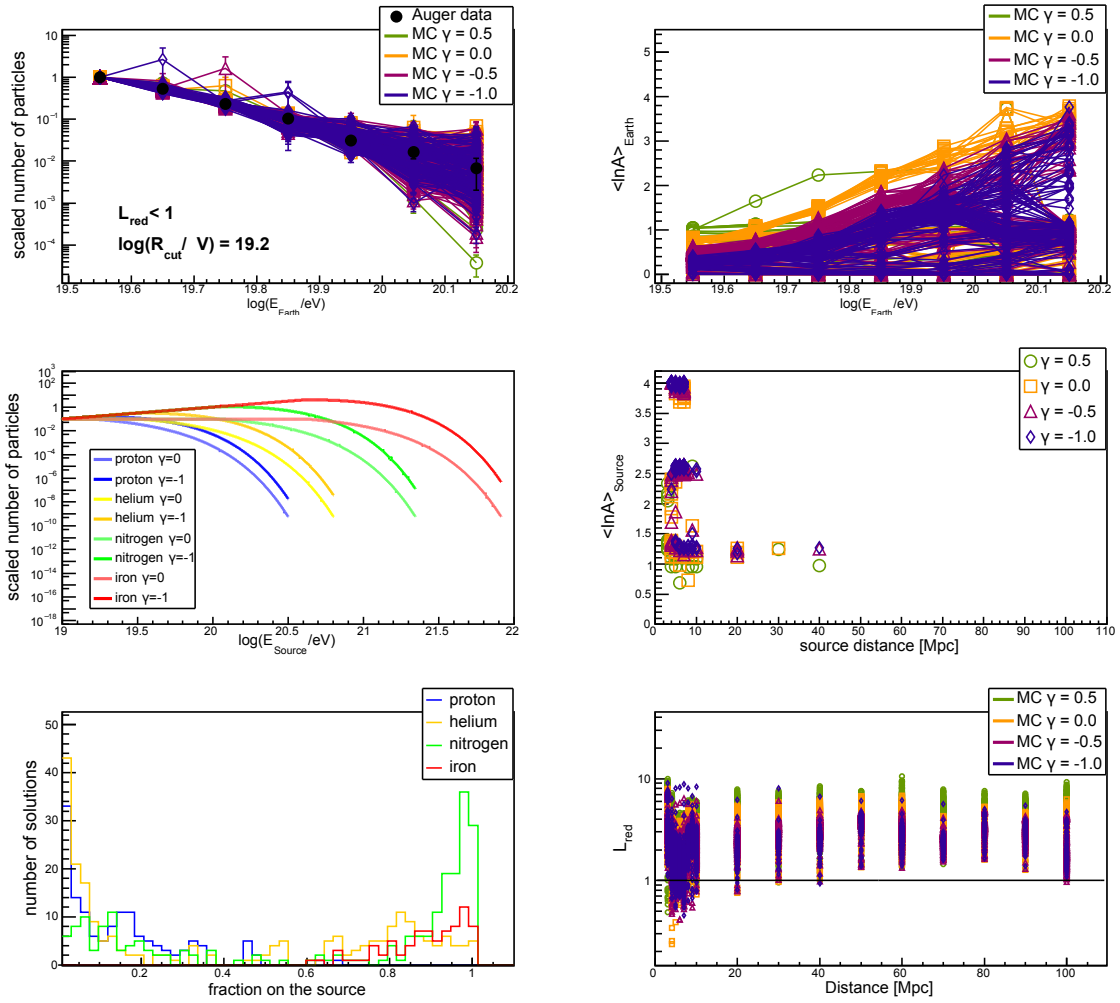

Figure A.24: Properties of simulated energy spectra with low spectral indices for rigidity cutoff $\log(R_{\mathrm{cut}}/\mathrm{V}) = 19.2$. For description see caption of Figure 6.11.

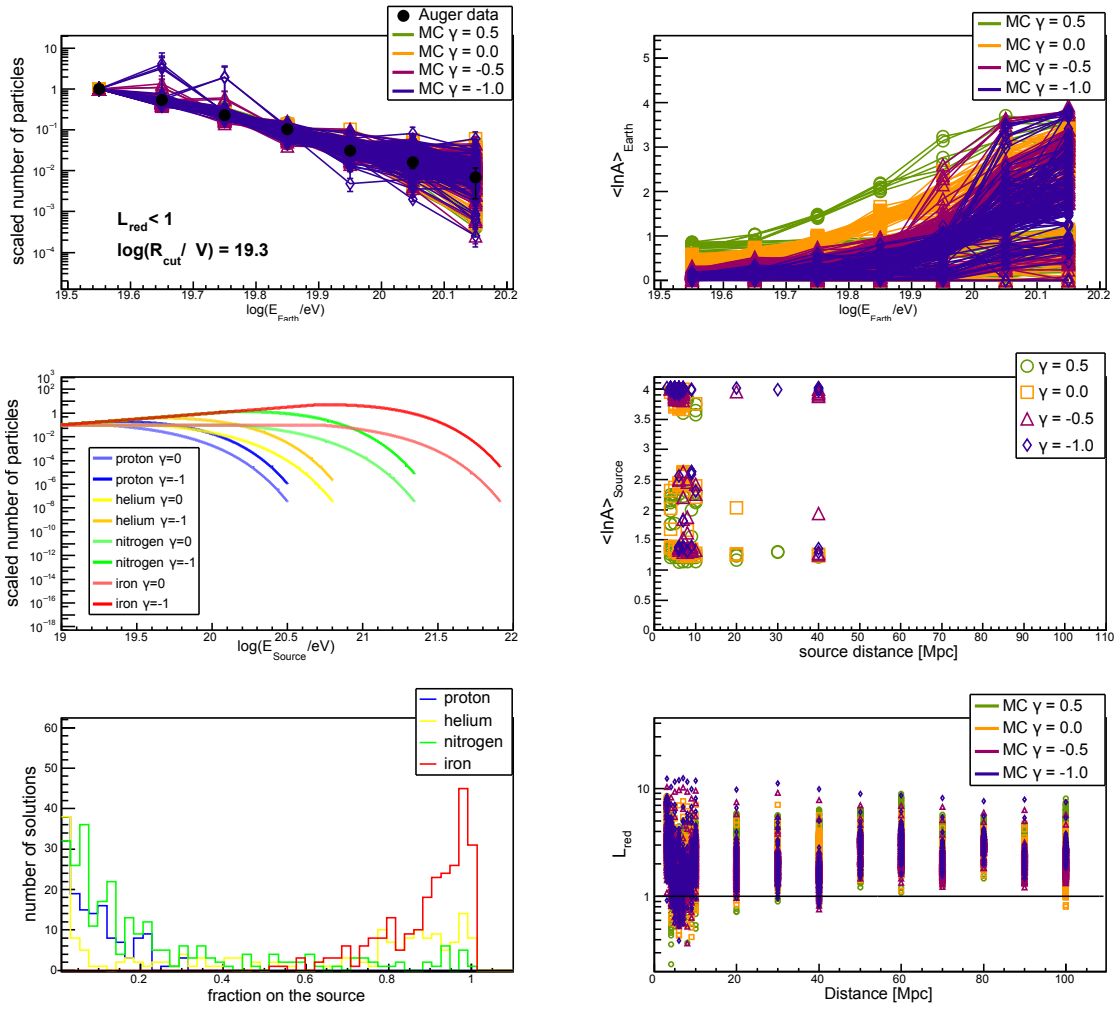

Figure A.25: Properties of simulated energy spectra with low spectral indices for rigidity cutoff $\log(R_{\mathrm{cut}}/\mathrm{V}) = 19.3$. For description see caption of Figure 6.11.

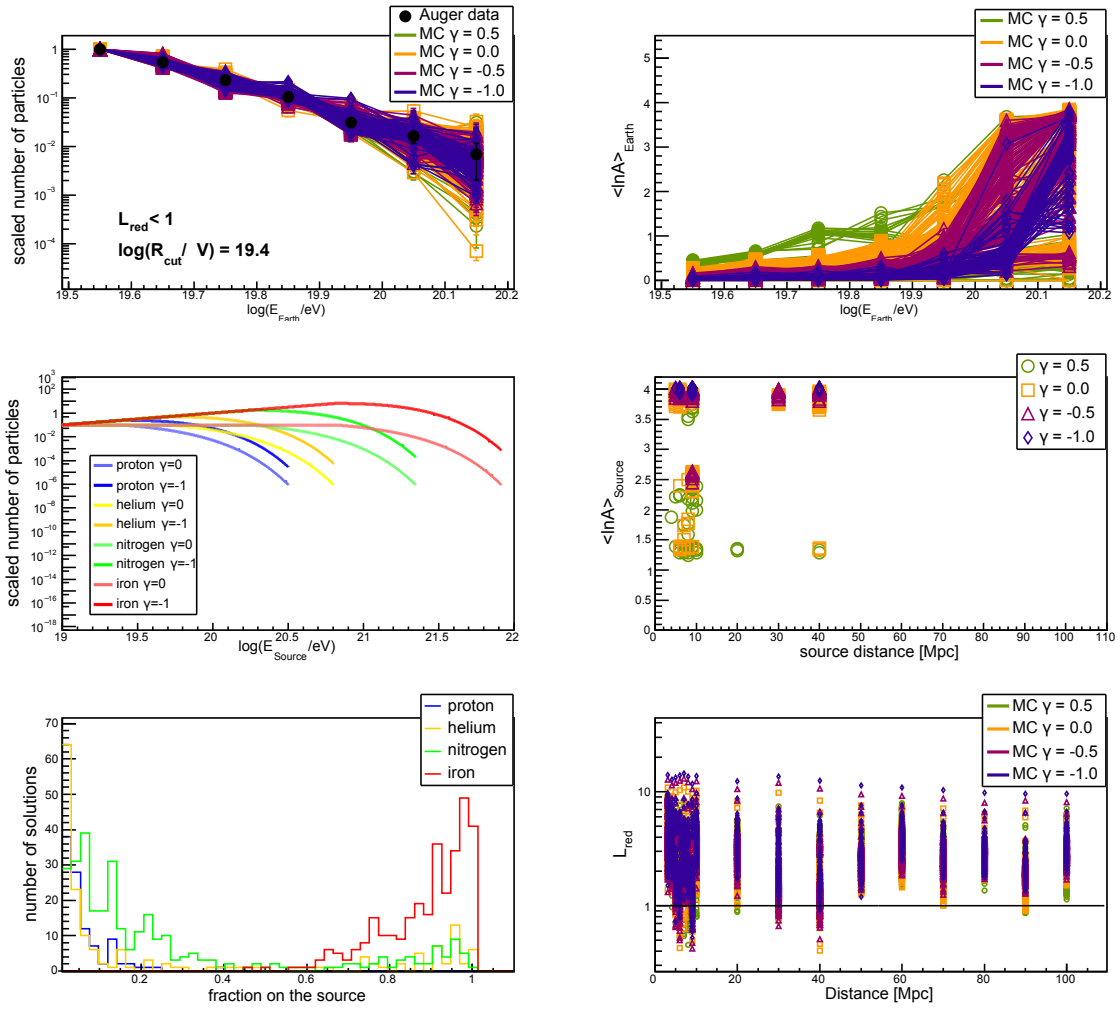

Figure A.26: Properties of simulated energy spectra with low spectral indices for rigidity cutoff $\log(R_{\mathrm{cut}}/\mathrm{V}) = 19.4$. For description see caption of Figure 6.11.

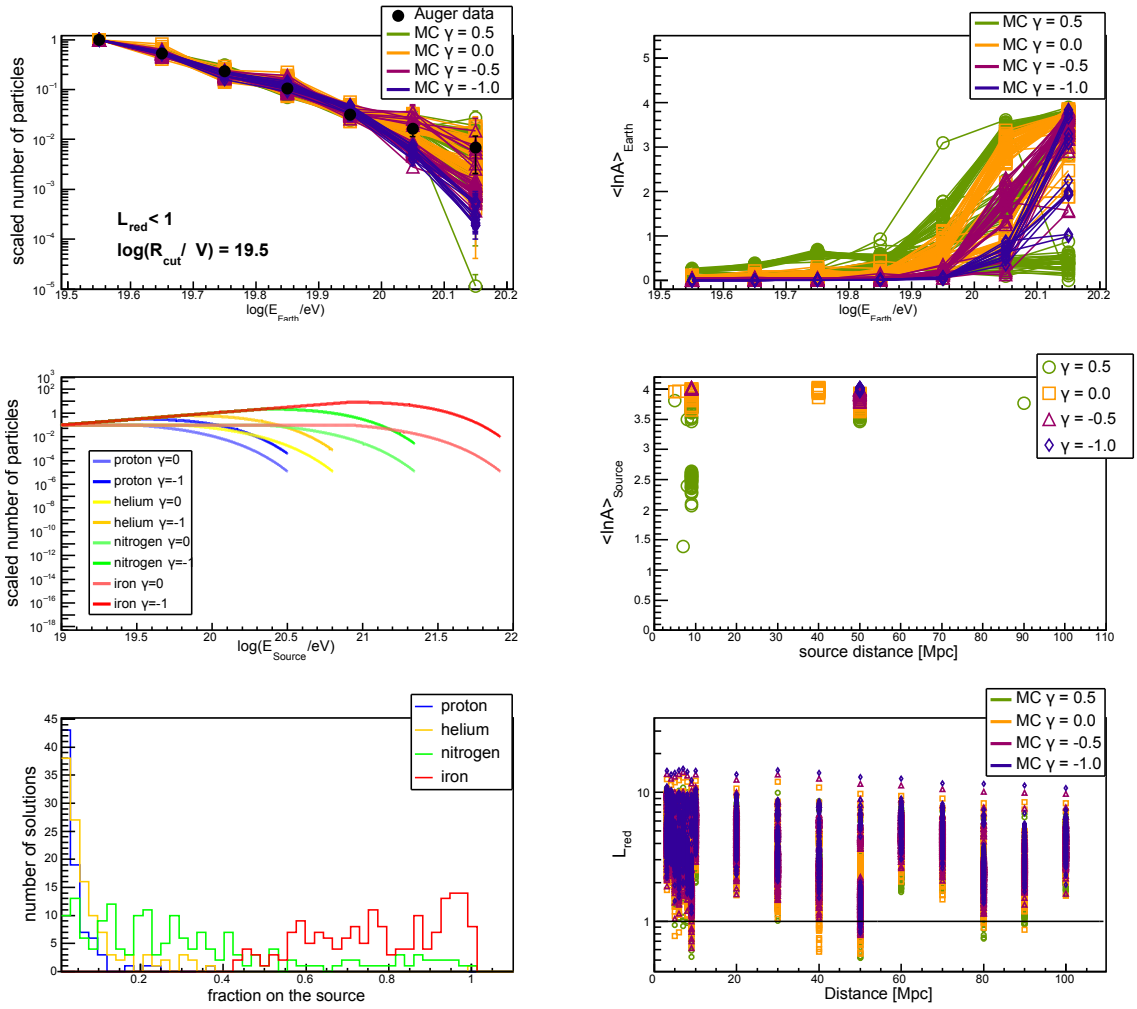

Figure A.27: Properties of simulated energy spectra with low spectral indices for rigidity cutoff $\log(R_{\mathrm{cut}}/\mathrm{V}) = 19.5$. For description see caption of Figure 6.11.

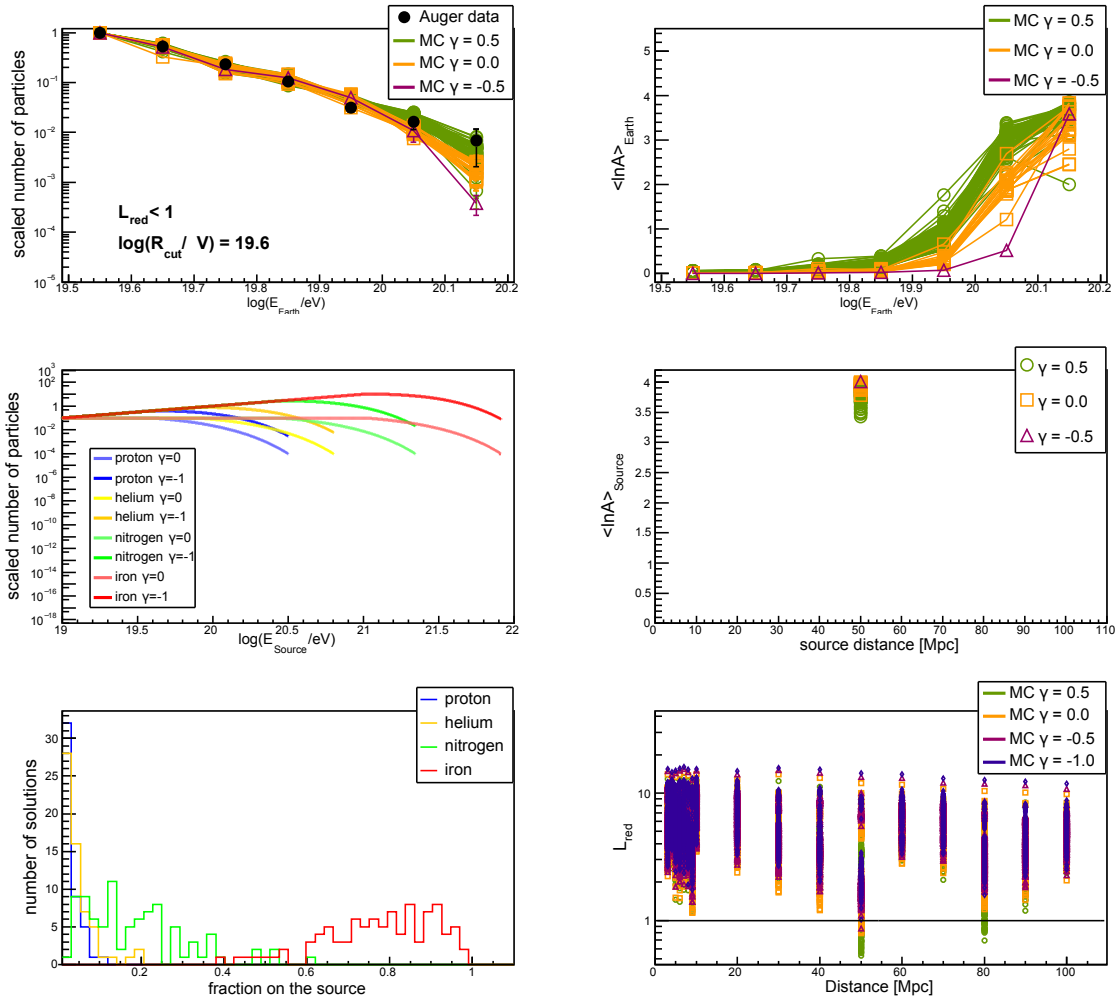

Figure A.28: Properties of simulated energy spectra with low spectral indices for rigidity cutoff $\log(R_{\mathrm{cut}}/\mathrm{V}) = 19.6$. For description see caption of Figure 6.11.

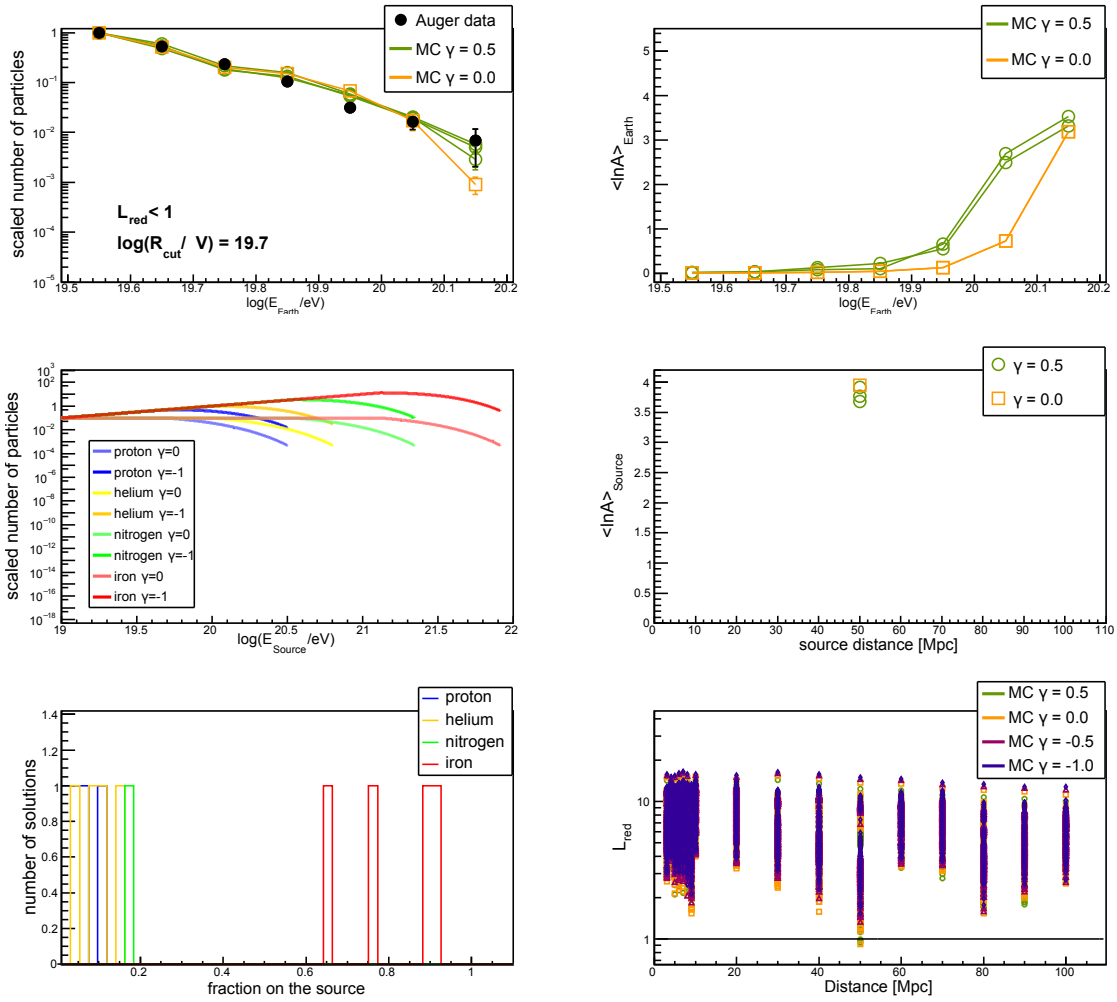

Figure A.29: Properties of simulated energy spectra with low spectral indices for rigidity cutoff $\log(R_{\mathrm{cut}}/\mathrm{V}) = 19.7$. For description see caption of Figure 6.11.

Appendix B

Effects of GMF on Arrival Directions of Cosmic Rays

Chapter 7 was dedicated to the large-scale anisotropies of arrival directions of extragalactic cosmic rays simulated in CRPropa 3. Distributions of arrival directions in the right ascension for different simulated primary particles and their combinations are illustrated below. The best fit is plotted within the figures corresponding to the best fitted values from Table 7.1.

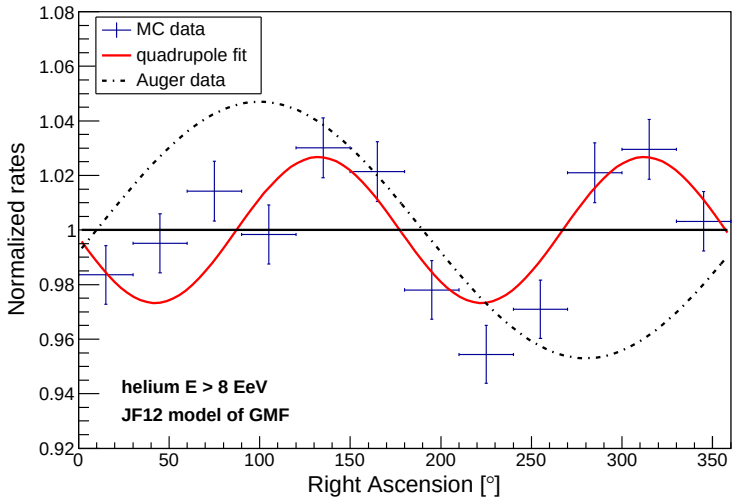

Figure B.1: Normalized rate of helium nuclei with $E > 8$ EeV hitting the observer as a function of the right ascension. Red line corresponds to the best fit by function (7.9) from Table 7.1. JF12 model of GMF was used. Dashed line corresponds to the anisotropy measured by the PAO [2].

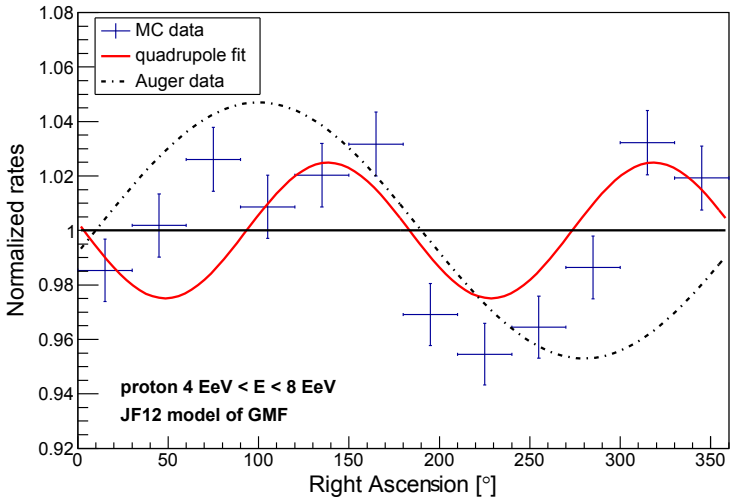

Figure B.2: Normalized rate of protons with 4 EeV $<$ E $<$ 8 EeV hitting the observer as a function of the right ascension. Red line corresponds to the best fit by function (7.9) from Table 7.1. JF12 model of GMF was used. Dashed line corresponds to the anisotropy measured by the PAO [2].

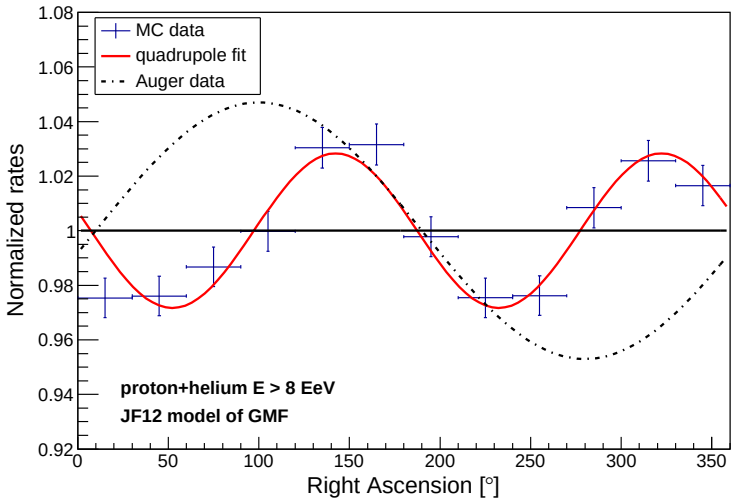

Figure B.3: Normalized rate of particles with $E > 8$ EeV hitting the observer as a function of the right ascension. Combination of simulated protons and helium nuclei propagated in JF12 model of GMF is used. Red line corresponds to the best fit by function (7.9) from Table 7.1. Dashed line corresponds to the anisotropy measured by the PAO [2].

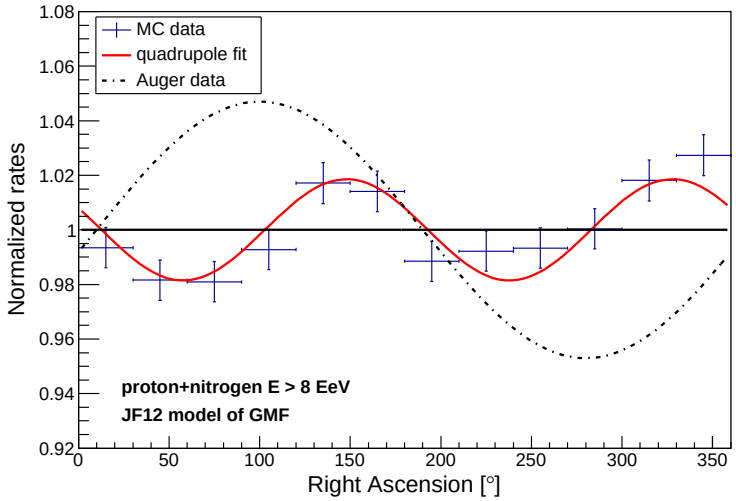

Figure B.4: Normalized rate of particles with $E > 8$ EeV hitting the observer as a function of the right ascension. Combination of simulated protons and nitrogen nuclei propagated in JF12 model of GMF is used. Red line corresponds to the best fit by function (7.9) from Table 7.1. Dashed line corresponds to the anisotropy measured by the PAO [2].

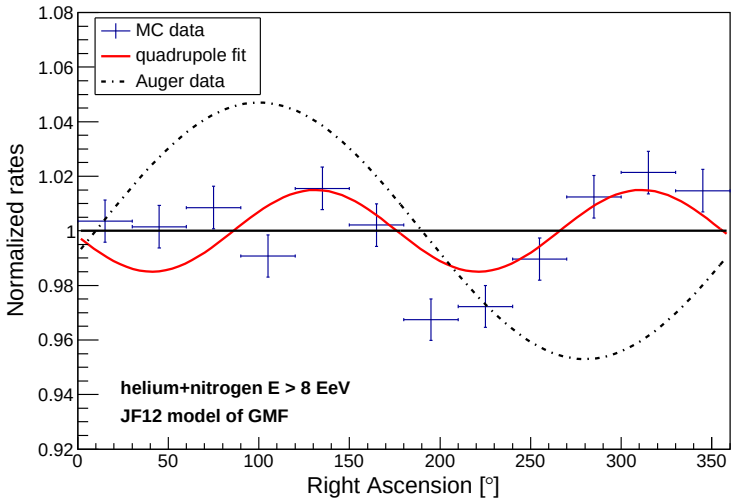

Figure B.5: Normalized rate of particles with $E > 8$ EeV hitting the observer as a function of the right ascension. Combination of simulated helium and nitrogen nuclei propagated in JF12 model of GMF is used. Red line corresponds to the best fit by function (7.9) from Table 7.1. Dashed line corresponds to the anisotropy measured by the PAO [2].

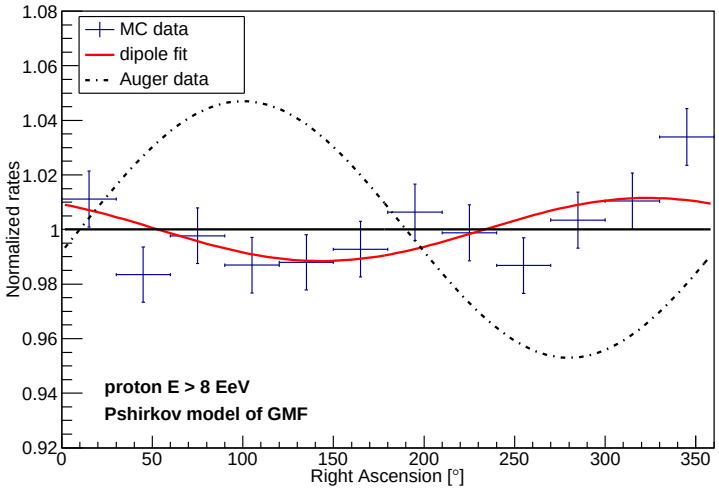

Figure B.6: Normalized rate of protons simulated with the Pshirkov model of GMF with $E > 8$ EeV hitting the observer as a function of the right ascension. Red line corresponds to the best fit by function (7.8) from Table 7.1. Dashed line corresponds to the anisotropy measured by the PAO [2].

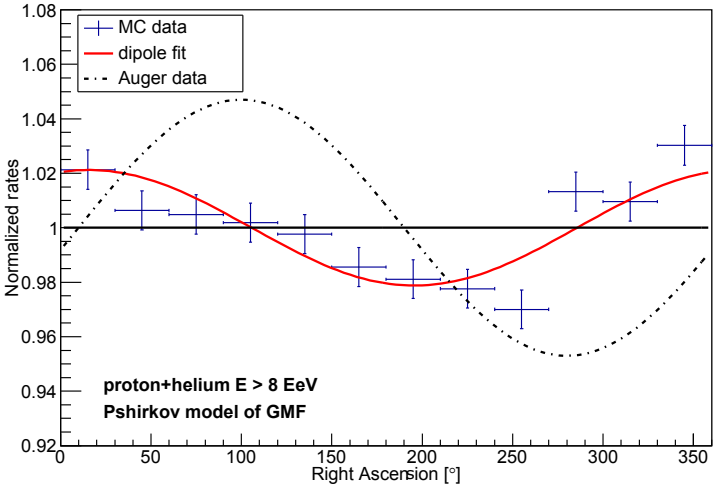

Figure B.7: Normalized rate of particles with $E > 8$ EeV hitting the observer as a function of the right ascension. Combination of simulated protons and helium nuclei propagated in the Pshirkov model of GMF is used. Red line corresponds to the best fit by function (7.8) from Table 7.1. Dashed line corresponds to the anisotropy measured by the PAO [2].

Bibliography

[1] V. F. Hess. Uber den Ursprung der durchdringenden Strahlung. *Physikalische Zeitschrift*, 610, 1913.

[2] The Pierre Auger Collaboration. Observation of a large-scale anisotropy in the arrival directions of cosmic rays above $8 \cdot 10^{18}$ eV. *Science*, 357(6357):1266–1270, September 2017.

[3] M. Bertolotti. *Celestial Messengers: Cosmic Rays: The Story of a Scientific Adventure*. Springer-Verlag Berlin Heidelberg, 2013.

[4] K.-H. Kampert and A. A. Watson. Extensive air showers and ultra high-energy cosmic rays: a historical review. *European Physical Journal H*, 37:359–412, August 2012.

[5] J. Linsley. Evidence for a primary cosmic-ray particle with energy 10^{20} eV. *Physical Review Letters*, 10:146–148, February 1963.

[6] D.H. Perkins. *Particle Astrophysics*. Oxford Master Series in Physics, 2009.

[7] M. Unger, G. R. Farrar, and L. A. Anchordoqui. Origin of the ankle in the ultrahigh energy cosmic ray spectrum, and of the extragalactic protons below it. *Physical Review D*, 92(12):123001, December 2015.

[8] KASCADE-Grande Collaboration. Investigating the 2nd knee: The kascade-grande experiment. *Journal of Physics: Conference Series*, 47(1):238, 2006.

[9] T. Abu-Zayyad, K. Belov, D. J. Bird, J. Boyer, et al. Measurement of the Cosmic-Ray Energy Spectrum and Composition from 10^{17} to $10^{18.3}$ eV Using a Hybrid Technique. *The Astrophysical Journal*, 557:686–699, August 2001.

[10] B. Peters. Primary cosmic radiation and extensive air showers. *Nuovo Cimento*, 2:800–819, November 1961.

[11] K. Greisen. End to the cosmic-ray spectrum? *Physical Review Letters*, 16:748–750, April 1966.

[12] G. T. Zatsepin and V. A. Kuzmin. Upper Limit of the Spectrum of Cosmic Rays. *Soviet Journal of Experimental and Theoretical Physics Letters*, 4:78, August 1966.

[13] J. Blümer and Pierre Auger Collaboration. The northern site of the Pierre Auger Observatory. *New Journal of Physics*, 12(3):035001, March 2010.

[14] T. Pierog, I. Karpenko, J. M. Katzy, E. Yatsenko, and K. Werner. EPOS LHC : test of collective hadronization with LHC data. *Physical Review C*, 92(1), September 2015.

[15] S. Ostapchenko. Monte Carlo treatment of hadronic interactions in enhanced Pomeron scheme: QGSJET-II model. *Physical Review D*, 83(1):014018, January 2011.

[16] F. Riehn, H. P. Dembinski, R. Engel, A. Fedynitch, T. K. Gaisser, and T. Stanev. The hadronic interaction model SIBYLL 2.3c and Feynman scaling. *ArXiv e-prints :* 1709.07227, September 2017.

[17] K.-H. Kampert and M. Unger. Measurements of the cosmic ray composition with air shower experiments. *Astroparticle Physics*, 35:660–678, May 2012.

[18] The Pierre Auger Collaboration. Muons in air showers at the Pierre Auger Observatory: Measurement of atmospheric production depth. *Physical Review D*, 90(1):012012, July 2014.

[19] The Pierre Auger Collaboration. Azimuthal asymmetry in the risetime of the surface detector signals of the Pierre Auger Observatory. *Physical Review D*, 93(7):072006, April 2016.

[20] The Pierre Auger Collaboration. The Pierre Auger Observatory Upgrade - Preliminary Design Report. *ArXiv e-prints :* 1604.03637, April 2016.

[21] The Pierre Auger Collaboration. Combined fit of spectrum and composition data as measured by the Pierre Auger Observatory. *Journal of Cosmology and Astroparticle Physics*, 4:038, April 2017.

[22] E. Fermi. On the Origin of the Cosmic Radiation. *Physical Review*, 75:1169–1174, April 1949.

[23] W. I. Axford, E. Leer, and G. Skadron. The acceleration of cosmic rays by shock waves. *International Cosmic Ray Conference*, 11:132–137, 1977.

[24] N. Bucciantini, T. A. Thompson, J. Arons, E. Quataert, and L. Del Zanna. Relativistic magnetohydrodynamics winds from rotating neutron stars. *Monthly Notices of the Royal Astronomical Society*, 368(4):1717–1734, February 2006.

[25] K. Kotera, E. Amato, and P. Blasi. The fate of ultrahigh energy nuclei in the immediate environment of young fast-rotating pulsars. *Journal of Cosmology and Astroparticle Physics*, 2015(08):026, August 2015.

[26] A. Bykov, N. Gehrels, H. Krawczynski, M. Lemoine, G. Pelletier, and M. Pohl. Particle Acceleration in Relativistic Outflows. *Space Science Reviews*, 173:309–339, November 2012.

[27] P. Chen, T. Tajima, and Y.i Takahashi. Plasma wakefield acceleration for ultrahigh-energy cosmic rays. *Physical Review Letters*, 89:161101, September 2002.

[28] D. Kuempel. Extragalactic Propagation of Ultra-High Energy Cosmic Rays. *ArXiv e-prints :* 1409.3129, September 2014.

[29] D. Allard. Propagation of extragalactic ultra-high energy cosmic-ray nuclei : implications for the observed spectrum and composition. In *Proceedings on 44th Rencontres de Moriond on Very High Energy Phenomena in the Universe*, pages 219–226, February 2009.

[30] R. Alves Batista, D. Boncioli, A. di Matteo, A. van Vliet, and D. Walz. Effects of uncertainties in simulations of extragalactic UHECR propagation, using CRPropa and SimProp. *Journal of Cosmology and Astroparticle Physics*, 10:063, October 2015.

[31] S. Hackstein, F. Vazza, M. Brüggen, G. Sigl, and A. Dundovic. Propagation of ultrahigh energy cosmic rays in extragalactic magnetic fields: a view from cosmological simulations. *Monthly Notices of the Royal Astronomical Society*, 462:3660–3671, November 2016.

[32] L. M. Widrow. Origin of galactic and extragalactic magnetic fields. *Reviews of Modern Physics*, 74:775–823, August 2002.

[33] R. Beck. Galactic and Extragalactic Magnetic Fields. volume 1085 of *American Institute of Physics Conference Series*, pages 83–96, December 2008.

[34] R. Jansson and G. R. Farrar. A New Model of the Galactic Magnetic Field. *The Astrophysical Journal*, 757:14, September 2012.

[35] M. S. Pshirkov, P. G. Tinyakov, P. P. Kronberg, and K. J. Newton-McGee. Deriving the Global Structure of the Galactic Magnetic Field from Faraday Rotation Measures of Extragalactic Sources. *The Astrophysical Journal*, 738:192, September 2011.

[36] J. C. Brown, M. Haverkorn, B. M. Gaensler, A. R. Taylor, N. S. Bizunok, N. M. McClure-Griffiths, J. M. Dickey, and A. J. Green. Rotation Measures of Extragalactic Sources behind the Southern Galactic Plane: New Insights into the Large-Scale Magnetic Field of the Inner Milky Way. *Astrophysical Journal*, 663:258–266, July 2007.

[37] M. Prouza and R. Šmída. The Galactic magnetic field and propagation of ultra-high energy cosmic rays. *Astronomy and Astrophysics*, 410:1–10, October 2003.

[38] R. Alves Batista, A. Dundovic, M. Erdmann, K.-H. Kampert, D. Kuempel, G. Müller, G. Sigl, A. van Vliet, D. Walz, and T. Winchen. CRPropa 3 - A public astrophysical simulation framework for propagating extraterrestrial ultra-high energy particles. *Journal of Cosmology and Astroparticle Physics*, 5:038, May 2016.

[39] K. Dolag, D. Grasso, V. Springel, and I. Tkachev. Mapping Deflections of Extragalactic Ultra High Energy Cosmic Rays in Magnetohydrodynamic Simulations of the Local Universe. *Nuclear Physics B Proceedings Supplements*, 136:234–243, November 2004.

[40] K. Dolag, M. Kachelriess, S. Ostapchenko, and R. Tomàs. Lower limit on the strength and filling factor of extragalactic magnetic fields. *The Astrophysical Journal Letters*, 727(1):L4, 2011.

[41] The Pierre Auger Collaboration. The Pierre Auger Cosmic Ray Observatory. *Nuclear Instruments and Methods in Physics Research*, 798:172–213, October 2015.

[42] R. M. Baltrusaitis, R. Cady, G. L. Cassiday, R. Cooperv, J. W. Elbert, P. R. Gerhardy, S. Ko, E. C. Loh, M. Salamon, D. Steck, and P. Sokolsky. The Utah Fly's Eye detector. *Nuclear Instruments and Methods in Physics Research A*, 240:410–428, October 1985.

[43] The Pierre Auger Collaboration. Inferences on mass composition and tests of hadronic interactions from 0.3 to 100 eev using the water-cherenkov detectors of the pierre auger observatory. *Physical Review D*, 96:122003, December 2017.

[44] The Pierre Auger Collaboration. The Fluorescence Detector of the Pierre Auger Observatory. *Nuclear Instruments and Methods in Physics Research A*, 620:227–251, August 2010.

[45] V. Novotný, D. Nosek, and J. Vícha. Energy spectrum of cosmic rays derived from Cherenkov-dominated data sample. *internal GAP Notes*, GAP-2017-067, 2017.

[46] V. Novotný, D. Nosek, and J. Vícha. Accuracy of shower parameters in stereo reconstruction. *internal GAP Notes*, GAP-2013-110, 2013.

[47] T. K. Gaisser and A. M. Hillas. Reliability of the method of constant intensity cuts for reconstructing the average development of vertical showers. *International Cosmic Ray Conference*, 8:353–357, 1977.

[48] K. Kamata and J. Nishimura. The Lateral and the Angular Structure Functions of Electron Showers. *Progress of Theoretical Physics Supplement*, 6:93–155, February 1958.

[49] K. Greisen. *The extensive air showers, Progress in Cosmic Ray Physics Vol. III.* 1956.

[50] J. Hersil, I. Escobar, D. Scott, G. Clark, and S. Olbert. Observations of extensive air showers near the maximum of their longitudinal development. *Physical Review Letters*, 6:22–23, January 1961.

[51] H. Kawai, S. Yoshida, H. Yoshii, K. Tanaka, et al. Telescope Array Experiment. *Nuclear Physics B Proceedings Supplements*, 175:221–226, January 2008.

[52] F. Fenu for the Pierre Auger Collaboration. The cosmic ray energy spectrum measured using the Pierre Auger Observatory. In *Proceedings of the 35th International Cosmic Ray Conference, Busan, Korea*, volume 486, 2017.

[53] V. Verzi, D. Ivanov, and Y. Tsunesada. Measurement of Energy Spectrum of Ultra-High Energy Cosmic Rays. *ArXiv e-prints :* 1705.09111, May 2017.

[54] J. Bellido for the Pierre Auger Collaboration. Depth of maximum of air-shower profiles at the pierre auger observatory: Measurements above $10^{17.2}$ eV and composition implications. In *Proceedings of Science*, volume 506, July 2017.

[55] The Pierre Auger Collaboration. Searches for Anisotropies in the Arrival Directions of the Highest Energy Cosmic Rays Detected by the Pierre Auger Observatory. *Astrophysical Journal Letters*, 804(1):15, May 2015.

[56] The Tescope Array Collaboration. Indications of Intermediate-Scale Anisotropy of Cosmic Rays with Energy Greater Than 57 EeV in the Northern Sky Measured with the Surface Detector of the Telescope Array Experiment. *Astrophysical Journal Letters*, 790:L21, August 2014.

[57] The Pierre Auger Collaboration. An Indication of anisotropy in arrival directions of ultra-high-energy cosmic rays through comparison to the flux pattern of extragalactic gamma-ray sources. *Astrophysical Journal Letters*, 853:L29, February 2018.

[58] A. Domínguez et al. Extragalactic background light inferred from AEGIS galaxy-SED-type fractions. *Monthly Notices of the Royal Astronomical Society*, 410:2556–2578, February 2011.

[59] R. Aloisio, D. Boncioli, A. F. Grillo, S. Petrera, and F. Salamida. SimProp: a simulation code for ultra high energy cosmic ray propagation. *Journal of Cosmology and Astroparticle Physics*, 10:007, October 2012.

[60] D. N. Spergel et al. First-year wilkinson microwave anisotropy probe (wmap) observations: Determination of cosmological parameters. *The Astrophysical Journal Supplement Series*, 148(1):175, 2003.

[61] G. R. Farrar. The Galactic magnetic field and ultrahigh-energy cosmic ray deflections. *Comptes Rendus Physique*, 15:339–348, April 2014.

[62] P. Duffett-Smith and J. Zwart. *Practical Astronomy with your Calculator or Spreadsheet*. Cambridge: Cambridge University Press, May 2011.

[63] atan2. `http://reference.wolfram.com/system-modeler/libraries/ModelicaReference/ModelicaReference.Operators.'atan2()'.html`. Accessed: 2018-05-02.

[64] E. W. Weisstein. "mollweide projection." from mathworld–a wolfram web resource. `http://mathworld.wolfram.com/MollweideProjection.htmll`. Accessed: 2018-05-02.